Lancashire Online Knowledge

University of Lancashire's Institutional Repository

TMAPes Role in Understanding Partic

le Injection and Energization Throughout th

e

Heliosphere

Type

URL https://knowledge.la

.org/10.1007/s11214-025-01257-4

2026

Cone

n, oc. M. S., Alterman, B. L., Baker, D. N,

Bruno, A., Bzowski, M., Christian, E. R.,

Cohen, I. J., Dalla, Silvia, Dayeh, M. A. e

tal (2026)

IMAP's Role in Understanding Pa

rticle Injection and Energization Throughou

t the Heliosphere. Space Science Reviews, 2

22(1). ISSN 0038-6308

Cohenors. M.S., Al

terman, B.L., Baker, D.N., Bruno, A., Bzo

wski, M., Christian, E. R., Cohen, I. J., D

alla, Silvia, Dayeh, M. A., Desai, M. I., E

lliott, H.A., Giacalone, J., Gkioulidou, M

, Guo, F., Horbury, T., Kanekal, S. G., Ko

walska - Leszczyńska, I., Lee, C.O., Livadio

tis, G. I., Luhmann, J. G., Matthaeus, W. H

, McComas, D. J., Mitchell, J. G., Moebius

, E., Rankin, J., Richardson, J. D., Schwad

ron, N. A., Skoug, R., Turner, D., Zank, G.

and Zirnstein, E. J.

It is advisable to refer to the publisher's version if you intend to cite from the work. https://doi.org/10.1007/s11214-025-01257-4

For information about Research at the University of Lancashire, please go to: University of Lancashire's research pages

IMAP's Role in Understanding Particle Injection and Energization Throughout the Heliosphere

C.M.S. Cohen[1] [iD] **· B.L. Alterman[2] · D.N. Baker[3] · A. Bruno[2,4] · M. Bzowski[5] ·
E.R. Christian[2] · I.J. Cohen[6] · S. Dalla[7] · M.A. Dayeh[8] · M.I. Desai[8] · H.A. Elliott[8] ·
J. Giacalone[9] · M. Gkioulidou[6] · F. Guo[10] · T. Horbury[11] · S.G. Kanekal[2] ·
I. Kowalska-Leszczyńska[5] · C.O. Lee[12] · G.I. Livadiotis[13] · J.G. Luhmann[12] ·
W.H. Matthaeus[14] · D.J. McComas[13] · J.G. Mitchell[2] · E. Moebius[15] · J. Rankin[13] ·
J.D. Richardson[16] · N.A. Schwadron[15] · R. Skoug[10] · D. Turner[6] · G. Zank[17] ·
E.J. Zirnstein[13]**

Abstract

The payload of the Interstellar Mapping and Acceleration Probe (IMAP) includes sophisticated in situ instruments to measure solar wind plasma and magnetic fields, suprathermal and energetic particles at 1 au as well as unprecedented remote sensing instruments to observe the energetic neutral atoms (ENAs) in the outer heliosphere and the ultraviolet glow of the interstellar neutral H interacting with the three-dimensional solar wind. This unique combination of sensors on a single platform allows connections to be made between the inner and outer heliosphere to an extent never before possible. This article focuses on the scientific theme of connecting the physics of particle acceleration and transport throughout the heliosphere. Such studies enabled by IMAP are organized into three broad categories: i) fundamental particle acceleration and transport processes, ii) heliospheric variability that affects those processes, and iii) inner heliospheric science.

1 Introduction

The heliosphere is a vast and complex 'system of systems' and fully understanding its structure and interaction with interstellar space, as well as the variability of both aspects, remains an important goal of heliophysics. The Interstellar Mapping and Acceleration Probe (IMAP) mission (McComas et al. 2025b) has a suite of 10 instruments, for both remote sensing and in situ observations, to make significant advances on this goal. Four science objectives were defined previously for the mission (McComas et al. 2018a):

1. Improve understanding of the composition and properties of the LISM.
2. Advance understanding of the temporal and spatial evolution of the boundary region in which the solar wind and the interstellar medium interact.

Extended author information available on the last page of the article

3. Identify and advance understanding of processes related to the interactions of the magnetic field of the Sun and the LISM.
4. Identify and advance understanding of particle injection and acceleration processes near the Sun, in the heliosphere and heliosheath.

This article focuses primarily on the particular challenge of the fourth objective.

The last three decades of heliophysics observations and research have revolutionized our understanding of the space environment near Earth, with a primary focus on connections between the Sun and measurements of ionizing photons, particles and fields at 1 au. However, the same missions needed to interpret the near-Earth conditions (e.g., SOHO, Ulysses, ACE, and STEREO) also led to the development of a global conceptual framework for understanding the 3D spatial and temporal structure of the global inner heliosphere – with the Sun as its inner boundary (see e.g., Riley et al. 2001; Odstrcil 2023; Pomoell and Poedts 2018).

This inner heliospheric perspective, with its emphasis on solar drivers, has taught us a great deal about the quasi-steady and transient corona and solar wind, over both quiet and active phases of the solar cycle (e.g. Riley et al. 2022; Zhang et al. 2023). Concurrently, research with a more 'outer' heliospheric perspective has steadily advanced. For example, measurements of both galactic and 'anomalous' cosmic rays, the former of which had been monitored from the ground for decades, are both better interpreted and have led to new insights as a result of better understanding global heliospheric structure (see, e.g., reviews by Rankin et al. 2022 and Giacalone et al. 2022). At the same time, interest has grown in what happens beyond the inner heliosphere, and how it affects our own environment. The establishment of the prevailing explanation for the anomalous cosmic rays, with their distinctive composition, charge states, and energy distributions, as accelerated 'pickup ion' messengers from the edge of interstellar space, inspired a new generation of theoretical and modeling work to extend inner heliosphere models to the outermost reaches of solar wind influence (see, e.g., Pogorelov et al. 2013; Kleinmann et al. 2022). A new methodology that in part grew out of this interest has been the use of measurements of energetic neutral atoms (ENAs) produced in charge exchange reactions between solar wind protons and penetrating interstellar gas to probe the outer heliosphere (Galli et al. 2014; McComas et al. 2024).

The IBEX (Interstellar Boundary Explorer) mission (McComas 2009a) applied new remote sensing techniques of ENAs to demonstrate the unique value of ENA maps to study the outer boundaries of the heliosphere. In effect, IBEX's images of the outer heliospheric boundary are a counterpart to the imaging of solar drivers at the heart of the system, providing constraints on the spatial and temporal conditions that both dictate, and reflect, the inner heliospheric conditions. IMAP builds upon this by uniquely combining advanced neutral imaging with the critical in situ measurements that provide a 'ground truth' for the inferred properties of the larger heliospheric models to which IMAP data must be compared. Every extrapolation of the heliospheric structure and physics inferred from the remote sensing with ENAs should be consistent with the in situ IMAP measurements of the galactic and anomalous cosmic ray (GCR and ACR), solar energetic particle (SEP), solar wind, and local pickup ion (PUI) responses to the more global heliospheric conditions. With its in situ suite of particle and magnetic field instruments, IMAP investigates the nature of particle acceleration in the inner heliosphere, revealing new details that further illuminate the physics of the more distant heliosphere and astrospheres across the cosmos.

The following sections highlight a few of the key scientific studies that the IMAP mission (McComas et al. 2025b) enables, organized into three broad sub-themes: i) fundamental particle acceleration and transport processes, ii) heliospheric variability, and iii) inner heliospheric science. However, before turning to these, we first introduce a few concepts that

the later sections have in common, including the critical role of interstellar PUIs, the structure of the solar wind and associated transients, and the need to leverage the limited in situ observations available beyond 1 au in order to achieve IMAP science.

1.1 The Role of Pickup Ions in the Heliosphere

Heliospheric PUIs are created when incoming neutrals from the local interstellar cloud become ionized by charge exchange with the outflowing solar wind, by solar UV, or by suprathermal electrons (e.g., Vasyliunas and Siscoe 1976; Möbius et al. 1985; Sokół et al. 2022; Zirnstein et al. 2022a, and references therein) at energies $\geq \sim 1$ keV/nuc. Such ionization and PUI generation occurs throughout the heliosphere. The PUI to solar wind density ratio increases with increasing heliocentric distance, until the PUI pressure rapidly dominates that of the solar wind. Beyond that point, PUIs substantially modify and even dominate the plasma physics in the outer heliosphere, especially between the termination shock and the heliopause (for more detailed discussions with specific connections to IMAP see, e.g., Reisenfeld et al. 2026 and Szalay et al. 2026).

As noted above, PUIs have long been recognized as the likely origin of ACRs - the unexpected enhanced populations of protons, helium, nitrogen, oxygen, and neon at 10 s to ~ 100 MeV/nucleon - which were first discovered by Pioneer 10 (McDonald et al. 1974; Fisk et al. 1974). While the source of these ACRs was initially unknown, the connection to PUIs was evidenced by observations that ACRs are predominantly singly ionized (Oschlies et al. 1989; Singh et al. 1991; Dutta et al. 1993; Klecker 1995), although occasionally doubly-ionized ACRs have been observed (Mewaldt et al. 1996). PUIs are also created from solar wind-grain interactions in the solar wind (Gloeckler et al. 2000; Schwadron et al. 2000) with abundances that resemble the solar wind. Interstellar PUIs are dominated by high FIP species (e.g., He and Ne) but are depleted in low FIP species. The PUIs from the solar wind-grain interactions supplies the ACR species (Schwadron and Gloeckler 2007) with lower first ionization potentials (e.g., C, Si, Mg, Fe), particularly from PUI sources in the Kuiper Belt (Schwadron et al. 2002). Today, a leading theory is that ACRs result from shock drift acceleration of PUIs at the termination shock inside of which the pressure of the solar wind outflow is effectively stopped as it meets its local interstellar equivalent (e.g., Axford et al. 1977; Krymsky 1977; Bell 1978; Blandford and Ostriker 1978; Armstrong et al. 1985; Jokipii 1986; Klecker 1995; Giacalone et al. 2022). Further, McComas and Schwadron (2006) proposed that the shape of the shock was important, with it being blunt on the nose and extending much farther from the Sun in the flanks and tail, which allows acceleration up to the observed ACR energies (Schwadron et al. 2008; Cummings et al. 2024). However, the exact steps of the energization process necessary to bring these particles from ~ 1 keV up to ~ 100 MeV energies remains to be understood.

PUIs also play a critical role in the generation of the ENAs imaged by IMAP. In particular, the combination of in situ observations by Voyager 2 and New Horizons, remote sensing from IBEX, and theory, simulations, and modeling, has provided a compelling scenario for the origin of ENAs with energies in the range of a few keV (Gruntman et al. 2001). PUIs are heated and accelerated at the solar wind termination shock and are advected from there into the heliosheath, along with the solar wind. The PUIs may experience charge exchange with inflowing interstellar neutral hydrogen to create ENAs at that location with energies of ~ 1 to ~ 5 keV. The ENAs created in the heliosheath appear in both the supersonic solar wind and very local interstellar medium (VLISM) to form an ENA population in both regions. The component in the supersonic solar wind is measured as the direct (non-ribbon) ENA population by the IBEX-Hi instrument (McComas et al. 2009b; Zank et al. 2010; Zirnstein

et al. 2014; Zank 2015). By contrast, the ENA population in the VLISM can experience a first charge-exchange event to produce an energetic PUI there, followed by a second charge-exchange to produce a secondary ENA (McComas et al. 2009b; Heerikhuisen et al. 2010b). There are competing views for the source of ENAs from the ribbon either involving a ring distribution from cyclotron motion about the VLISM magnetic field (Heerikhuisen et al. 2010b), or PUIs being spatially retained in regions where cyclotron wave generation is enhanced due to the neutral solar wind flowing almost perpendicular to the VLISM magnetic field (Schwadron and McComas 2013). The former is referred to as the weak scattering mechanism because it requires the ring distribution to persist without scattering on a time scale comparable to or longer than the ENA production time. The latter provides a spatial region, the Spatial Retention Region, in the VLISM where flux enhancements in PUIs are expected due to a range of possible plasma interactions. The secondary ENA reflects the physical conditions in the VLISM, such as the orientation and strength of the local interstellar medium (LISM) magnetic field, that gives rise to the IBEX ribbon.

Finally, PUIs have a significant role in the thermodynamics of solar wind plasma protons, primarily through energy and entropy transfer. The energy transfer occurs through dissipation of turbulence created by the PUI-excited, low-frequency plasma waves, which heats the solar wind protons and leads to a nonadiabatic polytropic process as they expand in the heliosphere. The resulting temperature profile can be used to determine the polytropic index that characterizes the nonadiabatic process, where the deviation of this index from its adiabatic value provides the turbulent energy (Livadiotis 2018; Zank et al. 2018; Livadiotis and McComas 2023a). The long-range correlations among particles, introduced by PUIs, reduces the system's entropy. The newly generated PUI protons are highly organized and through their interactions with the solar wind plasma protons, affect the nominal kappa-distribution, resulting in a decrease in solar wind flow's entropy. This reduction is quantified by the entropy defect, which is directly related to the value of thermodynamic kappa (Livadiotis and McComas 2023b,c). The derived profile of thermodynamic kappa in the heliosphere was found to match observations from various missions, especially the detailed IBEX skymaps.

PUIs are critical populations in the heliosphere given their contributions to total pressure (McComas et al. 2025a,b) plus the generation of both ENAs and ACRs in the outer heliosphere along with their impact on the thermodynamics of the system. Measuring the in situ velocity distribution functions and isotopic abundances of PUIs at 1 au, together with both the energy, angular, and mass distribution of ACRs and spectrally-resolved maps of outer heliospheric ENAs at PUI energies, enables IMAP to trace the evolution of PUIs at 1 au. Their subsequent influence in regulating the structure and variability of outer heliospheric plasma and energetic particle populations can then be inferred. Additionally, IMAP will enable even more precise and higher resolution determination of the kappa values in the heliosphere.

1.2 Solar Wind Structures

The solar wind plasma that escapes from the Sun carries with it the solar magnetic field creating the interplanetary magnetic field (IMF). The properties of a given solar wind parcel depend on the region from which it was emitted from the solar chromosphere. Coronal holes, which appear as dark regions in extreme ultraviolet (EUV) images of the Sun, emit fast, hot, and low-density solar wind. The slow solar wind associated with coronal streamers, which are bright in coronagraph and eclipse images, is slower, cooler, and higher in density compared to the fast wind.

As the solar wind moves radially away, the Sun's rotation causes the IMF to form the well-known Parker spiral. Deviations from the Parker Spiral occur often in rarefaction and
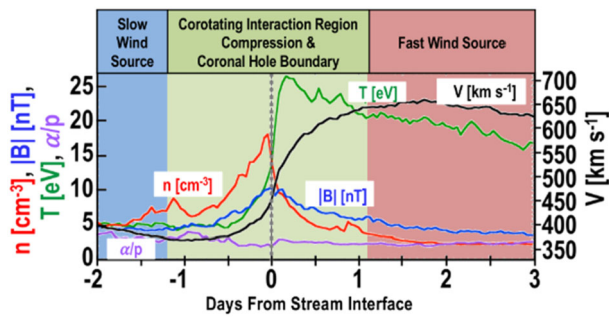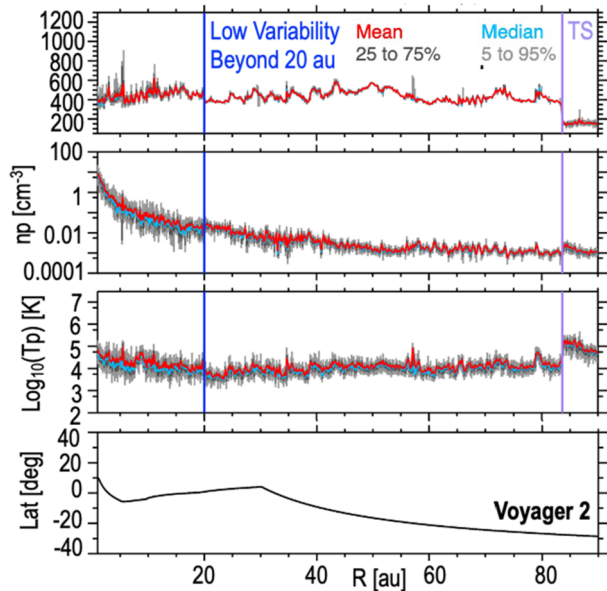
Fig. 1 When fast solar wind runs into slower wind, a compression forms and the density (n), temperature (T), and magnetic field strength ($|B|$) are enhanced. The plot shows a superposed epoch analysis of compressions of solar wind parameters for 27 Corotating Interaction Regions (CIRs), where the x-axis is in days and the events are aligned such that zero is where the solar wind speed (V) for each CIR rose most steeply. Each curve shows the average over all 27 events (Adapted from Borovsky and Denton 2010)

compression regions where the Sub- and Super-Parker Spirals (associated with switchbacks) form due to solar wind speed gradients along field-structures that were connected through magnetic interchange reconnection and footpoint motion back at the Sun (e.g., Schwadron and McComas 2005, 2021). The Sun's rotation can also result in solar wind of differing speeds to be sequentially emitted along a common radial direction. In the case of fast wind following slower wind, the faster wind can push into the slower wind forming a compression region in which the solar wind temperature, density and field strength are elevated (Fig. 1). These compressions are referred to as stream interaction regions (SIRs) or, if surviving over more than one full solar rotation, corotating interaction regions (CIRs). Often once they are somewhat beyond 1 au, the compression regions of SIRs and CIRs turn into fast magnetosonic shocks, which then continue to propagate into the outer heliosphere, driven by the fast solar wind sunward of them.

Coronal mass ejections (CMEs) leaving the Sun also carry with them their own plasma and field characteristics, evident as transient structures in the in situ solar wind measurements. If traveling fast enough, these CMEs can also drive interplanetary (IP) shocks. As the solar wind continues to expand away from the Sun, these solar wind structures (SIRs/CIRs, CMEs, shocks, fast and slow wind) dynamically interact and merge. In this merging process, higher speed solar wind features are worn down and form larger structures with smaller amplitudes. Such merged features are referred to as merged interaction regions (MIRs), or if very large, globally merged interaction regions (GMIRs), which may form a shell extending around the entirety of the heliosphere, at least at lower ecliptic latitudes ($< \sim 30°$) (Burlaga et al. 1993). As the Voyagers have shown, these structures are even capable of surviving all the way out to the heliopause and influencing the local environment of the VLISM (e.g., Burlaga and Ness 2016; Rankin et al. 2019b; Zirnstein et al. 2024). This results in the variability of the solar wind parameters to rapidly decrease with increasing heliocentric distance out to ~ 20 au (Fig. 2). Beyond this, particularly beyond ~ 30 au, the solar wind gradually slows and heats as it encounters an increasing density of interstellar neutral (ISN) material, which is ionized and picked up by the solar wind (Richardson et al. 1995; Richardson and Smith 2003; Elliott et al. 2016, 2019; Wang et al. 2000; Posner et al. 2001; Kim et al. 2016).

Fig. 2 The variability of the solar wind parameters rapidly decreases with distance inside of 20 au as solar wind structures are worn down and merge with one another through dynamic interaction. This figure shows radial profiles of the Voyager 2 solar wind speed, density, and temperature for solar rotation averaged bins (25.38 days). It shows the mean (red), median (blue), 25-75 percentiles (dark grey), and 5 to 95 percentiles (light grey)

1.3 Leveraging in Situ Observations by Other Missions

As with connecting the remote observations of the Sun with in situ data near Earth, the connection between the heliospheric ENA imaging and in situ measurements from IMAP needs to leverage all available resources. Modeling efforts are critical, but any 'ground truth' observations that are available are also necessary. Given the vast size, time-dependent nature, and constitution of the heliosphere, in situ measurements are few and far between, taken at different distances, during different solar cycle phases, and via different instrumentation. However, they can be used as 'stepping stones' to connect different regions of the heliosphere towards a global understanding of the physical processes and conditions at work. While not all measurements of fields and particles (or energy ranges) are available from each spacecraft, any contributions that can constrain the heliospheric models are valuable.

For example, comparing New Horizons solar wind speeds with propagated speeds at 1 au has proven useful for distinguishing reductions in speeds owing to changes in the sources of solar wind at the Sun or to the interaction with and pickup of ISN material. Several outer heliosphere models have already been adapted to have inner boundaries driven with 1 au observations and had success at reproducing these large-scale changes in speed as well as being able to reproduce the gradual slowing trend related to the presence of ISN material (Kim et al. 2016; Keebler et al. 2022).

While the inner heliosphere is better monitored than the outer heliosphere, there is still a dearth of measurements needed to understand the acceleration and transport of particles at and inside of 1 au. IMAP takes advantage of the existing NASA Heliophysics System Observatory (HSO) for context, while augmenting other in situ measurements at L1 with its complete set of instrumentation. In particular, IMAP will join several other missions already positioned at L1 creating an unprecedented spacecraft constellation which will enable unique studies of solar wind mesoscale structures and potentially improving space weather predictive capabilities. Observations from MAG (Horbury et al. 2026), SWE (Skoug et al. 2026), and SWAPI (Rankin et al. 2025) characterize the solar wind plasma and magnetic

field addressing solar wind structures, shocks and turbulence, with GLOWS (Bzowski et al. 2025) contributing to obtaining the solar wind latitudinal structure. SWAPI, along with CoDICE (Livi et al. 2026), also provides critical PUI observations. Suprathermal ions and their charge states are measured by CoDICE which connect to the energetic particle observations of HIT (Christian et al. 2026) with contributions from SEPs, ACRs, and GCRs. As illustrated in Fig. 3, there are a multitude of processes, particle populations, and solar wind structures that make up the global heliosphere. Ubiquitous processes such as shock acceleration can be studied both inside 1 au and in the outer heliosphere through the combination of in situ suprathermal and energetic particle and magnetic field observations, solar and ENA imaging, and theory and modeling that is possible with IMAP.

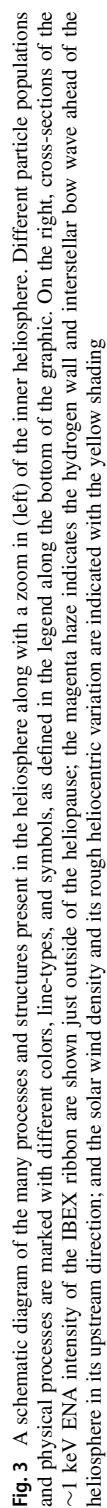## 2 Linking Particle Acceleration and Transport Across the Heliosphere

The physics of heliospheric energetic particles involves two important and interrelated processes: acceleration and transport. Acceleration is the process by which particles gain energy within a collisionless plasma; acceleration is distinct from heating, which only affects the thermal core of the plasma and ultimately results in an increase in the temperature. Two important examples of acceleration associated with collisionless shocks that IMAP studies extensively include IP shocks, which pass by Earth's orbit frequently, and the solar wind termination shock. Other forms of acceleration involve processes related to adiabatic compressions; magnetic reconnection, which is known to occur in the solar atmosphere, solar wind, and possibly in the outer heliosphere as well; and/or energy diffusion (i.e., stochastic acceleration), which typically happens relatively slowly compared to the other processes. With its mass and charge-state resolved observations of particle distributions, IMAP makes critical advances in disentangling the relative importance of these different processes active within the inner heliosphere. Furthermore, by comparing the ENA observations from the outer heliosphere and VLISM with solar and solar wind conditions in the inner heliosphere, IMAP establishes which of those acceleration processes may be active in those distant plasma regimes along the outermost extents of the heliosphere.

The transport of energetic particles is the process by which particles are dispersed in space from their initial acceleration sites. Particle transport involves knowledge of so-called 'transport parameters', such as diffusion and drift coefficients, which are related to the magnetic and electric fields and their fluctuations (i.e., waves and turbulence). Nondiffusive transport, such as that associated with confinement in structures and rapid, advective transport may also contribute to the dispersal of energetic particles, possibly leading to phenomena such as observed particle 'dropouts' (e.g., Mazur et al. 2000). The magnetic fields controlling transport are fundamentally multi-scale, though organized by large-scale solar wind features, they also possess a broadband turbulent component.

In this section, we describe a number of key aspects of this problem for which IMAP makes critical new measurements.

2.1 Solar Wind Structures and Particle Acceleration

The solar wind structures described in Sect. 1.2 occupy a broad range of scales (Bruno and Carbone 2013). The potential for such structures to influence processes at the termination shock depends on at least several effects that vary over such scales. Turbulence at magnetohydrodynamic (MHD) scales, up to around the correlation scale (typically 0.01 au at 1 au),

Fig. 3 A schematic diagram of the many processes and structures present in the heliosphere along with a zoom in (left) of the inner heliosphere. Different particle populations and physical processes are marked with different colors, line-types, and symbols, as defined in the legend along the bottom of the graphic. On the right, cross-sections of the ~1 keV ENA intensity of the IBEX ribbon are shown just outside of the heliopause; the magenta haze indicates the hydrogen wall and interstellar bow wave ahead of the heliosphere in its upstream direction; and the solar wind density and its rough heliocentric variation are indicated with the yellow shading

is expected to be dynamically processed many times over in transition to ∼100 au. This follows from the fact that the nonlinear time, i.e., $T_{nl} = L_c/u$, at 1 au is roughly of order of the correlation scale (L_c, the distance over which fluctuations become statistically independent) divided by the turbulence speed (u). Meanwhile the convection time is R/V for heliocentric distance R and solar wind speed V. Therefore, the structures at the correlation scale or smaller have experienced at least one nonlinear processing time per au of wind motion (Matthaeus et al. 1998). In taking into account the expected increase of correlation scale with distance (i.e., $L_c \sim R^{1/2}$), it is clear that inertial range turbulence structures at $< L_c$ will not survive to reach the termination shock (see, e.g., Cuesta et al. 2022).

On the other hand, structures much larger than the correlation scale may survive partially or wholly intact, in the sense that such structures may follow the large scale flow characteristics over large distances without 'internal' nonlinear distortion due to MHD turbulence processes. This may be roughly quantified by noting that the largest distance an MHD signal at the turbulence speed u can propagate in the convection time R/V in effect defines a "range of influence" $L_0 \sim (u/V)R$. For $V \sim 10u$, the angular opening of influence by MHD processes is $\theta_0 \sim L_0/R \sim 0.1$ radians (∼6°). Structures larger than L_0 at heliocentric distance R will mainly move along large scale flow characteristics, meaning that objects larger than 6° or so are relatively undisturbed by MHD turbulence. This simple calculation suggests that high resolution MHD models (e.g., Usmanov et al. 2025) may contribute to interpretation of IMAP ENA maps, which have similar resolution at most energies.

The above estimates are based on constant speed radial expansion. In reality, the myriad solar wind structures and their variability will distort the large-scale flow characteristics, causing considerable complexity at these mesoscales in the inner heliosphere (r < 20 au). Even in the outer heliosphere, structures such as MIRs have the potential for great influence at mesoscales.

Assessing the impact of various structures on the termination shock environment requires dealing with varying scales differently. One technique for addressing this multi-scale problem is linking a global MHD model at large scales to the photospheric conditions as represented by, for example, data from high-resolution magnetograms. The large-scale models may be single-fluid or multifluid to accommodate additional effects such as differential proton-electron heating as well as parameterized kinetic effects and multiple ion species. Large-scale MHD models are well developed and routinely applied to problems such as space weather.

One may add to such models a statistical representation of the turbulence, which is expected to influence heating and particle scattering and transport, even if it is not treated explicitly. Typically, turbulence in such approaches is described by just a few parameters, including turbulence energy density, cross helicity (i.e., Alfvénicity), ratio of flow kinetic energy to magnetic fluctuation energy, and a correlation length. Some models include several turbulence types, such as quasi-2D fluctuations and slab fluctuations, distinguished by the orientation of the underlying wave vectors. The use of this class of models has increased greatly in the last decade and shows promise in their increasing ability to account for observations by a variety of spacecraft at positions across the heliosphere. These are often called 'turbulence transport models' as they represent significant generalization of Wentzel–Kramers–Brillouin (WKB) theory and include the capability to account for heating through the addition of a temperature transport equation that includes models of turbulence dissipation.

When large-scale models and turbulence transport models are combined into a self-consistent solar wind model, a powerful tool emerges that shows promise to help understand how conditions at 1 au, as monitored by IMAP, can influence conditions in the outer heliosphere. In principle, these kinds of models can propagate shocks, pressure pulses and other

mesoscale structures as well as turbulence properties that determine scattering mean free paths needed for acceleration models. With great improvement in recent years, these models are evolving toward higher fidelity and improved self-consistency, thus becoming an asset in interpreting IMAP's groundbreaking observations. In particular, IMAP in situ observations at 1 au provide explicit constraints on MHD modeling, which then, through numerical propagation to the outer heliosphere, will inform interpretation of IMAP remote sensing data.

Most individual 'events' seen at 1 au by IMAP, except perhaps the largest and most dramatic events, will be fully assimilated into the solar wind turbulence and large-scale structures prior to encountering the termination shock (see, e.g., Fig. 2). Even with improved large-scale and turbulence transport modeling, most of the useful information at 1 au will not map directly to the outer heliosphere, but rather will be of a statistical nature. In this regard, at least several crucial parameters at 1 au are known to be characterized by lognormal statistical distributions. Observed variables displaying (at least, approximate) lognormality include the magnetic field magnitude, the turbulence correlation scales, and the turbulence energy density (Burlaga and Ness 1998; Padhye et al. 2001; Ruiz et al. 2014). This set of parameters encompasses much of what is needed to evaluate charged particle diffusion coefficients. The implication is that these quantities exhibit the same kind of burstiness that is seen in upper atmospheric wind speed, a property that was modeled as lognormal (Obukhov 1962) and inspired the development of intermittency theory (Kolmogorov 1962). Considering just one of these, e.g., a lognormal distribution of correlation scales, it is possible to show that in broad circumstances the resulting composite (or superposed) signal will give rise to a $1/f$ or 'flicker-noise' spectrum (Montroll and Shlesinger 1982). Applying the ideas to IMAP in situ observations, it seems quite likely that interplanetary dynamics in transit to the termination shock will superpose and low-pass filter the inputs at 1 au, resulting in lognormal distributions and $1/f$ noise at very low frequencies (Burlaga et al. 2003; Wang et al. 2024). Such signals are notoriously difficult to predict, as they have equal power per decade, thus delaying convergence of any averaging process. However, by adopting an appropriate statistical approach it may be feasible to interpret the impacts on the termination shock of low-frequency IMAP observations, using large-scale transport models. There is potential in this approach to develop an understanding of the associated response in the form of energization of charged particles.

2.2 PUI Heating and Acceleration

Interstellar PUIs are thought to be the population of particles in the heliosheath with the largest energy density, where most ENAs in the globally distributed flux (GDF) originate. We have a reasonable understanding of the distribution of PUIs in the solar wind through in situ measurements by Ulysses and New Horizons (e.g., McComas et al. 2021, 2025a; Zirnstein et al. 2022a, and references therein). However, we do not have in situ measurements of PUIs in the heliosheath because neither Voyager spacecraft have the instrumentation to measure particles with energies less than about 30 keV. The PLS instrument on Voyager 2 measures ion energies up to 6 keV, which does not cover the hot PUI range, and the lower-energy PUI fluxes are too small to be observed. Thus, we must infer their distribution from the remote observations of ENAs, which only provide a distribution along a particular line of sight over the entire heliosheath, or with numerical modeling which includes the physics of heating and acceleration across the termination shock. These simulations are only limited to the region near the shock and do not provide distributions throughout the heliosheath; however, both Voyager 1 and 2, separated spatially by over 100 AU, have revealed remarkably similar intensities of ∼0.03-1 MeV ions suggesting a certain amount of homogeneity.

Thus, the complete distribution of PUIs at the termination shock, currently only available through simulations, might be a reasonable estimate of that deeper in the heliosheath.

IMAP makes in situ, high-time resolution measurements of select PUI species at 1 au, and determines how their distribution is modified across IP shocks. There are many IP shocks at 1 au, with a variety of parameters, such as speed, Mach numbers, plasma beta, and magnetic field orientation. One important difference between shocks at 1 au and the termination shock is that PUIs dominate the internal plasma pressure in the outer heliosphere, unlike at 1 au (McComas et al. 2017, 2021, 2025a,b). Several authors have shown that interstellar PUIs can modify IP shocks in the outer heliosphere (Zirnstein et al. 2018e; McComas et al. 2021, 2022, 2025a,b; Shrestha et al. 2025). Additionally, at the termination shock, the effective plasma beta (the ratio of the thermal pressure to the magnetic pressure), including the PUI pressure, is very high. As such, those IP shocks for which the ambient plasma beta is large are reasonable analogs to the termination shock. In addition, the inner heliosphere is abundant in pre-existing suprathermal ions with energies from $\sim$1 keV and higher. In some cases, these particles are of sufficient intensity to contribute to the plasma pressure, thereby resembling conditions at the termination shock in which a suprathermal population dominates the plasma pressure. Therefore, we expect there to be IP shocks with plasma conditions analogous to that at the termination shock. This provides important in situ measurements of the evolution of PUIs across shocks with which to compare with distributions inferred from ENAs coming from the heliosheath.

As previously discussed, interstellar PUIs are also the most likely source population for ACRs (e.g., Fisk et al. 1974). Although the specific acceleration mechanism involved remains a topic of some debate (e.g., Giacalone et al. 2012), it is widely thought that acceleration at the termination shock is the primary mechanism (Pesses et al. 1981; Jokipii 1986; Jokipii et al. 2004; McComas and Schwadron 2006; Giacalone et al. 2022). Self-consistent plasma simulations have revealed that as PUIs are heated across the termination shock, a fraction of them are accelerated to higher energies with an intensity that is consistent with in situ Voyager 2 observations (Giacalone and Decker 2010; Giacalone et al. 2021). This is shown in the left panel of Fig. 4. The solid curves are simulated distributions of PUIs just downstream of the termination shock. The blue curve corresponds to the location where Voyager 2 crossed. The black symbols are Voyager 2/LECP data.

A comparison of ENA observations from IBEX and the expected ENA fluxes from the distribution of shock-heated and accelerated PUIs at the termination shock have revealed a discrepancy in the $\sim$3-10 keV energy range (Gkioulidou et al. 2022), which is about the place in phase space where the heated PUI distribution connects with the high-energy tail. A possible solution to this discrepancy was addressed by Giacalone et al. (2025) and is shown in the right panel of Fig. 4. Through a combination of in situ IMAP observations of the evolution of PUI distributions across IP shocks that are analogs to the termination shock, hybrid simulations of the IP shocks with well-determined initial conditions, and new IMAP observations of ENAs in this critical energy range, IMAP helps determine the cause of the discrepancy noted above.

2.3 The Coupling of PUIs to the Solar Wind

It is generally thought that after being ionized, either through charge exchange with the solar wind or by interaction with solar UV, PUIs then scatter rapidly in pitch angle to form a shell-like distribution in phase space. As they are carried outward by the solar wind to the outer heliosphere, they also undergo energy change via interaction with fluctuating electric and magnetic fields, some of which are of their own making due to their distribution being
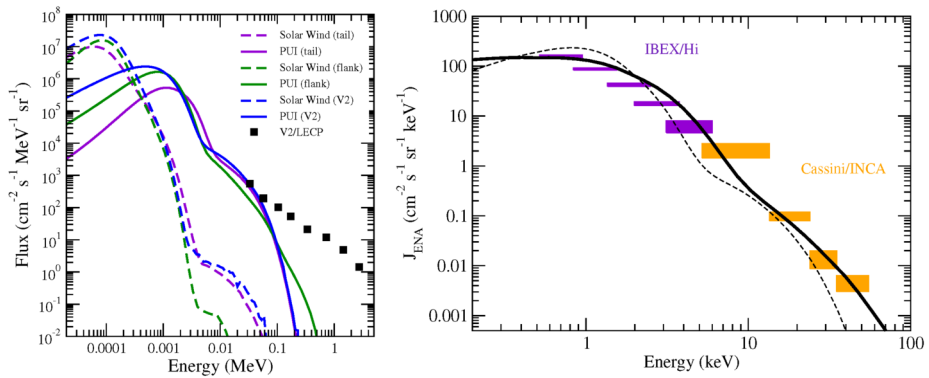
Fig. 4 (left) Energy spectra of solar wind (dashed curves) and pickup protons (solid curves) just downstream of the solar wind termination shock at three different places along the shock: (blue) the Voyager 2 crossing location, (green) at one flank of the heliosphere, and (purple) the tailward direction. The black symbols are data from the Voyager 2 LECP instrument. From Giacalone et al. (2021). (right) The flux of energetic neutral atoms as a function of energy at 1 au based on an estimate using the charged particle distribution obtained from hybrid simulations of the heating and acceleration of pickup protons across the termination shock. The solid and dashed curves are from two different simulations using somewhat different initial pickup proton distributions. The colored boxes from ENA observations from IBEX and Cassini. From Giacalone et al. (2025)

unstable, and through adiabatic cooling. As a result, the quasi-spherical shell distribution becomes filled in the frame co-moving with the solar wind (Fig. 5). In this picture, the PUIs are reasonably 'coupled' to the solar wind in the sense that they have the same bulk velocity as the solar wind, despite having considerably different density and thermal pressure. PUIs respond directly to structures within the solar wind since the PUI sources are generated along the entire streamline. Compressions and rarefactions cause decreased or increased adiabatic cooling, respectively, which increases or decreases PUI densities and pressures (Schwadron et al. 1999). If the scattering is weak, then the PUIs may move along the local magnetic field leading to, for example, a different temperature along the field compared to that across it. In the heliosheath, most models generally assume that the PUI pressure is isotropic and that the PUIs move with the same velocity vector as the solar wind. The two species are assumed to be coupled in this sense and can be characterized in a thermodynamic manner, as the PUI expansive cooling is connected to thermodynamic polytropic processes and the thermodynamic kappa parameter (Livadiotis et al. 2024). Because of the importance of large-scale modeling for our understanding of the global heliosphere, and to aid in the interpretation of ENA GDF observations, it is important that the models include all the essential physics. If the PUIs and solar wind are not coupled in the models, and move as separate populations, this could potentially have important effects on the resulting structure obtained from the models.

IMAP makes in situ observations at 1 au of the full 3D velocity distribution of PUIs from which bulk properties, such as speed, pressure tensor, and density, are determined over a wide variety of plasma conditions. Thus, IMAP studies the coupling of PUIs to the solar wind at 1 au that provides important information that can be related to the physics occurring in the heliosheath, and to guide the physics of large-scale modeling of the heliosphere important for interpreting IMAP observations of ENAs.
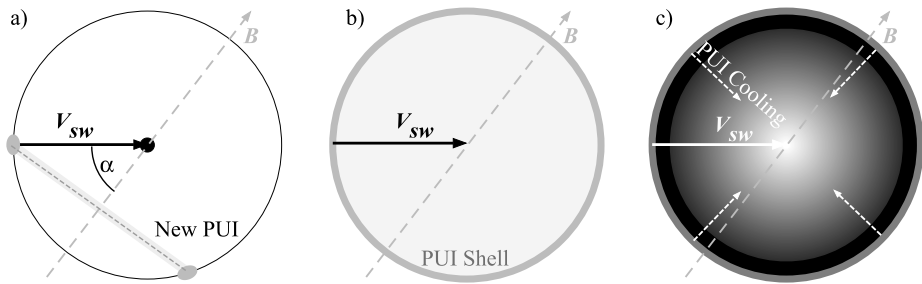
Fig. 5 Diagram illustrating the interstellar pickup ion distribution as the ions are first picked up at α (the angle between the bulk solar wind flow and the interplanetary magnetic field) (*a*), the shell with radius V_{SW} (i.e. the solar wind speed) formed as the ions are pitch angle scattered (*b*), and the shelled filled in response to adiabatic cooling that occurs as the plasma expands (From Fig. 1 in Zirnstein et al. 2022a,b)

2.4 Contributions from Suprathermal Particles

Suprathermal ions in the heliosphere - with energies above the local thermal distribution but below those of energetic particles (typically ∼0.1-100 keV/nucleon for ions, though boundaries vary by context) - come from various sources, such as heated solar wind, interstellar PUIs, and remnants of solar transients (e.g., Mason 2000). This population persists in the heliosphere, forming tails visible in solar wind and energetic particle distributions. These tails can act as the source of seed particles that get selectively injected and accelerated at IP shocks. While the generation process of suprathermal particles remains uncertain, their role in shaping particle dynamics at the termination shock is clear. Voyager observations showed a prevalent cold plasma downstream of the termination shock in the heliosheath, indicating that the primary energy dissipation by the shock is driven by the local energization of suprathermal PUIs, rather than the heating of the thermal solar wind (Zank et al. 1996; Richardson et al. 2008). This observation highlights the strong influence of a locally-energized population of PUIs on the dynamics of the termination shock (e.g., Burrows et al. 2010) and the presence of structures across various spatial scales and regions with diverse plasma turbulence levels (e.g., Richardson et al. 2008 and references there in).

The direct connection between the solar wind structure and ENAs created in the heliosheath (i.e., GDF) and outside the heliopause (i.e., ribbon) has been shown using IBEX ENA observations and solar wind measurements from ACE, Ulysses, and interplanetary scintillation observations (e.g., McComas et al. 2012; Dayeh et al. 2011; Zirnstein et al. 2017). Low-energy ENAs (< few keV) created in the heliosheath thus enable direct observational linkage to 1 au measurements, and provide constraints to validate models aimed at understanding the physical processes at and beyond the termination shock. For instance, IMAP observations enable comparing integrated energy spectra of suprathermal-to-high energy ions observed at 1 au during different phases of solar activity, with the ENA spectra derived from heliospheric ENA maps measured later in time (Zirnstein et al. 2020a) and in different directions of the sky. This in turn quantifies the correlation between 'reservoir' energetic particles present in the inner heliosphere during different solar cycle phases, with those in the heliosheath and near the termination shock, along with their time and solar cycle dependence.

2.5 Interaction of PUIs with Magnetic Field Fluctuations

Interstellar He$^+$ PUIs were first observed by the AMPTE-IRM spacecraft (Möbius et al. 1985) owing to their distinctly broader and continuous velocity distribution functions (VDFs) extending up to twice the solar wind speed (Vasyliunas and Siscoe 1976). These unique VDFs are formed as a result of continuous ionization of ISN He followed by effective pitch-angle scattering in IMF fluctuations and adiabatic cooling in the expanding solar wind (Isenberg 1986, 1987; Möbius et al. 1988; Zirnstein et al. 2022a). The Sun's gravity focuses the incoming ISNs on the downwind side relative to the interstellar inflow direction thus resulting in a longitudinal asymmetry in the ecliptic plane and an increased PUI He$^+$ density within the so-called 'ISN He focusing cone' (Möbius et al. 1985). Since the freshly ionized PUIs form ring-type pitch-angle distributions and achieve speeds that are vector sums of the local ISN flow and solar wind velocities, the cut-off speeds in the solar wind frame are higher on the upwind side (Möbius et al. 1985). The increased density in the ISN He focusing cone (Möbius et al. 1985) along with the cutoff speed enables determination of the symmetry in the PUI cut-off shift and the precise direction of the ISN He inflow longitude (Drews et al. 2012, 2015; Sokół et al. 2016; Möbius et al. 2015; Taut et al. 2018; Bower et al. 2019). However, transport and pitch-angle scattering can produce substantial asymmetries in the observed PUI distributions, e.g., the initial ring distribution can be scattered to form a torus or shell-type distribution, the expected cut-offs at $2V_{sw}$ can broaden, and the energy range where the PUI fluxes are expected to be largest can decrease to just above the solar wind energy (Gloeckler et al. 1994; Möbius et al. 1996, 1998; Chalov and Fahr 2006; Quinn et al. 2016). Additionally, large-scale solar wind structures can influence or even accelerate the PUIs preferentially (Möbius et al. 2019; Gloeckler and Geiss 2001), further modifying their VDFs compared to the freshly ionized population (Lee et al. 2012).

IMAP provides accurate measurements of the 3D VDFs of PUI He$^+$ at sufficient temporal resolution to enable tracking of their evolution after initial injection into the solar wind (e.g., Galvin et al. 2008; Drews et al. 2015). These measurements are used to diagnose the projection of the interstellar flow direction onto the ecliptic plane. In particular, the symmetry in the PUI cut-off shift in the flow axis can be used to determine the ISN flow longitude in the VLISM precisely and complement the ISN flow and gas parameters in the VLISM as inferred from direct measurements of ISNs (Witte et al. 1996; Möbius et al. 2009). Improved temporal resolution of these in situ PUI measurements also unravels details of the acceleration processes at strong IP shocks (e.g., Starkey et al. 2021), and this new information, in combination with state-of-the-art modeling efforts, furthers our understanding of the physics of injection and acceleration of PUIs at the heliospheric termination shock. Finally, tracing the evolution of the He$^+$ VDFs and coordinating with the in situ IMF fluctuations help us understand the transport of PUIs in the heliosheath and how freshly created populations of new PUIs interact with the LISM magnetic field. These observations shed new light into the dynamics of the heliosheath and the topology of the global heliosphere (Izmodenov et al. 2005; Lallement et al. 2005; Pogorelov et al. 2009; Opher et al. 2009), and help constrain models of the origin of the ENA ribbon (McComas 2009a; Schwadron and McComas 2010; Heerikhuisen et al. 2010a; McComas et al. 2014).

Moreover, IMAP provides compositional measurements of inner source PUIs, a population produced close to the Sun that is distinct from interstellar PUIs (Geiss et al. 1995; Gloeckler et al. 2000). Their low ionization potentials suggest their origin is not coronal, but rather from interactions between the solar wind and interplanetary dust grains (Gruntman 1996; Schwadron et al. 2000; Allegrini et al. 2005; Szalay et al. 2021). IMAP's observations of this population will advance our understanding of dust–plasma interactions close to

the Sun and help constrain the composition, size distribution, and spatial extent of near-Sun dust.

2.6 The Effect of Energetic Particles on Shocks

Energetic particles accelerated at collisionless shocks affect the upstream plasma resulting in feedback onto and modification of the shock itself. For example, ion foreshock regions are observed routinely at supercritical planetary bow shocks (e.g., Eastwood et al. 2005); these regions are characterized by suprathermal ions back-streaming from the shock into the incident solar wind. This additional beam of suprathermal ions, accelerated and reflected along the shock, interacts with the solar wind, resulting in a variety of waves and nonlinear feedback mechanisms that ultimately contribute to the energy budget and dissipation at quasi-parallel shocks (e.g., Trotta et al. 2021 and references therein). Foreshock ions only manifest upstream of quasi-parallel shocks, since it is only there that they are able to outrun the shock in its own rest frame, while electron foreshocks extend much further into the quasi-perpendicular regime since, at typical suprathermal energies in the solar wind, electrons are moving substantially faster relative to the shock itself. The dynamics of the foreshock modify the structure of the shock itself, with transient, large-amplitude magnetic structures (e.g., Schwartz et al. 1992; Caprioli and Spitkovsky 2014) and other, explosive foreshock phenomena (e.g., Schwartz et al. 2018; Turner et al. 2020) that form in the upstream and impact the local shock, often resulting in very effective enhancements in energetic particle acceleration (e.g., Liu et al. 2018; Turner et al. 2018; Raptis et al. 2024). IMAP will measure numerous interplanetary shocks and observe such phenomena.
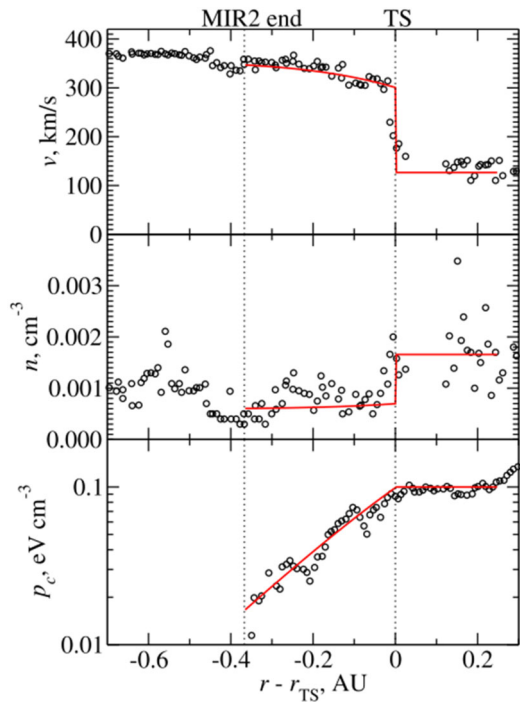
Recent simulations (e.g., Caprioli and Spitkovsky 2014; Haggerty and Caprioli 2020) have demonstrated how the kinetic physics of the ion foreshock results in the formation of nonlinear magnetic field amplifications and distinct deviations of the shock pressure balance and energy budget compared to that expected from pure MHD. For continuously driven shocks, like the heliospheric termination shock or the planetary bow shocks, the ion foreshock is always present upstream of the quasi-parallel shock. However, for transient shocks, like those associated with CMEs, the shock must slow down as it dissipates energy over time through sheath formation and energetic particle acceleration. Thus, the Mach number of CME shocks decreases as they propagate further in heliocentric distance (e.g., Cuesta et al. 2024 and references therein). As mentioned earlier, the frequency and variety of CME shocks at 1 au may result in some that are suitably analogous to the termination shock, providing an opportunity to examine how energetic particles may affect shocks in the outer heliosphere.

In fact, Voyager 2 termination shock observations provide evidence of energetic particles mediating the shock. Plasma measurements prior to the Voyager 2 termination shock crossing showed a clear decrease in the solar wind speed (Fig. 6). Florinski et al. (2009) show that the inward ACR pressure gradient is large enough to cause the solar wind deceleration that occurred 40 days prior to the termination shock crossing. With its comprehensive suite of in situ particle and plasma instruments, IMAP contributes to our understanding of how SEPs modify the structure and energy budgets at CME shocks and provide a more complete basis for interpreting the plasma observations at the termination shock.

2.7 Connecting in Situ Observations with the Physics of PUIs in the Ribbon

IBEX observations (McComas et al. 2009b) support a class of ribbon models based on the creation of plasma in the VLISM from neutral (secondary) solar wind. This secondary ribbon source was modeled in numerous studies (Chalov et al. 2010; Heerikhuisen et al. 2010b;

Fig. 6 Prior to the Voyager 2 termination shock crossing there was a precursor to the termination shock where the solar wind speed began to steadily decrease as the energetic Anomalous Cosmic Ray (ACR) ions increased. This figure shows the solar wind speed, density and the partial pressure determined from the measured distributions from the LECP instrument for the 2007 Voyager 2 termination shock crossing. The vertical dotted lines mark the end of the merged interaction region (MIR2) and the crossing of the termination shock (TS). Red lines show fits based on two-fluid gas-dynamic conservation laws (for more details see Florinski et al. 2009)

Möbius et al. 2013; Zirnstein et al. 2018a). Secondary ribbon models have two major variants: ring-beam (weak scattering) models (e.g., McComas et al. 2009b; Chalov et al. 2010; Florinski et al. 2010; Gamayunov et al. 2010; Heerikhuisen et al. 2010b; Liu et al. 2012; Möbius et al. 2013; Zirnstein et al. 2018a,b,c,d) and models involving the spatial retention of protons in the VLISM (Schwadron and McComas 2013; Isenberg 2014; Giacalone and Jokipii 2015).

The first variant of secondary ribbon models relies on ring-beam distributions created in the VLISM from solar wind neutrals that move out roughly perpendicular to the VLISM magnetic field. Once ionized, the PUI ions gyrate about the magnetic field, and when reneutralized, some fraction of the particles in the ring-beam move back toward IBEX and IMAP, where they are observed. This produces a ribbon that is aligned in directions where the neutral solar wind directed radially outward (r) is almost perpendicular to the VLISM magnetic field (B), where $B \cdot r \sim 0$. There are few measurements with sufficiently tight energy and angular resolutions to measure the ring-beam distribution directly (Drews et al. 2015; Oka et al. 2002). IMAP can identify the PUI ring-beam using in situ measurements, and determine the rate of PUI pitch-angle scattering based on the intensity of the PUI ring. These observations will be used to better understand the plasma physics associated with PUI scattering, which has direct applications for the plasma, turbulent, and wave-particle instabilities at work in the ring-beams that form the ribbon beyond the heliopause.

The second variant of ribbon models relies on pickup-wave instabilities or other larger-scale magnetic field variations that retain pickup ions in the spatial region near the $B \cdot r \sim 0$ surface in the VLISM (Schwadron and McComas 2013). Newly ionized atoms can be retained through increased rates of scattering by locally generated hydromagnetic waves through a well-known PUI instability (Lee and Ip 1987). The 1 au in situ PUI observations on IMAP provide the opportunity to resolve the relationship between PUI streaming, the

PUI hydromagnetic instability, and the turbulent state of the solar wind. Isenberg (2014) took a step in this direction by describing turbulence beyond the heliopause based on a model for turbulent heating driven by the slow pickup of protons in the solar wind 10's of au from the Sun. Application of a simple model of this process yielded a ribbon structure that is qualitatively similar to the IBEX ribbon.

3 Heliospheric Variability

Structures such as those described in Sect. 1.2 lead to variability in the heliosphere which in turn affects the global structure of the solar wind, the acceleration and transport of energetic particles and ultimately the characteristics of the created GDF and ribbon ENA populations. Combining IMAP ENA and in situ data with in situ measurements from missions, such as New Horizons, well beyond Earth's orbit (as well as sophisticated modeling efforts) enables studies that significantly advance our understanding of the global heliospheric system. Some examples of these studies are described below.
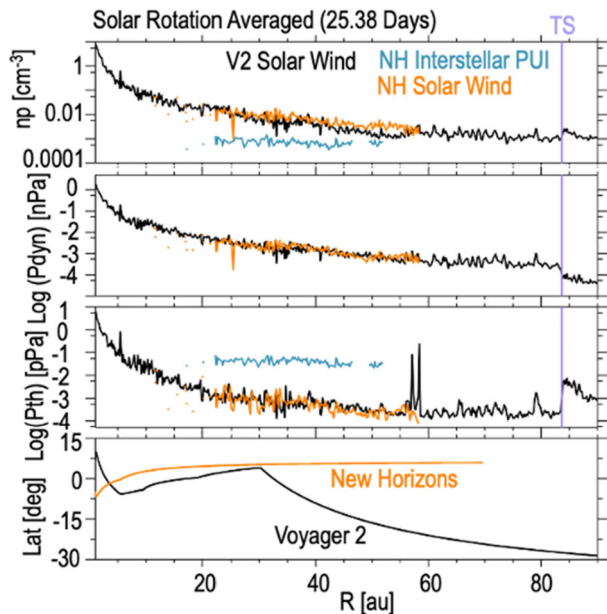
3.1 Evolution of the Solar Wind

3.1.1 Radial Evolution of the Solar Wind

Beyond the orbit of Earth, the expansion of the solar wind causes the density and both the dynamic and thermal pressures to decrease with distance (Fig. 7). However, New Horizons' SWAP instrument (McComas et al. 2008b) has shown that beyond 20 au, interstellar PUIs dominate the thermal energy of the solar wind, keeping the SW+PUI plasma mixture relatively hot (McComas et al. 2021, 2025a). The supersonic solar wind ends when it crosses the termination shock that forms sunward of the heliopause. At the termination shock, the solar wind is forced to slow, is compressed and heated, and starts to divert in direction around the inside of the heliopause and flow down the heliotail (McComas et al. 2013). Voyager 2 termination shock observations showed that the solar wind speed sharply decreased from 300 to 120 km/s and the density rose by the same factor, but the thermal plasma downstream of the termination shock was only heated to $\sim 10^5$ K (Fig. 2). While the solar wind thermal ions experienced slowing and compression at the termination shock, only 20% of the solar wind flow energy heated the thermal solar wind plasma, while the remaining 80% went into heating non-thermal particles. About 15% went into heating energetic particles, and the rest heated the interstellar PUIs (Richardson et al. 2008). This led to the solar wind remaining supersonic in the heliosheath with respect to the thermal plasma because the interstellar PUIs determine the sound speed.

New Horizons, which is currently at ~ 60 au, can measure the PUIs directly and has enough power to reach the termination shock (Stern et al. 2019). New Horizons' SWAP instrument will be the first to quantify the interstellar PUI's dominant thermal pressure beyond the termination shock, since the Voyager spacecraft could not measure the interstellar PUIs directly. This will also be the first time that in situ measurements of PUIs in the heliosheath are made in conjunction with heliosheath ENAs measured by the IMAP imagers. It is not known when New Horizons might encounter the termination shock, but some models suggest it could be as early as the first half of 2029 (Bera et al. 2025).

Fig. 7 The spherical expansion of the solar wind produces a distinct decreasing profile in the solar wind density, dynamic pressure, and thermal pressure. The interstellar PUI thermal pressure is much larger than the solar wind thermal pressure in the outer heliosphere. These radial profiles are solar rotation (25.38 days) averaged solar wind density, dynamic pressure, and thermal pressure measurements from Voyager 2 (black) and New Horizons (orange). The bottom panel shows the latitude of each spacecraft. The interstellar PUI densities and thermal pressures measured at New Horizons are also shown (blue) (From Richardson et al. 2022, but with fewer panels and updated to include new measurements)

3.1.2 Latitudinal Structure of the Solar Wind

We have a comprehensive understanding of the solar wind properties in the ecliptic plane owing to in situ measurements. However, its latitudinal structure has only been observed in situ by the Ulysses/SWICS experiment (Bame et al. 1992) between 1992 and 2007. Mc-Comas et al. (2000) demonstrated that during the phase of high solar activity, the slow and dense wind expands to all heliolatitudes, and during low activity, the fast and rarefied wind blows at all heliolatitudes except for an equatorial band of $\pm \sim 30°$. These observations also showed that the solar wind ram pressure or the total mechanical energy flux seem to be latitudinally constant during a given time, even though their absolute magnitudes vary with time (Lee et al. 2012).

Since the end of the Ulysses mission, the insight into the helio-latitudinal structure of the solar wind has solely relied on indirect remote sensing observations. One of these sources of information is the interplanetary scintillation (IPS) method (Hewish et al. 1964; Jackson et al. 2011), which uses scintillation of radio waves emitted by astrophysical compact sources resulting from fluctuations of the solar wind electron density which vary with the solar wind speed. Using tomography analysis (Jackson et al. 2011; Tokumaru et al. 2021) on measurements of these fluctuations observed by several geographically separated ground stations returns latitudinal profiles of the solar wind speed at 1 au. Synoptic maps of the solar wind speed have been available continuously since 1987; although, with considerable gaps in coverage (Sokół et al. 2015; Porowski et al. 2022). These data have been used by Sokół et al. (2015, 2016), Sokół, Bzowski and Tokumaru (2019), Sokół et al. (2020) and Porowski et al. (2022, 2023) to construct empirical models of the evolution of the solar wind velocity with heliolatitude for 1987 - 2022, with a time resolution of one speed profile per year, and then linearly interpolated to a Carrington Rotation cadence as a final product of the analysis. The use of the invariant solar wind mechanical energy flux yields also the evolution of the solar wind density for this interval.

Another analysis method uses observations of the solar Lyman-α radiation resonantly scattered on interstellar neutral hydrogen atoms within the heliosphere, commonly known as the heliospheric backscatter glow or the helioglow. The distribution of the helioglow intensity in the sky depends on the spatial distribution of the interstellar hydrogen density within a few au from the Sun (e.g., Kubiak et al. 2021a,b) and is shaped by photoionization and the interaction of interstellar hydrogen atoms with solar wind protons via charge exchange. The solar Lyman-α radiation is responsible on the one hand for the radiation pressure force, modifying the distribution of interstellar hydrogen, and on the other hand for the illumination of this gas and creation of the helioglow (see review by Bzowski et al. 2013). The helioglow modulation is thus directly linked to the solar wind latitudinal structure and its evolution during the solar activity cycle.

Full-sky observations of the helioglow have been used to infer the latitudinal structure of the solar wind (Lallement et al. 2010; Katushkina et al. 2013, 2019; Koutroumpa et al. 2019) observed by SOHO/SWAN (Bertaux et al. 1995). These authors obtained latitudinal profiles of the solar wind at a resolution on the order of days owing to their analysis of all suitable helioglow maps, which are available at a cadence of several per week. Bzowski (2003) and Bzowski et al. (2003) suggested a method of establishing the solar wind structure from helioglow observations collected along carefully selected heliocentric rings. Bzowski et al. (2003) used this method to derive the solar wind structure evolution from solar minimum to maximum and obtained results in qualitative agreement with those obtained for the same interval from in situ measurements.

The conclusions on the evolution of the latitudinal structure of the solar wind drawn from IPS versus helioglow observations have been pointed out to be somewhat inconsistent, with the two methods producing different solar wind profiles for times where analyzed times overlapped (Katushkina et al. 2013, 2019). The helioglow analysis suggested that solar wind speed or flux frequently features clear maxima at mid-latitudes during solar maximum. This feature was noticed in a few cases in the IPS analysis (Sokół et al. 2020; Porowski et al. 2022), but not on a regular basis. Also, it had not been seen by Ulysses, but given the point-like character of these latter observations and the long pole-to-pole cadence, such a feature could be challenging to identify. IMAP measures the helioglow more precisely than before possible, allowing resolution of the presence of solar wind maxima. If their existence is confirmed, this will be a qualitative change in the understanding of the global solar wind output.

3.1.3 Temporal Evolution of the Solar Wind

Understanding the solar wind structure and its temporal evolution is fundamental for understanding the global-scale production of PUIs. McComas et al. (2019a,b) demonstrated a time-delayed correlation between the variation of the solar wind measured in the inner heliosphere and the ENA fluxes observed by IBEX (see Fig. 9). Reisenfeld et al. (2016, 2019, 2021) and Zirnstein et al. (2022b) pointed out that with an appropriately accounted evolution of the solar wind, it is possible to determine the size and shape of the heliosphere based on the observed variation in the sky distribution of the global ENA fluxes.

The relation between the solar wind structure and ENAs is two-tier. Firstly, the ENA production varies with the modulation of the solar wind density and speed, with a location-dependent delay. The propagation time of the solar wind to the termination shock varies approximately by a factor of 2, between ~12 and 6 months, as the solar wind speed varies between ~400 and ~750 km s^{-1} (see Sect. 3.2.1 and Fig. 8). The fast wind is limited to polar regions and times of low solar activity. The global speed variations are correlated with

those of the density, with the lower magnitudes of the density related to the fast solar wind. The creation of the ENAs due to the solar wind forcing takes some time, approximately 2 years after the parent solar wind ions and PUIs, carried by the supersonic solar wind, cross the termination shock. Once created, some ENAs travel back toward the Sun, where they are detected at 1 au. The seed population for the ENAs able to reach 1 au, i.e., solar wind ions and PUIs, depending on the ENA energy, are created inside the termination shock, but compressed and heated at the termination shock and subsequently neutralized in the heliosheath. Secondly, these ENAs are subjected to re-ionization losses in the supersonic solar wind (Bzowski 2008). The magnitude of these losses varies between ∼70% for the lowest-energies ENAs (0.3 keV) observed to come from within 60° around the Sun to just ∼1% for the highest energy ENAs at ∼300 keV. Most of these losses are incurred within a few au from the Sun and are due to charge exchange with solar wind protons. Thus, the magnitude of the losses depends on the structure of the solar wind just before the ENA detection.

Investigating these processes is one of the science objectives of the IMAP mission. Insight into the context of the global solar wind is an essential part of these studies. Existing models of the solar wind structure based on IPS observations have had an effective time resolution of one year, i.e., comparable to the travel time of the solar wind from its source to the termination shock. IMAP measures the helioglow with higher temporal cadence and lower background than previously available observations and thus, has the capability to monitor the evolution of heliolatitudinal profiles of the solar wind at a time cadence on the order of a solar rotation period, i.e., a month, contemporaneous with ENA observations and in situ measurements of the solar wind in the ecliptic. With this, much more precise timing of the solar wind forcing and the ENA response signal will be obtained, provided that data for a time interval comparable to that of the solar cycle length are available.

3.2 Time-Delayed Inner/Outer Heliospheric Connections

3.2.1 Impact of GMIRs and Pressure Pulses on the Outer Boundaries

Fast CMEs and SIRs/CIRs drive pressure pulses through the solar wind, through the heliosheath, out to the heliopause, and beyond into the VLISM. These pressure pulses encounter the heliopause and drive shocks into the LISM. The Voyager 2 pressure pulses have also been correlated with electron plasma oscillations in the VLISM that are driven by these shocks (Richardson et al. 2022). They also drive anisotropic disturbances of cosmic rays (Rankin et al. 2019a,b). As mentioned earlier, in the outer heliosphere these shocks evolve into broad GMIRs lasting a few months with pressure increases of up to a factor of 10. These pressure pulses were observed by Voyager 2 near solar maximum (from 2000 to ∼2005) at distances from 60 – 75 au, and are reproduced by simulations (e.g., Wang and Richardson 2005). A solar cycle later, Voyager 2 was in the heliosheath and observed wider (6 month-long) pressure pulses with magnitudes of up to a factor of 3. Plasma densities, ACR, and GCR intensities were strongly correlated in the heliosheath with changes up to 50%. These changes are expected to drive emissions of the ENA fluxes, which should be observed by IMAP's three ENA imagers. As has been done with IBEX (Reisenfeld et al. 2021; Zirnstein et al. 2022b), the impacts of GMIRs and large pressure pulses on the heliospheric boundaries can be used by IMAP, with its better temporal resolution and energy range, to calculate the sizes of these boundaries based on the 'sounding' method originally developed for IBEX data (Reisenfeld et al. 2021).

To understand this inner/outer heliospheric connection, one must consider the propagation times for the various signals (i.e., drivers of information) between the Sun, 1 au, and the
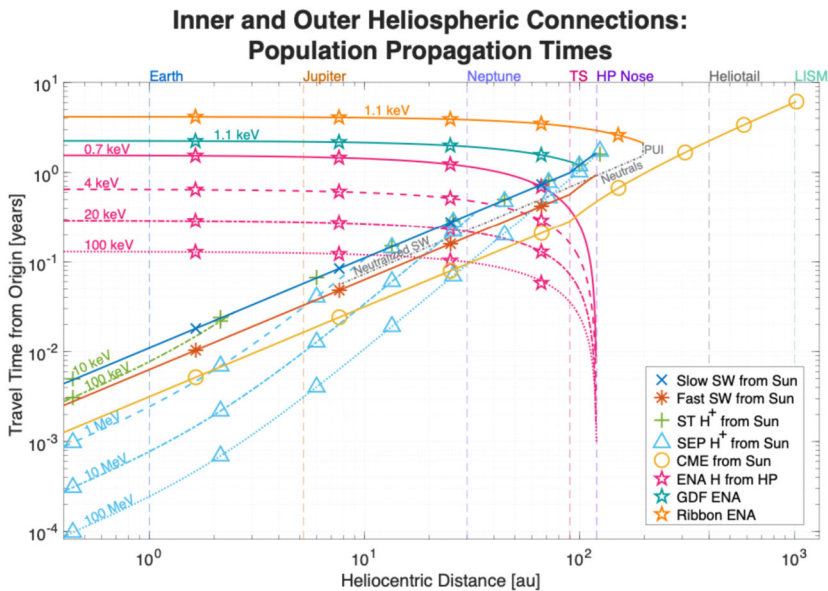
Fig. 8 Travel times for various species and populations throughout the heliosphere and beyond. Slow solar wind (SW) of 430 km/s, fast SW of 750 km/s, CMEs, and suprathermal (ST) and SEP protons (H^+) are all shown originating from the Sun and traveling outward in heliocentric distance. Multiple energies are shown for the following populations: ST and SEP protons and ENAs. ST protons are shown for 10 and 100 keV; SEP protons are shown for 1, 10, and 100 MeV. Travel times for both ST protons and SEPs are calculated assuming that those particles travel along the Parker spiral IMF, but note that for ST and SEP protons, when those populations intersect with the slow SW curve (i.e., where their outbound propagation parallel to field lines becomes slower than the radial motion of the SW convection flow), their outbound motion becomes dominated by SW convection and move essentially 'frozen-in' to the SW. For inbound populations, hydrogen ENAs are shown originating from the heliopause at 120 au and traveling inward. ENAs are shown at: 0.7, 4.0, 20, and 100 keV. For all populations with multiple energies, the slowest to fastest are shown with thick, solid, dashed, dash-dot, and dotted lines. Additional 1.1 keV ENA curves are shown originating from the heliosheath, representing the GDF ENA population, and the very local interstellar medium, representing the IBEX ribbon ENA population

outer reaches and boundaries of the heliosphere and VLISM. Figure 8, shows some representative, estimated travel times for various species and populations from the inner to outer heliosphere and LISM and vice versa. For example, a CME traveling at 1000 km/s takes 17 days to reach Saturn, ∼140 days to reach the termination shock, and 260 days to reach the heliopause (accounting also for slowing across the shock). Looking at inbound species, with respect to the Sun, hydrogen ENAs at 100 eV and 100 keV take ∼380 and ∼12 days, respectively, to transit from the nose of the heliopause through the heliosheath to the termination shock; at those same two energies, hydrogen ENAs take ∼4.1 years and ∼47 days, respectively, to transit from the nose of the heliopause to Earth at 1 au. GMIRs form around 10 au, and from there, estimating a speed of 500 km/s, GMIRs take ∼280 days to reach the termination shock and another ∼140 days to reach the heliopause. Such time delays are critical to consider when studying the time history of ENAs observed by IMAP, particularly with the improved temporal resolution for ENA maps.

IBEX observations from McComas et al. (2018b) demonstrated that the 4.3-keV ENA emissions have a ∼2–3 year delayed response to significant changes in the solar wind dynamic pressure observed at 1 au (Fig. 9), and that these changes were visible in ENAs down
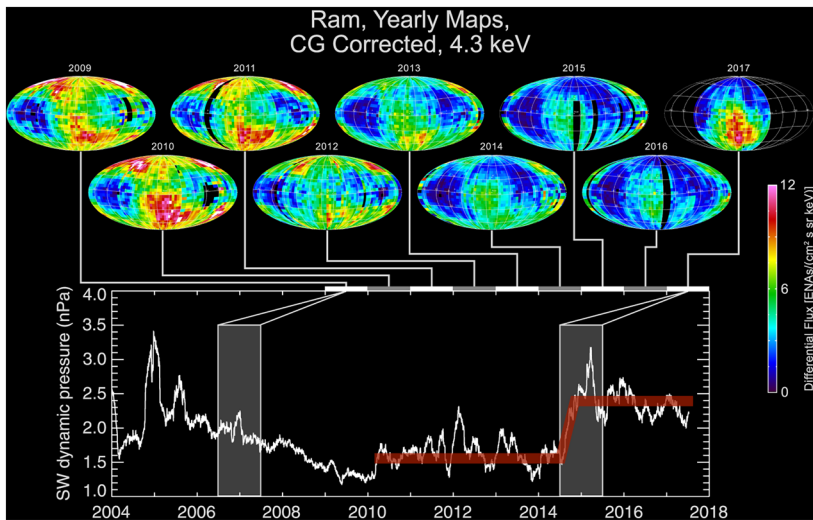
Fig. 9 Shown are the IBEX Ram, CG-corrected 4.3 keV ENA maps as an example. There are significant changes in the outer heliosphere 4.3 keV ENA emissions over the course of the solar cycle as the solar wind dynamic pressure changes. The top panel shows the 4.3 keV ENA differential flux from 2009 to 2017 as Mollweide projection maps centered on the direction of the inflowing interstellar gas. The bottom panel shows the corresponding time series of the solar wind dynamic pressure. The 4.3 keV ENA differential flux has a ∼2–3 year delayed response to large changes in the solar wind dynamic pressure (from McComas et al. 2018b)

to at least 1.74 keV, with longer response times. This delayed response can be understood when the transit times for the solar wind and ENAs are considered. From Fig. 8, the solar wind takes ∼0.9–1.6 years (for fast and slow solar wind) to transit from 1 au to the nose of the heliopause, where it can modify the production of ENAs, as observed by IBEX. At 4.3 keV, an ENA takes at least another 0.3 years to travel back to 1 au from the nose-ward side of the heliopause. Accounting for some additional time for the pressure wave to travel to the heliopause and partially reflect back into the heliosheath, the observed 2–3 year delayed response is reasonable (Zirnstein et al. 2018b). For secondary ENAs that come from outside the heliopause (i.e., the secondary ENA model of the IBEX ribbon; McComas et al. (2009b)), Schwadron et al. (2018), for example, showed evidence in support of this secondary ENA model using a combination of in situ data from 1 au alongside IBEX ENA GDF maps versus ENA ribbon maps and accounting for the different time lags between the two populations of ENAs with respect to changes in the inner heliospheric solar wind (e.g., Fig. 10).

With its combination of comprehensive in situ observations at 1 au plus comprehensive and higher-resolution ENA imagers, IMAP promises to drastically improve upon our preliminary understanding of the connections between the inner and outer heliosphere and the LISM. ENA all-sky maps from IMAP are produced on at least a 6-month cadence, with significantly improved counting statistics compared to IBEX (e.g., McComas et al. 2018a). IMAP in situ instruments measure the solar wind pressure variations and transient structures (CMEs, CIRs/SIRs) and PUIs at 1 au, all of which propagate outward into the outer heliosphere and affect ENAs (both GDF and ribbon populations). Thus, correlation studies like those presented by McComas et al. (2018b) and Schwadron et al. (2018) are conducted with IMAP on a faster cadence and with higher time resolution than with IBEX.
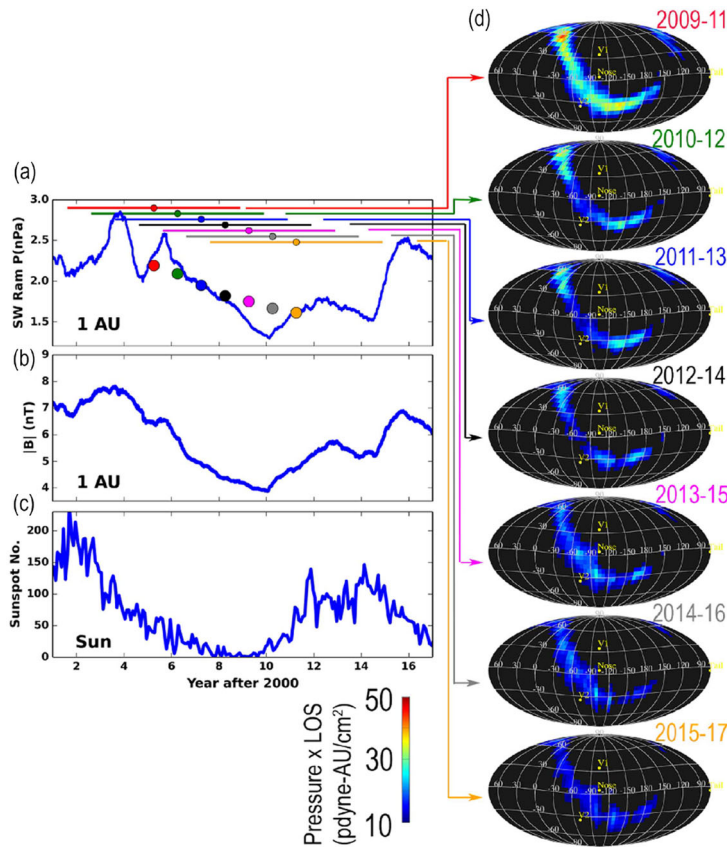
Fig. 10 Transit-time corrections applied to the LOS-integrated pressure maps of the ribbon observed by IBEX over 9 years of data. Panel (a) shows the SW dynamic pressure at 1 au, and panel (b) shows the magnetic field magnitude at 1 au, both from OMNI data. Panel (c) shows the sunspot number. Panel (d) shows the LOS-integrated pressure maps of the IBEX ribbon. In panel (a), the colored horizontal lines correspond to the time periods over which solar wind conditions observed at 1 au affect conditions in the heliosheath observed in corresponding LOS-integrated pressure maps. Finally, the large colored dots in panel (a) show the average ram pressure over the time periods indicated by the colored horizontal lines. Reproduced from Schwadron et al. (2018)

3.2.2 Solar-Cycle Dependencies of ACRs and GCRs at 1 AU

By the time both ACRs and GCRs penetrate to 1 au, their flux has been heavily modulated enroute depending on the solar cycle and the corresponding global magnetic configuration, presence and number of large-scale solar wind transients, and solar magnetic polarity (see, e.g., reviews by Rankin et al. 2022 and Giacalone et al. 2022). When the solar magnetic field is outward in the northern hemisphere, this solar configuration/state is referred to as being A>0 (i.e., white background intervals in Fig. 11). For the A>0 solar minimum intervals, the maximum intensities of positively-charged ACR and GCR ions are relatively 'flat', i.e., constant with time for an extended period. When the field points outward in the southern hemisphere during solar minimum conditions corresponding to the A<0 (i.e., gray background intervals in Fig. 11), the intensity maximum is of shorter duration, i.e., more 'peaked'. For the A<0 cycles, particles drift into the heliosphere along the heliospheric cur-
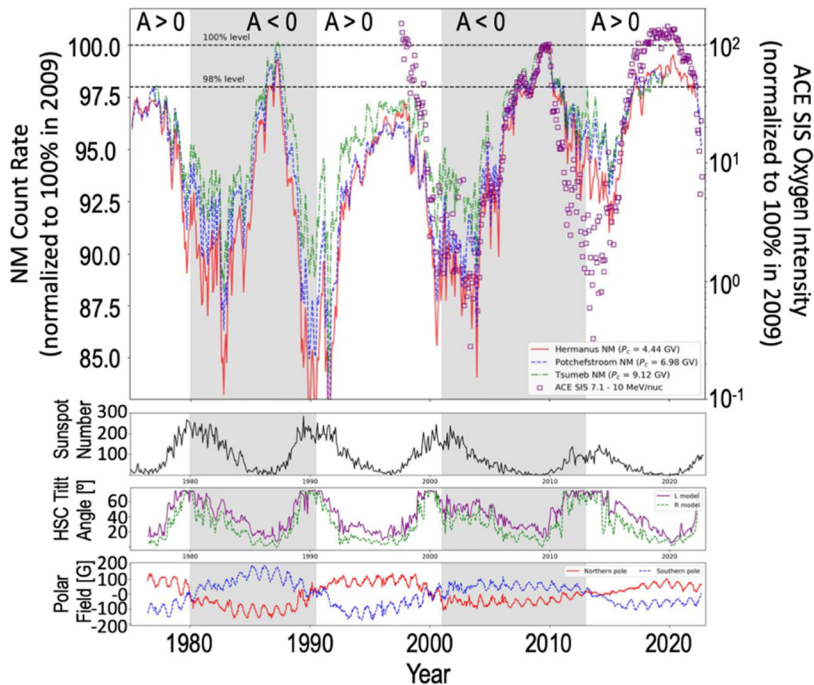
Fig. 11 In the top panel are several time series curves all scaled to 100% in 2009. There are 3 neutron monitor curves for stations in South Africa with cutoff rigidities of 4.44 GV (red), 6.98 GV (blue dash) and 9.12 GV (green dot dash) and one curve with ACE SIS Oxygen Intensity (purple squares). The bottom 3 panels provide the corresponding time series for the monthly sunspot number, heliospheric current sheet (HSC) tilt angle determined using either the classic line-of-sight boundary conditions (purple) or radial boundary conditions at the photosphere (green), and the polar field strength for the north (red) and south (blue) poles. The grey background indicates A<0 and the white background indicates A>0 (Adapted from Figs. 1 and 2 in Strauss et al. 2023)

rent sheet whereas during the A>0 cycle the particles drift in from the poles and drift out along the heliospheric current sheet (Jokipii and Thomas 1981; Kota and Jokipii 1983). The observed modulation of ACRs and low-energy GCRs measured in situ by IMAP at 1 au, which can also be connected to the thermal and interstellar PUI behavior which reflect not only large-scale solar wind transients but also the solar cycle, are likely to affect the high energy ENAs observable by IMAP. With their fast travel time, high energy ENAs are an important observable to probe the outer heliosphere for large-scale solar wind changes that may affect the propagation of ACRs through the heliosphere.

3.3 Turbulence in the Outer Heliosphere

Turbulence is important on global scales particularly beyond 20-30 au in the supersonic solar wind where PUI-driven instabilities produce much of the turbulence, which ultimately heats the thermal plasma. Fraternale et al. (2022) provide a thorough review of turbulence in the solar wind in the outer heliosphere, in the solar wind, the heliosheath, and the LISM. PUI distributions are non-uniform, with higher fluxes in the nose than tail; therefore, energy cascade rates are also non-uniform. In the nose region they decrease until about 20 au, then slowly increase, and in the tail region they decrease until 30 au, then flatten, as has been
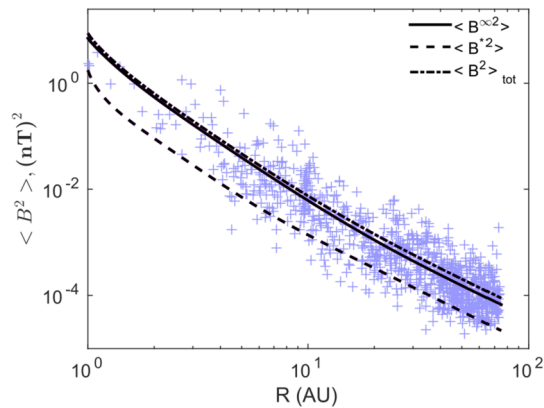
Fig. 12 Turbulent magnetic fluctuation energy as a function of distance from 1 au out to the termination shock (from Zank et al. 2018). Plotted are three theory curves showing the fluctuating magnetic energy density in quasi-2D turbulence <B2> (solid black line), slab turbulence <B*2> (dashed line), and their total <B2> tot (dash-dotted line). The blue crosses denote the transverse magnetic field fluctuations observed in the outer heliosphere by Voyager 2. The observations and theory show that the creation of PUIs in the distant heliosphere augments the existing solar wind turbulence

shown theoretically by Adhikari et al. (2017). The fluctuating magnetic energy is displayed in Fig. 12, indicating that theory and observations are consistent (Zank et al. 2018).

The termination shock is a major source of turbulence for the inner fheliosheath (Zank et al. 2018, 2021). Before the termination shock, PUI-generated turbulence augments the pre-existing or embedded solar wind turbulence, which is amplified locally as it transmitted across the heliospheric termination shock by about a factor of 10 or more (Zank et al. 2021) and, if the termination shock is locally oblique, by reflected particle-driven turbulence (Lembège et al. 2020). Thus, the shock amplifies both pre-existing solar wind and locally-generated turbulence as it enters the heliosheath. Anisotropic plasma distributions, particularly those of PUIs (e.g., Lembège et al. 2020), can also be generated by shock waves in the outer heliosphere, including at the heliospheric termination shock, which results in the driving of instabilities that produce more turbulence.

The best evidence of turbulence in the heliosheath and LISM is the observation of intermittency of magnetic field fluctuations, power-law regimes for spectra and higher-order structure functions, and multifractal statistics. The generation and propagation of turbulence in the heliosheath is essential for understanding the GDF ENAs produced there. It has been demonstrated that either a high amount of turbulence at the termination shock (Zirnstein et al. 2021) or in the heliosheath (Zirnstein et al. 2018c,d) may be the key to understanding the ENA spectral observations from IBEX, and soon IMAP. Turbulence can lead to diffusive heating of PUIs in the heliosheath, which may account for the 'gap' problem in ENA fluxes between models and data (Gkioulidou et al. 2022). Several scenarios have been proposed to 'fill' this gap (Giacalone et al. 2025) but so far, no consensus has been reached. With the IMAP ENA imagers' enhanced capabilities and wider energy range, more data are available to analyze and determine how turbulence affects the parent particles of ENAs.

The ISM is turbulent on scales up to 1000 pc (Lee and Jokipii 1976; Armstrong et al. 1981). This turbulence is characterized by the 'The Big Power Law' spectrum of density fluctuations (Armstrong et al. 1995; Chepurnov and Lazarian 2010). Recent studies suggest that the turbulence observed in the VLISM is a superposition of the fluctuations emanated by the heliopause and the background LISM turbulence. However, discriminating between

these two components has been difficult so far, which leaves the question about the properties of the unperturbed LISM turbulence open. However, the IBEX ribbon is a unique observable for this situation. The ribbon has been shown by models to be sensitive to the turbulence in the LISM within a few hundred au of the heliopause, i.e., the power level of turbulence that may cause, e.g., 'weak' or 'strong' pitch angle scattering (Zirnstein et al. 2018a, 2019, 2023). Models of the ribbon (Zirnstein et al. 2020b) and theory (Zank et al. 2019) suggest that the turbulent component emanating from the heliopause is stronger than the pre-existing LISM turbulence, with a correlation scale on the order of ∼100 au, i.e., the size of the nose-ward heliosphere (Zank et al. 2019; Zirnstein et al. 2020b; Xu and Li 2022). Thus, with ever-improving models/theory of the ribbon, and better measurements of the ribbon characteristics (width, radius, center, etc.) from IMAP's ENA imagers, particularly IMAP-Hi whose energy range covers the energies at which the ribbon is observed, we can learn much more about turbulence in the VLISM. The source particles of the ribbon come from neutralized solar wind/PUI particles inside the heliosphere. The properties of the solar wind over time are an essential component to understand the ribbon and its evolution over time; thus, IMAP's in situ measurements are essential for predicting the source particles of the ribbon.

4 New Inner Heliospheric Science

One of the primary science objectives of the IMAP mission is to 'identify and advance understanding of particle injection and acceleration processes near the Sun, in the heliosphere and heliosheath' (McComas et al. 2018a, 2025b). IMAP brings unique capabilities to the HSO to improve our understanding of the acceleration and transport of energetic particles in the heliosphere and answer some of the key open questions of energetic particle phenomena, including (Desai and Giacalone 2016):

1. Where and how are these particles energized?
2. What is the source material or seed populations?
3. How do properties of the accelerated populations get modified during transit from remote acceleration sites to an observer's location?

4.1 Particle Acceleration

4.1.1 Injection Problem

The so-called 'injection problem' involves a seemingly paradoxical challenge of collisionless shock physics, in which particles incident on the shock require some energy significantly above the thermal plasma energy to enter into diffusive shock acceleration (DSA). A generally accepted lower limit of DSA is a few times greater than the energy of the plasma flow itself (Giacalone 2003b), which is greater than the plasma thermal energy by a factor of a few times the square of the shock Mach number. This problem continues to limit progress in our understanding of energetic particle seed populations, acceleration, and successful model development (Giacalone et al. 1994; Kallenbach et al. 2005; Zank et al. 2001). Theoretically, the injection problem exists because DSA is deemed unable to scatter particles with speeds similar to the local plasma speed and diffusively accelerate them. Shocks with an angle Θ_{Bn}—i.e., the angle between the upstream magnetic field vector and the direction of the shock normal vector propagation—that is less than 45° are referred to as quasi-parallel;

otherwise they are quasi-perpendicular. Considering electric fields, drift motion, and appropriate frames of reference, only particles that are sufficiently energetic or a pre-accelerated seed population can participate in the acceleration processes at collisionless shocks, where the injection energy threshold increases with the shock normal angle (Lee 1983; Jones and Ellison 1991; Zank et al. 2001). However, in typical heliospheric plasmas, a significant high-energy tail exists prior to encountering heliospheric shocks, so the seed population for DSA is typically already present. Some numerical studies have suggested that thermal protons can be efficiently injected and accelerated at quasi-perpendicular shocks (e.g., Giacalone 2003b, 2005). However, observational studies have revealed somewhat conflicting results. Indeed, solar wind protons have been observed to be accelerated by several CME-driven shocks, supporting the idea that the ambient solar wind could provide a seed population for shock acceleration (e.g., Baring et al. 1997; Lee 1983, 2005; Giacalone 2012; Giacalone et al. 2023; Parker et al. 2014). Other studies indicate that other populations are important constituents of the seed particles that are accelerated by DSA including the suprathermal tail of the solar wind, pre-accelerated populations of tracer ion species such as suprathermal ^{3}He ions from flares, heavier ions from small and large SEP events, and interstellar He PUIs (Gosling et al. 1981; Tan et al. 1989; Tsurutani and Lin 1985; Chotoo et al. 2000; Desai et al. 2001, 2003, 2006a; Kucharek et al. 2003; Allegrini et al. 2008).

For at least two reasons, PUI populations are considered a strong candidate for energetic particle seed populations: (1) they have higher speeds extending up to twice the local plasma speed and (2) they are pitch-angle scattered into a torus or shell-like distribution compared to the highly anisotropic, beam-like (in the shock frame) solar wind distribution (Giacalone and Jokipii 1997; Jokipii and Giacalone 1996; Le Roux et al. 2002). Likewise, pre-accelerated SEP populations also have two clear advantages: they are (1) nearly isotropic and (2) extend from ∼few keV up to MeV energies (Desai et al. 2006b; Dayeh et al. 2017; Alterman et al. 2023, 2024). In contrast, the core solar wind ion population has only one clear advantage: it has significantly higher number density and is thus likely to play a key role in dissipating the energy available at IP shocks, which results in heating the thermal plasma. Exactly how a given shock partitions its energy into heating and accelerating the solar wind plasma and re-accelerating the suprathermal seed populations remains unanswered, and likely depends on different ambient conditions under which the shock forms and propagates as well as properties of the shock itself (Zank et al. 2006; Li et al. 2009). Finally, depending on which acceleration mechanism dominates (i.e., first-order or second-order Fermi, shock-drift, shock surfing, or specular reflection), distinct 3D VDFs and spectral forms, as well as characteristic pitch-angle distributions, are expected to be observed downstream of the shock (Decker 1983; Armstrong et al. 1985; Starkey et al. 2019, 2021).

Very few observational studies have explored these issues either in individual cases (Ogasawara et al. 2025) or using a statistically significant event sample because to date only the Magnetospheric Multiscale (MMS) mission has provided high-time resolution 3D VDFs of ion species from different origins, such as solar wind He and PUI He (Cohen et al. 2019; Starkey et al. 2019). While MMS is not optimized to make routine measurements in the solar wind, IMAP instruments are designed to have (1) higher angular resolution, and (2) sufficient mass resolution to both separate flare-origin ^{3}He from the more abundant solar wind ^{4}He at the <10% level and identify heavier ion species up to Fe over a broad energy range from ∼0.5 keV to above ∼10 s of MeV/nuc. IMAP instruments also have adequate geometric factor and are sufficiently sensitive to provide 3D VDFs at <1-hr time resolution for PUI He and solar wind He, which enables IMAP to unambiguously identify the origin of the seed populations and characterize the ion 3D VDFs upstream and downstream of IP shocks. These measurements are central to understanding how ion species from different

sources with distinct spectral and/or angular characteristics are preferentially selected or injected into the acceleration processes (Gloeckler et al. 1994; Giacalone 2003b; Zank et al. 2001). Simultaneously, these measurements also enable IMAP to determine whether the dominant energization occurs parallel or perpendicular to the local magnetic field direction (e.g., Starkey et al. 2021), and thus identify the primary mechanisms by which IP shocks accelerate these different ion species and quantify the energy partition during individual cases.

4.1.2 Suprathermal Seed Particle Characteristics

Theoretical models of shock-driven particle acceleration reproduce many observed features of energy spectra and temporal evolution, yet significant discrepancies remain. Predicted spectral slopes often diverge from in situ measurements and particle intensities vary far more than models account for. Observations show that accelerated particles contain enhanced trace ions (e.g., ^{3}He, He$^+$) and heavy ion ratios that differ from the solar wind composition. These features correlate with the suprathermal ion population - highly variable in both abundance and composition – suggesting that suprathermals contribute to the seed population. A key to understanding the variability of SEP composition lies in characterizing this suprathermal population, which is believed to be substantially different and more variable than the bulk solar wind (e.g., Mewaldt et al. 2007; Desai and Giacalone 2016). However, measurements have been limited because suprathermals occupy an energy range that typically falls between the upper sensitivity of solar wind instruments and the lower threshold of traditional energetic particle detectors, many of which lack composition resolution. As shown in Fig. 13 (adapted from Dayeh et al. 2009; see also Mason and Gloeckler 2012), quiet-time abundance ratios such as C/O, Fe/O, and ^{3}He/^{4}He vary with the solar cycle, reflecting the dynamic and evolving nature of the suprathermal pool - an essential factor in explaining the wide range of observed SEP event characteristics. IMAP sensors fill in this measurement gap by making significant compositional observations from 0.5 keV/q to 5 MeV/nuc, with charge state and composition covered up to 80 keV/q and composition only from 80 keV/nuc to 5 MeV/nuc.

Charge-state measurements of the energetic particle population are also currently lacking. ACE/SEPICA was the last instrument to reliably and directly measure the energetic particle charge-states in the solar wind (Möbius et al. 1998). As transport and acceleration processes are generally dependent on the particles' magnetic rigidity (particle momentum divided by charge), the charge state is an important parameter. Most SEP analysis involves information about charge-to-mass ratios (Q/M), e.g., the dependence in the spectral break energies (e.g., Cohen et al. 2005; Mewaldt et al. 2005; Desai et al. 2016) or the compositional biases (e.g., Reames 2014). Current work generally assumes charge states based on previous limited measurements or isothermal temperature arguments, both of which are potentially inaccurate for any individual SEP event under study. IMAP measures the average charge state of C to Fe ions over the suprathermal to energetic particle range from several keV/nuc to a few MeV/nuc, allowing the appropriate values to be used on a case-by-case basis. These charge state measurements are also necessary to answer important questions on the origin of the suprathermal population (Dayeh et al. 2009, 2017; Alterman et al. 2023, 2024). Measurements of charge states in IP shocks and other solar wind structures also shed light on how particles with different Q/M are injected and accelerated to high energy (Desai et al. 2003; Allegrini et al. 2008) and whether that can explain why SEPs have significant event-to-event variation in different ion abundance ratios (e.g., ^{22}Ne/^{20}Ne, ^{26}Mg/^{24}Mg, and He/H) (Leske et al. 1999; Wiedenbeck et al. 2008; Cohen et al. 2021).

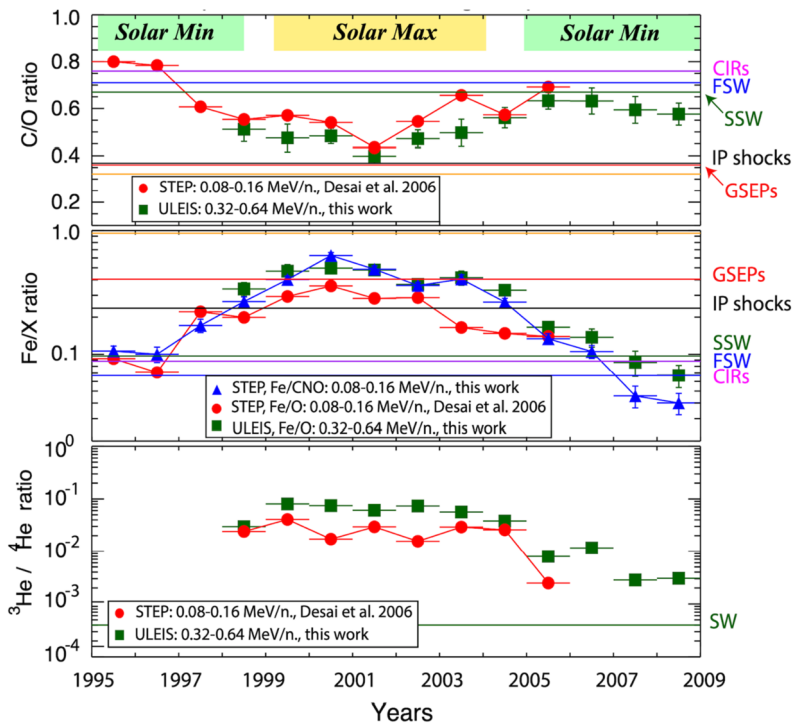**Fig. 13** Quiet-time average values of suprathermal ion ratios—C/O (top), Fe/O and Fe/CNO (middle), and ^{3}He/^{4}He (bottom)—illustrating their dependence on the solar cycle (from Mason and Gloeckler 2012, updated from Dayeh et al. 2009). Horizontal lines in each panel represent averaged abundances measured in: CIRs at ∼ 0.15 MeV/nuc (CIRs; Mason et al. 2008); gradual SEP events at ∼ 0.38 MeV/nuc (GSEPs; Desai et al. 2006b); CME-driven interplanetary shocks at ∼ 0.75 MeV/nuc (IP shocks; Desai et al. 2003); fast solar wind (FSW; Gloeckler and Geiss 2007); slow solar wind (SSW; von Steiger et al. 2000). The horizontal line in panel (c) shows the average SW value (Gloeckler and Geiss 1998)

Finally, accurate charge-state measurements are key to identifying Q/M-dependent transport effects that act on suprathermals (and SEPs). For example, the way in which suprathermals propagate to reach the shock acceleration region and SEPs escape it and fill regions of the heliosphere may be influenced by guiding center drifts due to the large-scale IMF (Dalla et al. 2013; Wijsen et al. 2020) and to local magnetic field structures. The guiding center drift velocity is proportional to Q/M so that partially ionized heavy ions experience drift effects to a different degree depending on their charge state and mass and this influences their spatial distribution in the heliosphere (Dalla et al. 2017). Measuring Q/M consistently in the ∼10 keV/nuc - 1 MeV/nuc range allows characterization of the energy dependence of charge states over this range and leads to a better understanding of its origin (Klecker et al. 2007; Dalla et al. 2017).

4.1.3 Foreshock Region Acceleration

The ability for an energetic particle to 'outrun' the shock in its own frame of reference depends strongly on the aforementioned shock Θ_{Bn} angle. For quasi-perpendicular shocks ($\Theta_{Bn} > 45°$), the amount of energy it takes for an ion to outrun the shock quickly approaches

infinity, resulting in a region upstream of the shock that is relatively free of reflected particles. However, for quasi-parallel shocks ($\Theta_{Bn} < 45°$), a single interaction with the shock ramp typically provides enough acceleration to some subset of the incident ions that they are able to reflect and return into the upstream creating an ion foreshock (see also Sect. 2.6). These foreshocks are extremely efficient accelerators of energetic particles through a number of different acceleration mechanisms that often act collectively and possibly even feedback on each other nonlinearly (e.g., Caprioli and Spitkovsky 2014; Wilson et al. 2016; Liu et al. 2018; Turner et al. 2018; Liu et al. 2019; Amano et al. 2020; Caprioli et al. 2020; Liu et al. 2020; Raptis et al. 2024). Such mechanisms include first- and second-order Fermi acceleration (Fermi 1949), shock-drift acceleration (e.g., Sonnerup 1969; Lee et al. 1996; Ball and Melrose 2001), betatron acceleration, and potentially quasilinear and nonlinear wave-particle interactions (e.g., Shi et al. 2023; Artemyev et al. 2022). As discussed in the previous section, all of these acceleration mechanisms are characteristically dependent on particle mass and charge state. As such, the IMAP observations offer excellent opportunities to characterize how solar and IP shocks accelerate SEPs and contribute to nonlinear dynamics within the ion foreshock. From its location at L1, IMAP will routinely observe both SEPs accelerated by shocks at lower heliocentric distances, right down into the solar corona, and directly in situ at interplanetary shocks. For the subset of interplanetary shocks that happen to be quasi-parallel at L1, IMAP will further be able to directly observe those shocks' foreshock regions in situ.

4.2 Energetic and Solar Wind Electrons

Energetic solar electrons are of key interest in their own right, but they also provide broad and deep insights into the locations of energy dissipation regions near the Sun. Once accelerated to mildly relativistic energies, solar electrons propagate rapidly along the IMF in ways that permit mapping of field topologies and also permit identification of coronal energization sites. The energy spectrum and pitch angle distributions of energetic solar electrons can provide considerable insight into mechanisms operating in both solar flares and at IP shock waves as they expand outward from solar disturbance sites.

Energetic solar electrons form the tail of the overall solar wind electron population. The bulk solar wind electrons are generally considered to be composed of three essential components as illustrated in Fig. 14 (Feldman et al. 1975, 1978; Rosenbauer et al. 1977; Anderson et al. 2012). The thermal 'core' electrons are the lowest-energy population and are considered to be trapped or confined within the solar system by an interplanetary potential barrier that exists between the Sun and the distant heliosphere. The higher energy suprathermal solar wind electrons consist of two components: a diffuse 'halo' population and an anisotropic 'strahl'. Halo electrons are higher in temperature than the thermal core, but have a lower number density. The halo population is isotropic with a VDF that is well-represented by a bi-Kappa distribution as shown in Fig. 14. Strahl electrons are a narrow field-aligned population that stream rapidly outward from the hot solar corona and form a highly directional distribution along the IMF near 1 au and throughout the inner heliosphere. The strahl electrons comprise the heat flux component carried within the solar wind. In addition, a 'superhalo' population has been observed at higher energies (Lin et al. 1997; Livadiotis 2017).

Solar energetic electrons are generally considered to be the more highly accelerated population of the overall electron distribution and extend from tens of keV to MeV energies. It is widely accepted that solar energetic electron events are among the most prevalent particle acceleration phenomena detectable in interplanetary space (Lin 1985). Such energetic electron events near 1 au can last for as little as a few tens of minutes, but can also last up to a
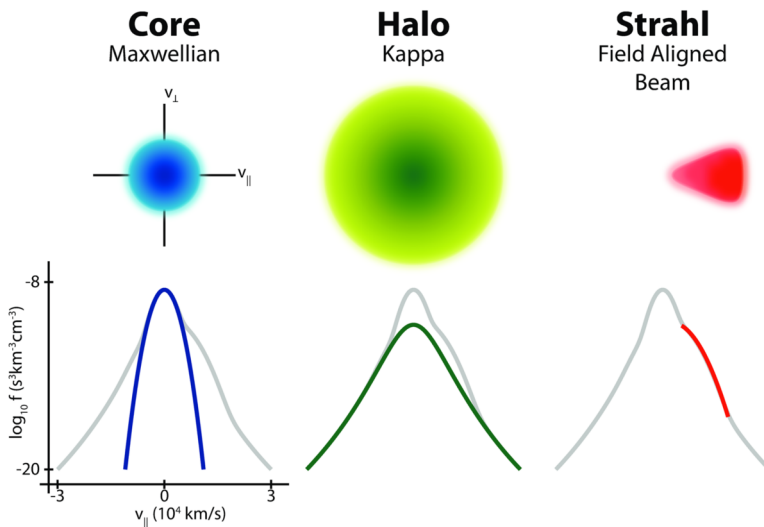
Fig. 14 Solar wind electron pitch-angle distributions (top) and parallel VDF (bottom). Top images show that core and halo populations have isotropic bi-Maxwellian and bi-Kappa distributions while the strahl is aligned with the magnetic field. Bottom images show how each population contributes to the overall field-aligned VDF (total shown in gray and individual components shown as colored lines). Courtesy M. Pulupa

few days. Near periods of peak sunspot activity, studies show that more than 150 events can occur each year (Wang et al. 2012). Solar electron bursts, many associated with Type-III radio bursts, are also observed at lower energies, down to 100 s of eV (Lin et al. 1996; Gosling et al. 2003, 2004a,b; de Koning et al. 2006, 2007), not always in association with the higher energy particles.

Because of their high speeds, energetic solar electrons constitute excellent probes of magnetic flux tube topologies in IP space. As such, energetic electrons can delineate times when magnetic flux tubes are directly connected back to acceleration sites in the solar corona (e.g. Mazur et al. 2000; Gosling et al. 2004a). Furthermore, bidirectional heat flux electron distributions can be used to identify 'magnetic cloud' or 'magnetic bottle' configurations in IP space (Gosling 1983). Counterstreaming electrons can also result from IMF connection to Earth's bow shock (Feldman et al. 1982); from connection to IP shocks or CIRs (Gosling et al. 1993; Steinberg et al. 2005); or from depletion of halo particles around 90° pitch angle (Gosling et al. 2001, 2002; Skoug et al. 2006). The absence of a strahl population has been used to indicate magnetic disconnection from the Sun in reconnection exhausts observed at the heliospheric current sheet (Gosling et al. 2005).

Hot solar wind electrons and solar energetic electrons also play a key role in Earth's magnetospheric processes. Such solar electrons become the 'seed population' that enters the terrestrial magnetotail and distant plasma sheet (Baker et al. 1985, 1998). These relatively energetic electrons are subsequently transported from the magnetotail toward the inner magnetosphere, where they are then accelerated to hundreds or even thousands of keV energies by large scale convection, inductive substorm electric fields (Baker et al. 1979), and localized acceleration mechanisms within the magnetotail and inner magnetosphere (Reeves et al. 2013; Thorne et al. 2013). These accelerated particles ultimately form the central components of the Van Allen radiation belts (Baker et al. 2019, 2021).

Additionally, the field-aligned strahl electrons and solar energetic electrons (when present in the IP medium) also propagate along magnetic field lines that interconnect with

the 'open' polar cap field lines extending into Earth's magnetotail lobes (Fennell et al. 1975; Baker et al. 1986). This population of solar electrons then actually forms what is called the 'polar rain' (Gussenhoven et al. 1984) observed by low-Earth orbit (LEO) spacecraft. This polar rain clearly delineates the large-scale connectivity of the IMF with Earth's magnetospheric fields (Gosling et al. 1986; Baker et al. 1987).

From its location at L1, IMAP provides 3D VDFs of the solar wind electron population (2 eV – 5 keV) to measure structures and transients in the solar wind. IMAP also provides measurements of near-relativistic (>270 keV) electrons propagating from and towards the Sun in several energy bands. As near-relativistic electrons travel significantly faster than SEP ions, the real-time electron data provided by IMAP is a key early warning for SEP events (e.g., Posner 2007; Lee et al. 2025).

4.3 The Expanded L1 Fleet and Coordinated Multi-Spacecraft Studies

The collection of spacecraft at 1 au carrying in situ instrumentation to measure plasma and magnetic fields may be described as the 'L1 fleet'. Taken together, the availability of simultaneous data from this array of spacecraft opens numerous new possibilities for synergistic multi-spacecraft studies of the upstream solar wind and IMF in relative proximity to Earth's orbit that have not been possible previously. The existing L1 fleet consists of NASA's Wind and Advanced Composition Explorer (ACE) spacecraft, the ESA Solar and Heliospheric Observatory (SOHO) spacecraft, NOAA's Deep Space Climate Observatory (DSCOVR) spacecraft, and ISRO's Aditya-L1 spacecraft. The addition of NOAA's Space Weather Follow On-Lagrange 1 (SWFO) spacecraft in 2025, launched with IMAP, provides added capacity to the constellation. The presence of IMAP dramatically increases this capability with complementary measurements to those of the other L1 spacecraft, thereby enabling valuable studies pertaining to both space weather and heliophysics. Altogether, the seven spacecraft in the L1 fleet ranges in separation from ∼10 Earth radii (R_E) to ∼200 R_E (∼6.4 × 10^4 km to 1.3 × 10^6 km; see Fig. 15). With spacecraft separated at a variety of scales, the L1 fleet enables unprecedented opportunities to study the mesoscale structure (Fig. 16) and spatiotemporal evolution of the solar wind near 1 au, enabling new understanding of solar wind structure and turbulence (e.g., Borovsky 2008) and potentially better predictive capabilities for space weather (see Sect. 4.4). Table 1 in Appendix 5 shows a comparison of the measurement capabilities of the spacecraft in the L1 Fleet, demonstrating the powerful complementary measurements that can be made with these missions.

4.3.1 Mesoscale Solar Wind Structure

Recent multi-spacecraft magnetospheric missions such as Cluster and MMS set the standard for extraction of spatial information, as distinct from temporal information, and for computing quantities related to spatial derivatives, as in the curlometer technique. This information is of exceptional value, and, for gradients in particular, the methods actually benefit from the small inter-spacecraft separations of those missions. Cluster and MMS orbits typically afford spacecraft separations in the range from 10 km up to 10,000 km. For information at larger scales, the familiar approach is to employ the single-spacecraft Taylor (i.e., frozen-in) hypothesis. This is widely used and while it remains useful, it mixes space and time variations and is best understood when the time variations due to local dynamics can be neglected entirely. Previous studies of spatial structure on multi-spacecraft analysis without applying the Taylor hypothesis have necessarily resorted to comparing spacecraft data streams from pairs of spacecraft with separations in a larger range of interest. Such an approach, for example, using ensembles of paired datasets from Wind and ACE (Matthaeus et al. 2005) enabled
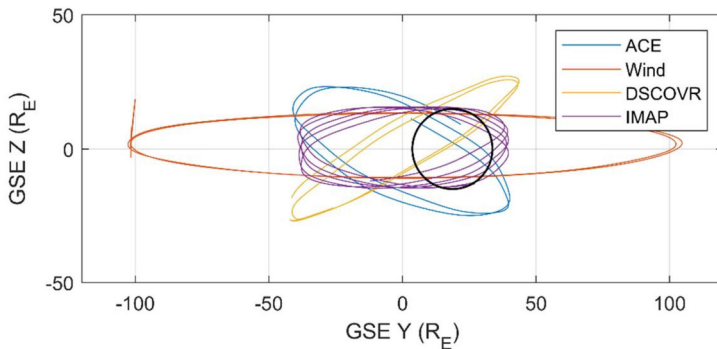
Fig. 15 2D projection of the orbits of several spacecraft of the L1 Fleet in units of Earth radii showing the wide range of mesoscale structures that can be probed by these spacecraft. The black circle indicates the projected, aberrated cross section of the magnetopause at X_GSE = 0; aberration assumes Earth's orbital motion, 30 km/s in the ecliptic perpendicular to the Earth-Sun radial direction, and a nominal solar wind speed of ~ 400 km/s along that radial direction

the correlation length of interplanetary turbulence to be directly measured for the first time without assumptions such as the Tayor hypothesis. However, this can only be accomplished if adequate data are available with separators on the order of 500,000 to 1,000,000 km. With only two available spacecraft, and in the absence of planned orbit separations, such a study requires use of data from varying time frames, perhaps separated by months or even years. This introduces other parameters to be controlled, such as solar wind speed, proximity to the heliospheric current sheet, solar cycle, and the presence of CMEs. With the IMAP mission increasing the number of operative spacecraft, the L1 fleet becomes much more valuable and capable of evaluating targeted information more rapidly and less confounded by varying parameters. It also becomes more sensitive to correlation anisotropy and more capable of separating space and time correlations (Matthaeus et al. 2016). Another major advantage of such multi-spacecraft analysis with three or more spacecraft is that the larger number of baselines and their different orientations enables simultaneous investigation in various directions. This clearly increases the rate at which measures of directional anisotropy can be evaluated. As the number of available simultaneous spacecraft data streams becomes larger, the number of useful baselines increases dramatically, i.e., with six spacecraft in the L1 fleet, the number of potentially useful baselines increases to 18.

Similar multi-spacecraft methods can be implemented by the IMAP-enhanced L1 fleet to study other turbulence topics as well, such as $1/f$ noise, cascade rates at large scales, space time-correlation at the outer scale, etc. In general, when turbulence properties are measured at scales larger than the correlation scale, the data quantify the state and dynamics of 'energy-containing scales' of classical turbulence (Batchelor 1970). For freely decaying turbulence these eddies exert control of the cascade dynamics at all smaller scales, including the entire inertial range where 'Kolmogorov-like 'power-law spectra are typically observed. Simply put, the enhanced L1 fleet measures the input to the turbulence cascade. It is noteworthy that the upcoming nine-spacecraft NASA HelioSwarm mission will probe much smaller inertial range scales, from around 1000 km to the ion inertial scale near 100 km where dissipation processes set in. Thus, the expanded L1 fleet will provide input to the dynamics observed by HelioSwarm as solar wind structures propagate from L1 to the HelioSwarm orbit near the Earth.
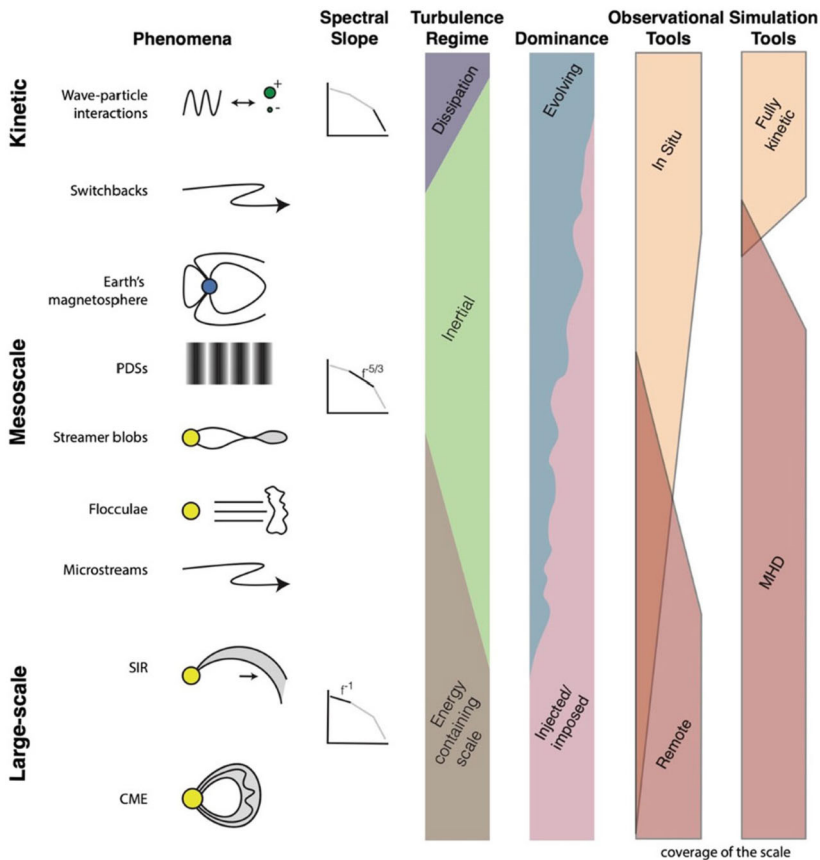
Fig. 16 Spatial scale of solar wind structures (from Viall et al. 2021). The L1 fleet will allow unprecedented study of a variety of mesoscale structures and phenomena. The kinetic scale represents phenomena less than an ion inertial length (10's of km) through 100's of km. The mesoscale spans 100's of km to ∼ 10,000 Mm after which structures are considered large-scale. See Viall et al. 2021 for detailed descriptions

4.3.2 Shock Structure & Morphology

IP shocks move through, and interact with, a turbulent solar wind plasma, and, as such, their surfaces are distorted, or rippled. With numerous spacecraft in close proximity at L1 the structure of shock fronts can be studied in relatively-good detail; of particular interest is the scale of surface ripples. Neugebauer and Giacalone (2005) used the crossing times of 26 transient IP shocks seen by seven different spacecraft near Earth to infer an average radius shock surface curvature of the order of 3 million km. This study involved spacecraft that were separated by rather large distances, but also included some smaller separations. The array of spacecraft in orbits at L1, covering a somewhat smaller spatial range as well as some larger separations of the order of the turbulence coherence scale, can be used to considerably advance our understanding of shock surface structure (Szabo et al. 2001; Szabo 2005). Notably, limited information on IP shock structure has inhibited understanding of how such variations may impact the geoeffectiveness of these shocks in driving a response in Earth's magnetosphere.

In addition to the rippling of shock surfaces, the interaction of IP shocks with pre-existing solar wind turbulence also leads to other important effects. For instance, spacecraft which are separated far enough apart often observe different behavior in the bulk plasma, field, and energetic particle parameters as functions of time. Neugebauer et al. (2006) showed that energetic particle fluxes were reasonably correlated when the spacecraft separation was less than about 3 million km. The variation of the plasma properties seen by different spacecraft across the same shock is less well studied, and the addition of IMAP to the L1 fleet of spacecraft considerably advances our understanding of the structure of shocks.

The study of energetic particles and plasma across individual shocks seen by multiple spacecraft also provides a critical test to the theory of DSA. A fundamental result from this theory is that the distribution function of energetic particles accelerated by the shock have a power law dependence on momentum (or energy) over a range of energies from a keV up to a few MeV. The theory predicts that the power-law index depends only on the density jump across the shock. However, because shocks move through turbulence, the locally observed density jump across the shock likely depends on where along the shock front that the observer is located. This was discussed by Giacalone and Neugebauer (2008), who showed that spacecraft separated by scales of the order of the turbulence coherence scale will see different local density jumps. The energetic particles, however, are considerably more mobile owing to their large speeds, averaging over the fluctuations. Thus, their spectra are likely similar at different places along the shock front. Giacalone and Neugebauer showed that the energy spectra of energetic particles seen to be associated with three separate IP shocks seen by two spacecraft were similar, which supports this idea. With many spacecraft observing the density jump across a single shock, an average density jump can be estimated. The test of DSA theory is then whether the observed spectral index of energetic particles at low energies (below any spectral break energy) is well correlated with the average density jump.

4.4 Space Weather-Related Science

4.4.1 Scientific Understanding

One of the most important advancements in observational capability for space weather research came about in the 1978-80 timeframe with the insertion of the ISEE-3 spacecraft into a 'halo' orbit around L1 (Tsurutani and Baker 1979). At the key L1 location upstream of Earth in the supersonic, super-Alfvénic solar wind flow, it proved possible to monitor in an uninterrupted way the solar wind speed and density along with the IMF strength and orientation. These 'driver' characteristics of the solar wind flow were seen through numerous empirical studies to be highly correlated with all manner of geomagnetic activity such as geomagnetic storms and magnetospheric substorms (Baker et al. 1981, 1983 and references therein).

In IP space, the energetic particle propagation is highly dependent on the solar wind and embedded transient structures. The nominal IMF 'guides' charged particle transport making them stream along the IMF lines. The IMF and the solar wind fluctuate resulting in particle scattering and cross-field diffusion (Reid and Kontar 2010; Klein and Dalla 2017); for example, energetic particle transport is affected by IP turbulence (Jokipii 1966; Chhiber et al. 2019). Large-scale structures like CMEs and IP shocks can accelerate SEPs to relatively high energies (Desai and Giacalone 2016) and induce geomagnetic storms as well as Forbush decreases (Ghag et al. 2023). At lower energies, IP strahl properties are correlated with magnetic discontinuities (Borovsky 2020). Rosenvinge et al. (2009) showed that energetic particle data exhibit intensity variations that suggested a linkage to mesoscale flux tubes.

The Earth's Van Allen radiation belts are populated by energetic protons and electrons trapped in the geomagnetic field, respectively in the inner and outer belts, with the outer belt trapped electron intensities being highly dynamic varying over several orders of magnitude over time scales ranging from minutes to years (Baker and Kanekal 2008). Electron dynamics are driven ultimately by transient/recurrent structures in the solar wind (Kanekal 2006; Baker and Kanekal 2008). Radiation belt electrons also respond to mesoscale transient structures in the solar wind, such as periodic density structures (PDS) (Kepko and Viall 2019; Di Matteo et al. 2022). A recent study by Kurien et al. (2024) provides the first evidence that mesoscale structures, in the form of PDSs, modulate relativistic and ultra-relativistic electron intensities in the heart of the outer radiation belt ($L \approx 4$). The electron modulation was found to occur at frequencies close to those of IP PDSs, exhibiting intensity modulations over a wide range of energies ($\sim$200 keV to 4 MeV) and pitch angles ($\sim$20-120°). Energetic particles are also known to pose a significant space weather hazard to human assets in space, as well as affect global climate by inducing changes in atmospheric chemistry through particle precipitation (Baker et al. 2018).

It is important to recognize that space weather effects in the terrestrial magnetosphere-ionosphere system are driven in clear and direct ways by changes in the mesoscale properties of solar wind plasmas that flow from the Sun (Baker 1996, and refs. therein). By measuring north-south IMF orientation changes or major shifts in solar wind speed as they are about to impact Earth, one can develop highly effective space weather forecasting methods (Baker et al. 1981, 1983).

4.4.2 Real-Time Space Weather Capability

As described in Tsurutani and Baker (1979), the key to effective utilization of L1 solar wind monitors is to have real-time measurements of solar wind/IMF properties that could then be telemetered continuously to ground receiving stations. Under typical solar wind conditions, alerts and warnings for relevant changes in solar wind driving conditions could be achieved with 45-minute to 1-hour warning times. Under extreme driving conditions, these warning times were often reduced to less than 30 minutes. Through early and dedicated collective efforts of NASA, NOAA, and other agencies, the ISEE-3 monitoring system was emplaced by the NOAA Space Environmental Services Center (now the Space Weather Prediction Center) by March 1980 (Jocelyn 1980). The ISEE-3 real-time alert system proved so beneficial and so important that this approach was replicated with the ACE spacecraft (Acuña et al. 1995) that is still operational today after nearly three decades of operational utilization; similar real-time space weather data links were also provided by NASA's STEREO and Van Allen Probes missions. IMAP continues, and greatly extends, this remarkable and highly effective monitoring tradition through the IMAP Active Link for Real-Time (I-ALiRT) capability, which provides low-latency, near-real-time in situ measurements of relevance to space weather forecasting (see McComas et al. 2025b; Lee et al. 2025).

Space weather is a matter of growing importance as humanity becomes increasingly reliant on infrastructure that can be affected by the space environment. As we move towards an expansion in human spaceflight, including upcoming missions to send humans back to the Moon and for the first time to Mars, the ability to forecast space weather events is an important facet of the health and safety of astronauts and the protection of space assets. For these reasons, space weather has been elevated as a national priority through the National Space Weather Action Plan and the PROSWIFT Act, passed by Congress and signed into law in 2020.

Data from scientific and operational instruments are utilized by a variety of government sponsors (including those with both civil space and national security interests), commercial

companies, and research groups for the purposes of forecasting, nowcasting and hindcasting space weather events. As such, the availability of reliable real-time space weather data is of fundamental importance to understanding and utilizing the predictors of space weather events. The diversity of these data in terms of both data products and heliographic position contributes to our ability to model and predict these events.

With I-ALiRT, IMAP joins ACE, STEREO, and DSCOVR, in making continuous real-time space weather observations from orbit. IMAP, ACE, and DSCOVR are all located at L1 but provide varied and complementary measurement capabilities. STEREO expands on these capabilities by monitoring space weather along 1 au from other longitudes due to its unique heliocentric orbit. Additional capabilities are offered by the GOES satellites as well as SWFO-L1 and the anticipated ESA Vigil mission to be located at L5.

5 Summary

The IMAP observatory provides our most comprehensive, full system-of-systems view of our heliosphere and its interaction with the LISM. The mission is a unique combination of in situ and remote sensing instruments that enables studies of the heliosphere through interconnected local and distant observations at a level not previously possible. As discussed above, many aspects of fundamental particle acceleration and transport found throughout the heliosphere benefit from this new capability. Connecting conditions observed by IMAP at 1 au to variations in the outer heliosphere and the resulting impact on the energization of particles is a primary focus of IMAP science. This involves characterizing the PUI population and the suprathermal ions at 1 au with SWAPI and CoDICE and their evolution across IP shocks (measured by SWAPI and MAG), some of which are expected to be reasonable analogs to the termination shock. How energetic and suprathermal particles observed by CoDICE and HIT modify shocks at IMAP's location also provides critical information regarding particle interactions with the termination shock.

Examinations of the variations in the heliosphere and their impact on the structure of its boundary and interactions with the ISM yields a new understanding of the dynamics of the greater system. IMAP characterizes the latitudinal structure of the solar wind with GLOWS and, in combination with missions beyond 1 au, can speak to the radial evolution as well. How solar wind structures evolve with distance and impact the outer boundaries of the heliosphere to change the ENA production is an important study that involves both the in situ and remote sensing instruments on IMAP. Similarly, the creation of the ACRs and their modulation as they diffuse back to be measured by HIT is examined in the context of the time evolution of the solar wind structures propagating outward.

Naturally, IMAP also addresses inner heliosphere science from its L1 vantage point and contributes to the HSO. With IMAP's advanced in situ instrumentation, detailed investigations into the characteristics of the suprathermal population needed to fully understand the injection and energization of particles can be conducted. New charge state measurements from CoDICE are instrumental in characterizing the Q/M-dependent effects of SEP acceleration and transport and provide critical clues for resolving the source of the seed population accelerated at a variety of solar wind structures. IMAP joins a number of existing spacecraft near L1 creating the ability to study the meso-scale structure of the solar wind and shock morphology, while also providing a bridge between older solar wind and SEP data sets and the new ones IMAP creates. Detailed observations from SWE and SWAPI of the VDFs of ions and electrons, along with magnetic field measurements from MAG, also characterize the solar wind impinging on the Earth's magnetosphere. Finally, the enhanced real-time data

produced by IMAP improves space weather forecasting and alerts that are needed to protect space-based assets.

Appendix: L1 Fleet Capabilities

As discussed above, the L1 Fleet has varied instrument suites capable of measuring a wide variety of observables. This includes important capabilities that are common among many of the spacecraft (e.g., 3D velocity distribution functions of the solar wind) and capabilities that are unique to individual spacecraft (e.g., IMAP interplanetary and interstellar dust measurements). Together, these complementary instrument suites have the ability to facilitate previously impossible scientific studies. In Table 1, we provide a comparison of the capabilities for the spacecraft in the L1 fleet.

Table 1 Comparison of the measurement capabilities of the various spacecraft in the L1 fleet, with a special focus on the capabilities introduced by IMAP

Measurement	Spacecraft (Instrument)					
	IMAP	IBEX	ACE	SWFO	WIND	Aditya
Magnetic field	**MAG:** 2-64 vectors/s 12s 128 Hz	—	6 vectors/s, 64 s	8 vectors/s, 64 s 300s latency8Hz	11 vectors/s	24 vectors/s
ISN atoms (H, He, O, Ne, and D) tracked over >180o in ecliptic longitude	**IMAP-Lo/Hi/Ultra:** 9°/4°/2°-10° angular res. 6-month map 3-month res. (1 week Ultra)	**IBEX-Lo/Hi:** 6.5o × 6.5o or 3.2o × 3.2o FOVGE: ~8-30x10^{-4} (cm^2 sr eV/eV)6-month map	—	—	—	—
Energy resolved global maps of ENA H and O.	**IMAP-Lo:** 5-1000 eV **IMAP-Hi:** 0.41-15.6 keV **IMAP-Ultra:** 3-300 keV (H) up to 300 keV/q	**IBEX-Lo:** 10 eV-2 keV $\Delta E/E$ = 0.8 **IBEX-Hi:** 300 eV-6 keV $\Delta E/E$=0.47-0.66	—	—	—	—
3D distribution of SW thermal and suprathermal electrons	**SWE:** 1 eV to 5 keV 12% en. res. 12o × 21o ang. res. 15s time res.	—	**SWEPAM-E:** 1.6-1350 eV 12% en. res. 9-28o × 21o ang. res. 64s time res.	**STIS:** 25-250 keV 80°x 60°FOV16s time res.	**SWE/VEIS:** 7 eV-24.8 keV 7.5°x 6.5°FOV92s time res. **3DP/SST:** 25-1000 keV 22.5°x36° angular res. $\Delta E/E$=0.3 **3DP/EESA Low:** ~0.003-1 keV **3DP/EESA High:** 0.200 - 30 keV $\Delta E/E$=0.2	**PAPA/SWEEP:** 0.01-3 keV

Table 1 *(Continued)*

Measurement	Spacecraft (Instrument)					
	IMAP	IBEX	ACE	SWFO	WIND	Aditya
solar wind H+ and He++ and interstellar He+ and H+ PUIs	**SWAPI:** 0.1–20 keV/q8.5% en. res. 12 s time res. GE (cm² sr eV/eV) Sun-viewing: 2.57×10^{-7} for SW H+ (cold plasma with 8° FWHM beam) Non-Sun-viewing: 1.6×10^{-2} for PUI He+ (hot plasma approx..)	—	**SWEPAM-I:** 260 eV–35 keV 5% en. res. 9-28o × 21o ang. res. 64s time res. GE: 2-7 10^{-4} (cm² sr eV/eV)/pixel	**STIS:** 5-6000 keV 80°x 60°FOV16 s time res. **SWiPS:** 0.17 to 33 keV/q60 s res.	**SMS/SWICS:** 0.5 to 30 keV/qΔ(E/q)/ (E/q)=6%4o × 45o FOVGF (cm² sr): 2.3 $\times 10^{-3}$ **SWE:** ~150 eV -8 keV Faraday Cup 7 eV to 24.8 keV VEIS	**ASPEX/SWIS:** 100 eV to 20 keV ΔE/E ≈10%180° FOV 22.5° ang. res.
The 3D VDFs ionic charge state and mass composition	**CODICE-lo:** ~ 0.5–80 keV/qM range: 3-60 amu M/ΔM=2- 10(M/q)/Δ(M/q) < 25GE:1.4 x10^{-3} (cm² sr eV/eV)	—	**SWICS:** 0.16 to 15.05 keV/q 5.2% en. res. 0.49–100.0 keV/q 6.4% en. res.	—	**APE-A/B:** ~ 0.2-10 MeV GF: 1.2 cm² sr **SMS/STICS:** 8-226 keV/qΔ(E/q)/ (E/q)=5%Δ(M/q)/ (M/q)=15%4.5o × 156o FOVGF(cm² sr): 0.05 **SMS/MASS:** 0.5 to 12 keV/qM/ΔM > 100Δ(E/q)/ (E/q)=5% **3DP/PESA Low:** 0.1-10 keV GE: 1.6 × 10^{-4} cm²-sr eV/eV 180°x14° FOV **3DP/PESA High:** GE 1.5 × 10^{-2} E cm²-sr ΔE/E=0.2	**PAPA/SWICAR:** 1-60 amu 0.01–25 keV/q

Table 1 (*Continued*)

Measurement	Spacecraft (Instrument)					
	IMAP	IBEX	ACE	SWFO	WIND	Aditya
Mass composition and arrival direction of heavy ions	**CODICE-Hi:** 0.03–5 MeV/nuc M range: 1-60 amu M/ΔM=7H, He,e-1 min res. C-Fe 15 min res. GF: 0.2 cm² sr **HIT:** 2 - 40 MeV/nuc 30o × 30o, all skyM/ΔM > 7GF: 4 cm² sr1 min res.	—	**SWIMS:** 3-60 amu M/ΔM > 100	—	**APE-A/B:** ~ 4.6-500 MeV/nuc GF: 1.2-1.3 cm² sr **IT:** ~ 3.4-230 MeV/nuc GF: ~9 cm² sr **LEMT:** ~ 1.4-50 MeV/nuc ~ 2% charge res. GF: 3 cm² sr **STEP:** ~ 0.02-8.1 MeV/nuc GF: 1.2-1.3 cm² sr **3DP/SST:** 0.02-11 MeV 22.5°x36° ang. res. ΔE/E=0.3	**ASPEX/STEPS** 20 keV/n to 20 MeV/n.
UV glow measurements for ionization rates, radiation pressure, and latitudinal SW	**GLOWS:** <5% accuracy on amplitude variations<15° accuracy on resolving latitude variations 20o × 360o,6-month sky map	—	—	—	—	**SUIT:** 200-400 nm focus on the Sun corona and spots
interstellar dust populations	**IDEX:** 1-500 amu M/ΔM > 2 dust M/ΔM > 200 ions Lyman alpha (124.567 nm) and He ray 58.4 nmFOV 50o	—	—	—	—	—

Declarations

Competing Interests C.M.S.C acknowledges membership on the Space Science Reviews editorial board. The other authors have no conflicts of interest to declare that are relevant to the content of this article.

References

Acuña MH, Ogilvie KW, Baker DN, et al (1995) The global geospace science program and its investigations. Space Sci Rev 71(1–4):5–21. https://doi.org/10.1007/BF00751323

Adhikari L, Zank GP, Hunana P, et al (2017) II. Transport of nearly incom- pressible magnetohydrodynamic turbulence from 1 to 75 au. Astrophys J 841(2):85. https://doi.org/10.3847/1538-4357/aa6f5d

Allegrini F, Schwadron NA, McComas DJ, Gloeckler G, Geiss J (2005) Stability of the inner source pickup ions over the solar cycle. J Geophys Res 110:A05105. https://doi.org/10.1029/2004JA010847

Allegrini F, Desai MI, Mason GM, et al (2008) Evidence for mass-per-charge–dependent acceleration of a multiple-component seed population by CME-driven interplanetary shocks near 1 AU. Astrophys J 682(1):690–696. https://doi.org/10.1086/587163

Alterman BL, Desai MI, Dayeh MA, et al (2023) Solar Cycle Variation of 0.3-1.29 MeV Nucleon^{-1} Heavy Ion Composition During Quiet Times Near 1 au in Solar Cycles 23 and 24. Astrophys J 952(1). https://doi.org/10.3847/1538-4357/acd24a

Alterman BL, Desai MI, Dayeh MA, et al (2024) Quiet-time spectra of suprathermal heavy ions near 1 au in solar cycles 23 and 24. Astrophys J Lett 964:L31. https://doi.org/10.3847/2041-8213/ad2deb

Amano T, Katou T, Kitamura N, et al (2020) Observational evidence for stochastic shock drift acceleration of electrons at the Earth's bow shock. Phys Rev Lett 124:065101. https://doi.org/10.1103/PhysRevLett.124.065101

Anderson BR, Skoug RM, Steinberg JT, McComas DJ (2012) Variability of the Solar Wind Suprathermal Electron Strahl. J Geophys Res 117(A4). https://doi.org/10.1029/2011JA017269

Armstrong JW, Cordes J, Rickett B (1981) Density power spectrum in the local interstellar medium. Nature 291:561–564. https://doi.org/10.1038/291561a0

Armstrong TP, Pesses ME, Decker RB (1985) Shock drift acceleration. Geophys Monogr 35:271–285. https://doi.org/10.1029/GM035p0271

Armstrong JW, Rickett BJ, Spangler SR (1995) Electron density power spectrum in the local interstellar medium. Astrophys J 443(1):209–221. https://doi.org/10.1086/175515

Artemyev A, Shi X, Liu TZ, et al (2022) Electron resonant interaction with whistler waves around fore-shock transients and the bow shock behind the terminator. J Geophys Res 127. https://doi.org/10.1029/2021JA029820

Axford WI, Leer E, Skadron G (1977) In: Proc. 15th Int. Cosmic Ray Conf. Plovdiv, vol 11, p 132

Baker DN (1996) Solar wind–magnetosphere drivers of space weather. J Atmos Terr Phys 58(14):1509–1526. https://doi.org/10.1016/0021-9169(96)00006-2

Baker DN, Kanekal SG (2008) Solar cycle changes, geomagnetic variations, and energetic particle properties in the inner magnetosphere. J Atmos Sol-Terr Phys 70(2–4):195–206. https://doi.org/10.1016/j.jastp.2007.08.031

Baker DN, Belian RD, Higbie PR, Hones EW Jr (1979) High-energy magnetospheric protons and their dependence on geomagnetic and interplanetary conditions. J Geophys Res Space Phys 84(12):7138–7154. https://doi.org/10.1029/JA084iA12p07138

Baker DN, Hones EW Jr, Payne JB, Feldman WC (1981) A high time resolution study of interplanetary parameter correlations with AE. Geophys Res Lett 8:179–182. https://doi.org/10.1029/GL008i002p00179

Baker DN, Zwickl RD, Bame SJ, et al (1983) An ISEE 3 high time resolution study of interplanetary parameter correlations with magnetospheric activity. J Geophys Res 88(A8):6230–6242. https://doi.org/10.1029/JA088iA08p06230

Baker DN, Fritz TA, McPherron RL, et al (1985) Magnetotail energy storage and release during the CDAW-6 substorm analysis intervals. J Geophys Res Space Phys 90(2):1205–1216. https://doi.org/10.1029/JA090iA02p01205

Baker DN, Bame SJ, Feldman WC, et al (1986) Strong electron bidirectional anisotropies in the distant tail: ISEE-3 observations of polar rain. J Geophys Res Space Phys 91(A5):5637–5662. https://doi.org/10.1029/JA091iA05p05637

Baker DN, Bame SJ, Gosling JT, Gussenhoven MS (1987) Observations of polar rain at low and high altitudes. J Geophys Res Space Phys 92(A12):13547–13560. https://doi.org/10.1029/JA092iA12p13547

Baker DN, Pulkkinen TI, Li X, et al (1998) Coronal mass ejections, magnetic clouds, and relativistic magnetospheric electron events: ISTP. J Geophys Res Space Phys 103(A8):17279–17291. https://doi.org/10.1029/97JA03329

Baker DN, Erickson PJ, Fennell JF, et al (2018) Space weather effects in the Earth's radiation belts. Space Sci Rev 214:17. https://doi.org/10.1007/s11214-017-0452-7

Baker DN, Hoxie V, Zhao H, et al (2019) Multi-year measurements of radiation belt electrons: acceleration, transport, and loss. J Geophys Res Space Phys 124(4):2588–2602. https://doi.org/10.1029/2018JA026259

Baker DN, Kanekal S, Hoxie V, et al (2021) Relativistic Electron-Proton Telescope (REPT) investigation: design, operational properties, and science highlights. Space Sci Rev 217:68. https://doi.org/10.1007/s11214-021-00838-3

Ball L, Melrose DB (2001) Shock drift acceleration of electrons. Publ Astron Soc Aust 18. https://doi.org/10.1071/AS01047

Bame SJ, McComas DJ, Barraclough BL, Phillips JL, Sofaly KJ, Chavez JC, Goldstein BE, Sakurai RK (1992) The Ulysses solar wind plasma experiment. Astron Astrophys Suppl Ser 92:237–265. https://ui.adsabs.harvard.edu/abs/1992A%26AS...92..237B/abstract

Baring MG, Ogilvie KW, Ellison DC, Forsyth RJ (1997) Acceleration of solar wind ions by nearby interplanetary shocks: comparison of Monte Carlo simulations with Ulysses observations. Astrophys J 476:889. https://doi.org/10.1086/303645

Batchelor GK (1970) The theory of homogeneous turbulence. Cambridge University Press, Cambridge

Bell AR (1978) The acceleration of cosmic rays in shock fronts – II. Mon Not R Astron Soc 182:443. https://doi.org/10.1093/mnras/182.3.443

Bera RK, Fraternale F, Pogorelov NV, Roytershteyn V, Gedalin M, Zank GP (2025) The role of pickup ions in the interaction of the solar wind with the local interstellar medium. II. Effects of solar cycle. Astrophys J 990:5. https://doi.org/10.3847/1538-4357/adec86

Bertaux JL, Kyrölä E, Quémerais E, et al (1995) SWAN: a study of solar wind anisotropies on SOHO with Lyman-alpha sky mapping. Sol Phys 162:403–439. https://doi.org/10.1007/BF00733435

Blandford RD, Ostriker JP (1978) Particle acceleration by astrophysical shocks. Astrophys J 221:L29. https://doi.org/10.1086/182658

Borovsky JE (2008) Flux tube texture of the solar wind: Strands of the magnetic carpet at 1 AU? J Geophys Res Space Phys 113(A8). https://doi.org/10.1029/2007JA012684

Borovsky JE (2020) The magnetic structure of the solar wind: ionic composition and the electron strahl. Geophys Res Lett 47:e2019GL084586. https://doi.org/10.1029/2019GL084586

Borovsky JE, Denton MH (2010) Solar wind turbulence and shear: a superposed-epoch analysis of corotating interaction regions at 1 AU. J Geophys Res 115(A):10101. https://doi.org/10.1029/2009JA014966

Borovsky JE, Podesta JJ (2015) Exploring the effect of current sheet thickness on the high-frequency Fourier spectrum breakpoint of the solar wind. J Geophys Res Space Phys 120(11):9256–9268. https://doi.org/10.1002/2015JA021622

Bower JS, Moebius E, Berger L, et al (2019) Effect of rapid changes of solar wind conditions on the pickup ion velocity distribution. J Geophys Res Space Phys 124(8):6418–6437. https://doi.org/10.1029/2019JA026781

Bruno R, Carbone V (2013) The solar wind as a turbulence laboratory. Living Rev Sol Phys 10:2. https://doi.org/10.12942/lrsp-2013-2

Burlaga LF, Ness NF (1998) Magnetic field strength distributions and spectra in the heliosphere and their significance for cosmic ray modulation: Voyager 1, 1980–1994. J Geophys Res 103:29719. https://doi.org/10.1029/98JA02682

Burlaga LF, Ness NF (2016) Observations of the interstellar magnetic field in the outer heliosheath: Voyager 1. Astrophys J 829:134. https://doi.org/10.3847/0004-637x/829/2/134

Burlaga LF, McDonald FB, Ness NF (1993) Cosmic ray modulation and the distant heliospheric magnetic field: Voyager 1 and 2 observations from 1986 to 1989. J Geophys Res 98(A1):1–12. https://doi.org/10.1029/92JA01979

Burlaga LF, Wang C, Richardson JD, Ness NF (2003) Large-scale magnetic field fluctuations and development of the 1999–2000 global merged interaction region: 1–60 AU. Astrophys J 585:1158. https://doi.org/10.1086/346108

Burrows RH, Zank GP, Webb GM, et al (2010) Pickup ion dynamics at the heliospheric termination shock observed by Voyager 2. Astrophys J 715:1109–1116

Bzowski M (2008) Survival probability and energy modification of hydrogen energetic neutral atoms on their way from the termination shock to Earth orbit. Astron Astrophys 488:1057–1068. https://doi.org/10.1051/0004-6361:200809393

Bzowski M, Mäkinen T, Kyrölä E, et al (2003) Latitudinal structure and North-south asymmetry of the solar wind from Lyman-α remote sensing by SWAN. Astron Astrophys 408:1165–1177. https://doi.org/10.1051/0004-6361:20031022

Bzowski M, Sokół JM, Tokumaru M, et al (2013) Solar parameters for modeling the interplanetary background. In: Bonnet RM, Quémerais E, Snow M (eds) Cross-calibration of past and present far UV spectra of Solar System objects and the heliosphere. ISSI scientific report series, vol 13. Springer, New York, pp 67–138. https://doi.org/10.1007/978-1-4614-6384-9_3

Bzowski M, Wawrzaszek R, Strumik M, et al (2025). GLObal solar Wind Structure (GLOWS). Space Sci Rev 221:105. https://doi.org/10.1007/s11214-025-01233-y

Caprioli D, Spitkovsky A (2014) Simulations of ion acceleration at non-relativistic shocks. II. Magnetic field amplification. Astrophys J 794:46. https://doi.org/10.1088/0004-637X/794/1/46

Caprioli D, Haggerty CC, Blasi P (2020) Kinetic simulations of cosmic-ray-modified shocks. II. Particle spectra. Astrophys J 905:2. https://doi.org/10.3847/1538-4357/abbe05

Chalov SV, Fahr HJ (2006) Pickup interstellar helium ions in the region of the solar gravitational cone. Astron Lett 32(7):487–494. https://doi.org/10.1134/s1063773706070061

Chalov SV, Alexashov DB, McComas D, et al (2010) Scatter-free pickup ions beyond the heliopause as a model for the interstellar boundary explorer ribbon. Astrophys J 716:L99

Chepurnov A, Lazarian A (2010) Extending the big power law in the sky with turbulence spectra from Wisconsin Hα mapper data. Astrophys J 710(1):853–858. https://doi.org/10.1088/0004-637x/710/1/853

Chhiber R, Usmanov AV, Matthaeus WH, Goldstein ML (2019) Contextual predictions for the Parker Solar Probe. I. Critical surfaces and regions. Astrophys J Suppl Ser 241:11. https://doi.org/10.3847/1538-4365/ab0652

Chotoo K, Schwadron NA, Mason GM, et al (2000) The suprathermal seed population for corotating interaction region ions at 1 AU deduced from composition and spectra of H+, He++, and He+ observed on wind. J Geophys Res Space Phys 105(A10):23107–23122. https://doi.org/10.1029/1998JA000015

Christian ER, Mitchell JG, Bruno A, et al (2026) The High-energy Ion Telescope (HIT) for the Interstellar Mapping and Acceleration Probe (IMAP) Mission. Space Sci Rev 222

Cohen CMS, Stone EC, Mewaldt RA, et al (2005) Heavy ion abundances and spectra from the large solar energetic particle events of October-November 2003. J Geophys Res 110:A09S16. https://doi.org/10.1029/2005ja011004

Cohen IJ, Schwartz SJ, Goodrich KA, et al (2019) High-Resolution Measurements of the Cross-Shock Potential, Ion Reflection, and Electron Heating at an Interplanetary Shock by MMS. J Geophys Res Space Phys 124(6). https://doi.org/10.1029/2018JA026197

Cohen CMS, Christian ER, Cummings AC, et al (2021) Parker Solar Probe observations of He/H abundance variations in SEP events inside 0.5 au. Astron Astrophys 650:A23

Cuesta ME, Chhiber R, Roy S, Goodwill J, Pecora F, et al (2022) Isotropization and evolution of energy-containing eddies in solar wind turbulence: Parker Solar Probe, Helios 1, ACE, WIND, and Voyager 1. Astrophys J Lett 932:L11. https://doi.org/10.3847/2041-8213/ac73fd

Cummings AC, Kóta J, Richardson JD, et al (2024) On the acceleration site of anomalous cosmic rays: Voyager 2 observations of their anisotropy in the heliosheath. Astrophys J 977:76. https://doi.org/10.3847/1538-4357/ad8e66

Dalla S, Marsh MS, Kelly J, Laitinen T (2013) Solar Energetic Particle drifts in the Parker spiral. J Geophys Res 118. https://doi.org/10.1002/jgra.50589

Dalla S, Marsh MS, Battarbee M (2017) Solar energetic particle drifts and the energy dependence of 1 AU charge states. Astrophys J 834:167. https://iopscience.iop.org/article/10.3847/1538-4357/834/2/167

Dayeh MA, Desai MI, Dwyer J, et al (2009) Composition and spectral properties of the 1 AU quiet-time suprathermal ion population during solar cycle 23. Astrophys J 693:1588. https://doi.org/10.1088/0004-637X/693/2/1588

Dayeh MA, McComas DJ, Livadiotis G, et al (2011) Spectral properties of regions and structures in the Interstellar Boundary Explorer (IBEX) sky maps. Astrophys J 734:29. https://doi.org/10.1088/0004-637X/734/1/29

Dayeh MA, Desai MI, Mason GM, et al (2017) Origin and properties of quiet-time 0.11–1.28 MeV nucleon^{-1} heavy-ion population near 1 au. Astrophys J 835:155. https://doi.org/10.3847/1538-4357/835/2/155

de Koning CA, Gosling JT, Skoug RM, Steinberg JT (2006) Widths of suprathermal pitch angle distributions during solar electron bursts: ACE observations. Geophys Res Lett 111:A04101. https://doi.org/10.1029/2005JA011326

de Koning CA, Gosling JT, Skoug RM, Steinberg JT (2007) Energy dependence of electron pitch angle distribution widths in solar bursts. Geophys Res Lett 112:A04101. https://doi.org/10.1029/2006JA011971

Decker RB (1983) Formation of shock-spike events at quasi-perpendicular shocks. J Geophys Res Space Phys 88(A12):9959–9973. https://doi.org/10.1029/JA088iA12p09959

Desai M, Giacalone J (2016) Large gradual solar energetic particle events. Living Rev Sol Phys 13:3. https://doi.org/10.1007/s41116-016-0002-5

Desai MI, Mason GM, Dwyer JR, et al (2001) Acceleration of ^{3}He nuclei at interplanetary shocks. Astrophys J 553(1):L89–L92. https://doi.org/10.1086/320503

Desai MI, Mason GM, Dwyer JR, et al (2003) Evidence for a suprathermal seed population of heavy ions accelerated by interplanetary shocks near 1 AU. Astrophys J 588(2):1149–1162. https://doi.org/10.1086/374310

Desai MI, Mason GM, Gold RE, et al (2006b) Heavy-ion elemental abundances in large solar energetic particle events and their implications for the seed population. Astrophys J 649(1):470–489. https://doi.org/10.1086/505649

Desai MI, Mason GM, Mazur JE, Dwyer JR (2006a) Solar cycle variations in the composition of the suprathermal heavy-ion population near 1 AU. Astrophys J 645(1):L81–L84. https://doi.org/10.1086/505935

Desai MI, Mason GM, Dayeh MA, et al (2016) Spectral properties of large gradual solar energetic particle events. II. Systematic Q/M dependence of heavy ion spectral breaks. Astrophys J 828(2):106. https://doi.org/10.3847/0004-637x/828/2/106

Di Matteo S, Villante U, Viall N, et al (2022) On differentiating multiple types of ulf magnetospheric waves in response to solar wind periodic density structures. J Geophys Res Space Phys 127(3):e2021JA030144. https://doi.org/10.1029/2021JA030144

Drews C, Berger L, Wimmer-Schweingruber RF, et al (2012) Inflow direction of interstellar neutrals deduced from pickup ion measurements at 1 AU. J Geophys Res Space Phys 117(A9). https://doi.org/10.1029/2012JA017746

Drews C, Berger L, Taut A, et al (2015) STEREO PLASTIC observations. Astron Astrophys 575:1–13. https://doi.org/10.1051/0004-6361/201425271

Dutta A, Goswami JN, Biswas S, et al (1993) Ionization states of low-energy cosmic rays: results from spacelab 3 cosmic-ray experiment. Astrophys J 411:418. https://doi.org/10.1086/172844

Eastwood J, Lucek EA, Mazelle C, et al (2005) The foreshock. Space Sci Rev. https://doi.org/10.1007/s11214-005-3824-3

Elliott HA, McComas DJ, Valek P, et al (2016) The New Horizons Solar Wind Around Pluto (SWAP) observations of the solar wind from 11–33 au. Astrophys J Suppl Ser 223:19. https://doi.org/10.3847/0067-0049/223/2/19

Elliott HA, McComas DJ, Zirnstein EJ, et al (2019) Slowing of the solar wind in the outer heliosphere. Astrophys J 885(2):156. https://doi.org/10.3847/1538-4357/ab3e49

Eriksson S, Swisdak M, Weygand JM, et al (2022) Characteristics of multi-scale current sheets in the solar wind at 1 au associated with magnetic reconnection and the case for a heliospheric current sheet avalanche. Astrophys J 933(2):181. https://doi.org/10.3847/1538-4357/ac73f6

Feldman WC, Asbridge JR, Bame SJ, et al (1975) Solar wind electrons. J Geophys Res 80(31):4181–4196. https://doi.org/10.1029/JA080i031p04181

Feldman WC, Asbridge JR, Bame SJ, et al (1978) Characteristic electron variations across simple high-speed solar wind streams. J Geophys Res 83(A11):5285–5295. https://doi.org/10.1029/JA083iA11p05285

Feldman WC, Asbridge JR, Bame SJ, Gosling JT (1982) Quantitative tests of a steady state theory of solar wind electrons. J Geophys Res 87(A9):7355–7362. https://doi.org/10.1029/JA087iA09p07355

Fennell JF, Mizera PF, Croley D Jr (1975) Low energy polar cap electrons during quiet times. In: Proceedings of the 14th international cosmic ray conference, München, Germany, 15–29 August, vol 4, p 1267

Fermi E (1949) On the origin of the cosmic radiation. Phys Rev 75:1169. https://doi.org/10.1103/PhysRev.75.1169

Fisk LA, Koslovsky B, Ramaty R (1974) An interpretation of the observed oxygen and nitrogen enhancements in low-energy cosmic rays. Astrophys J 190:L35–L37. https://doi.org/10.1086/181498

Florinski V, Decker RB, Le Roux JA, Zank GP (2009) An energetic-particle-mediated termination shock observed by Voyager 2. Geophys Res Lett 36:L12101. https://doi.org/10.1029/2009GL038423

Florinski V, Zank GP, Heerikhuisen J, Hu Q, Khazanov I (2010) Stability of a pickup ion ring-beam population in the outer heliosheath: implications for the IBEX ribbon. Astrophys J 719:1097

Fraternale F, Adhikari L, Fichtner H, et al (2022) Turbulence in the outer heliosphere. Space Sci Rev 218:1. https://doi.org/10.1007/s11214-022-00914-2

Galli A, et al (2014) Imaging the heliosphere using neutral atoms from solar wind energy down to 15 eV. Astrophys J 796:9. https://doi.org/10.1088/0004-637X/796/1/9

Galvin AB, Kistler LM, Popecki MA, et al (2008) The plasma and suprathermal ion composition (PLASTIC) investigation on the STEREO observatories. Space Sci Rev 136(1–4):437–486. https://doi.org/10.1007/s11214-007-9296-x

Gamayunov K, Zhang M, Rassoul H (2010) Pitch angle scattering in the outer heliosheath and formation of the Interstellar Boundary EXplorer ribbon. Astrophys J 725:2251

Geiss J, Gloeckler G, Fisk LA, von Steiger R (1995) C+ pickup ions in the heliosphere and their origin. J Geophys Res 100:23,373

Ghag K, Tari P, Raghav A, et al (2023) The role of extreme geomagnetic storms in the Forbush decrease profile observed by neutron monitors. J Atmos Sol-Terr Phys 252:106146. https://doi.org/10.1016/j.jastp.2023.106146

Giacalone J (2003a) The physics of particle acceleration by collisionless shocks. Planet Space Sci 51:659. https://doi.org/10.1016/S0032-0633(03)00101-6

Giacalone J (2003b) The physics of particle acceleration by collisionless shocks. Planet Space Sci 51(11):659–664. https://doi.org/10.1016/S0032-0633(03)00101-6

Giacalone J (2005) The efficient acceleration of thermal protons by perpendicular shocks. Astrophys J 628(1):L37–L40. https://doi.org/10.1086/432510

Giacalone J (2012) Energetic charged particles associated with strong interplanetary shocks. Astrophys J 761(1). https://doi.org/10.1088/0004-637X/761/1/28

Giacalone J, Decker R (2010) The origin of low-energy anomalous cosmic rays at the solar-wind termination shock. Astrophys J 710:91

Giacalone J, Jokipii JR (1997) Spatial variation of accelerated pickup ions at co-rotating interaction regions. Geophys Res Lett 24(14):1723–1726. https://doi.org/10.1029/97GL01631

Giacalone J, Jokipii JR (2015) A new model for the heliosphere's "IBEX ribbon". Astrophys J 812:L9

Giacalone J, Jokipii JR, Kóta J (1994) Ion injection and acceleration at quasi-perpendicular shocks. J Geophys Res 99:19351. https://doi.org/10.1029/94JA01213

Giacalone J, Drake JF, Jokipii JR (2012) The acceleration mechanism of anomalous cosmic rays. Space Sci Rev 173:283–307. https://doi.org/10.1007/s11214-012-9915-z

Giacalone J, Nakanotani M, Zank GP, et al (2021) Hybrid simulations of interstellar pickup protons accelerated at the solar-wind termination shock at multiple locations. Astrophys J 911:27. https://doi.org/10.3847/1538-4357/abe93a

Giacalone J, Fahr H, Fichtner H, et al (2022) Anomalous cosmic rays and heliospheric energetic particles. Space Sci Rev 218:22. https://doi.org/10.1007/s11214-022-00890-7

Giacalone J, Cohen CMS, McComas DJ, et al (2023) Analyses of ∼0.05–2 MeV ions associated with the 2022 February 16 energetic storm particle event observed by Parker Solar Probe. Astrophys J 958(2):144. https://doi.org/10.3847/1538-4357/acfb86

Giacalone J, Kornbleuth M, Opher M, et al (2025) Hybrid simulations of interstellar pickup ions at the solar wind termination shock revisitied. Astrophys J 980:29. https://doi.org/10.3847/1538-4357/ada89c

Gkioulidou M, Opher M, Kornbleuth M, et al (2022) On the energization of pickup ions downstream of the heliospheric termination shock by comparing 0.52-55 keV observed energetic neutral atom spectra to ones inferred from proton hybrid simulations. Astrophys J Lett 931:L21. https://doi.org/10.3847/2041-8213/ac6beb

Gloeckler G, Geiss J (2001) Heliospheric and interstellar phenomena deduced from pickup ion observations. Space Sci Rev 97(1/4):169–181. https://doi.org/10.1023/A:1011867320416

Gloeckler G, Fisk LA, Ipavich FM, et al (1994) Acceleration of interstellar pickup ions in the disturbed solar wind observed on Ulysses. J Geophys Res 99(A9):17637–17644

Gloeckler G, Fisk LA, Geiss J, et al (2000) The elemental composition of inner source pickup ions. J Geophys Res 105:7459

Gosling JT (1983) Ion acceleration at shocks in interplanetary space: a brief review of recent observations. Space Sci Rev 34:113. https://doi.org/10.1007/BF00194621

Gosling JT, Asbridge JR, Bame SJ, et al (1981) Interplanetary ions during an energetic storm particle event: the distribution function from solar wind thermal energies to 1.6 MeV. J Geophys Res 86:547–554. https://doi.org/10.1029/JA086iA02p00547

Gosling JT, Baker DN, Bame SJ, Feldman WC (1986) Bidirectional solar wind electron heat flux and hemispherically symmetric polar rain. J Geophys Res 91:11352

Gosling JT, Bame SJ, Feldman WC, et al (1993) Counterstreaming suprathermal electron events upstream of corotating shocks in the solar wind beyond approximately 2 AU Ulysses. Geophys Res Lett 20:2335–2338. https://doi.org/10.1029/93GL02489

Gosling JT, Skoug RM, Feldman WC (2001) Solar wind electron halo depletions at 90 pitch angle. Geophys Res Lett 28:4155–4158. https://doi.org/10.1029/2001GL013758

Gosling JT, Skoug RM, Feldman WC, McComas DJ (2002) Symmetric suprathermal electron depletions on closed field lines in the solar wind. Geophys Res Lett 29(12):1573. https://doi.org/10.1029/2001GL013949

Gosling JT, Skoug RM, McComas DJ (2003) Solar electron bursts at very low energies: evidence for acceleration in the high corona? Geophys Res Lett 30(13):1697. https://doi.org/10.1029/2003GL017079

Gosling JT, de Koning CA, Skoug RM, Steinberg JT, McComas DJ (2004b) Dispersionless modulations in the low-energy solar electron bursts and discontinuous changes in the solar wind electron strahl. J Geophys Res 109:A05102. https://doi.org/10.1029/2003JA010338

Gosling JT, Skoug RM, McComas DJ (2004a) Low-energy solar electron bursts and solar wind stream structure at 1 AU. J Geophys Res 109:A04104. https://doi.org/10.1029/2003JA010309

Gosling JT, Skoug RM, Haggerty DK, McComas DJ (2005) Absence of energetic particle effects associated with magnetic reconnection exhausts in the solar wind. Geophys Res Lett 32:L14113. https://doi.org/10.1029/2005GL023357

Gruntman MA (1996) H_2^+ pickup ions in the solar wind: outgassing of interplanetary dust. J Geophys Res 101:15,555–15,568

Gruntman M, Roelof EC, Mitchell DG, et al (2001) Energetic neutral atom imaging of the heliospheric boundary region. J Geophys Res 106:15767. https://doi.org/10.1029/2000JA000328

Guo F, Zhao L, Cohen CMS, et al (2022) Variable ion compositions of solar energetic particle events in the inner heliosphere: a field line braiding model with compound injections. Astrophys J 924:22. https://doi.org/10.3847/1538-4357/ac3233

Gussenhoven MS, Hardy DA, Heinemann N, Burkhardt RK (1984) Morphology of the polar rain. J Geophys Res Space Phys 89(A11):9785–9800. https://doi.org/10.1029/JA089iA11p09785

Haggerty CC, Caprioli D (2020) Kinetic simulations of cosmic-ray-modified shocks. I. Hydrodynamics. Astrophys J 905:1. https://doi.org/10.3847/1538-4357/abbe06

Heerikhuisen J, Pogorelov N, Zank G (2010a) IBEX ribbon from outer heliosheath pick-up ions. AIP Conf Proc 1302:98–103. https://doi.org/10.1063/1.3529997

Heerikhuisen J, Pogorelov NV, Zank GP, et al (2010b) Pick-up ions in the outer heliosheath: a possible mechanism for the interstellar boundary EXplorer ribbon. Astrophys J Lett 708:L126–L130. https://doi.org/10.1088/2041-8205/708/2/L126

Hewish A, Scott PF, Wills D (1964) Interplanetary scintillation of small diameter radio sources. Nature 203:1214–1217. https://doi.org/10.1038/2031214a0

Horbury TS, O'Brien H, Greenaway C, et al (2026) The IMAP magnetometer. Space Sci Rev 222

Isenberg PA (1986) Interaction of the solar wind with interstellar neutral hydrogen: three-fluid model. J Geophys Res Space Phys 91(A9):9965–9972. https://doi.org/10.1029/JA091iA09p09965

Isenberg PA (1987) Evolution of interstellar pickup ions in the solar wind. J Geophys Res Space Phys 92(A2):1067–1073. https://doi.org/10.1029/JA092iA02p01067

Isenberg PA (2014) Spatial confinement of the IBEX ribbon: a dominant turbulence mechanism. Astrophys J 787:76

Izmodenov V, Alexashov D, Myasnikov A (2005) Direction of the interstellar H atom inflow in the heliosphere: role of the interstellar magnetic field. Astron Astrophys 437(3):L35–L38. https://doi.org/10.1051/0004-6361:200500132

Jackson BV, Hick PP, Buffington A, et al (2011) Three-dimensional reconstruction of heliospheric structure using iterative tomography: a review. J Atmos Terr Phys 73:1214–1227. https://doi.org/10.1016/j.jastp.2010.10.007

Jocelyn JA (1980) A prominent cause for magnetic storms. Sci News 117:391

Jokipii JR (1966) Cosmic-ray propagation. I. Charged particles in a random magnetic field. Astrophys J 146:480. https://doi.org/10.1086/148912

Jokipii JR (1986) Particle acceleration at a termination shock 1. Application to the solar wind and the anomalous component. J Geophys Res 91:2929

Jokipii JR, Giacalone J (1996) The acceleration of pickup ions. Space Sci Rev 78(1):137–148. https://doi.org/10.1007/BF00170800

Jokipii JR, Thomas B (1981) Effects of drift on the transport of cosmic rays. IV. Modulation by a wavy interplanetary current sheet. Astrophys J 243:1115–1122

Jokipii JR, Giacalone J, Kota J (2004) Transverse streaming anisotropies of charged particles accelerated at the solar wind termination shock. Astrophys J 611:L141

Jones FC, Ellison DC (1991) The plasma physics of shock acceleration. Space Sci Rev 58:259–346. https://doi.org/10.1007/BF01206003

Kahler SW, Brown D (2021) Variations of peak He/H ratios in solar energetic (E > 4 MeV) particle events and comparisons with solar wind He/H ratios. Astrophys J 908:214

Kallenbach R, Hilchenbach M, Chalov SV, et al (2005) On the "injection problem" at the solar wind termination shock. Astron Astrophys 439(1):1–22. https://doi.org/10.1051/0004-6361:20052874

Kanekal SG (2006) A review of recent observations of relativistic electron energization in the Earth's outer Van Allen radiation belt. In: Gopalswamy N, Bhattacharyya A (eds) Proceedings of the ILWS workshop, p 274. ISBN 81-87099-40-2

Katushkina OA, Izmodenov VV, Quémerais E, Sokół JM (2013) Heliolatitudinal and time variations of the solar wind mass flux: inferences from the backscattered solar Lyman-alpha intensity maps. J Geophys Res 118:1–9. https://doi.org/10.1002/jgra.50303

Katushkina O, Izmodenov V, Koutroumpa D, Quémerais E, Jian LK (2019) Unexpected behavior of the solar wind mass flux during solar maxima: two peaks at middle heliolatitudes. Sol Phys 294:17. https://doi.org/10.1007/s11207-018-1391-5

Keebler TB, Tóth G, Zieger B, et al (2022) MSWIM2D: two-dimensional outer heliosphere solar wind modeling. Astrophys J Suppl Ser 260(2):43. https://doi.org/10.3847/1538-4365/AC67EB

Kepko L, Viall NM (2019) The source, significance, and magnetospheric impact of periodic density structures within stream interaction regions. J Geophys Res Space Phys 124(10):7722–7743. https://doi.org/10.1029/2019JA026962

Kim TK, Pogorelov NV, Zank GP, et al (2016) Modeling the solar wind at the Ulysses, Voyager, and new horizons spacecraft. Astrophys J 832(1):72. https://doi.org/10.3847/0004-637X/832/1/72

Klecker B (1995) The anomalous component of cosmic rays in the 3-D heliosphere. Space Sci Rev 72:419–430. https://doi.org/10.1007/BF00768815

Klecker B, Möbius E, Popecki MA (2007) Ionic charge states of solar energetic particles: a clue to the source. Space Sci Rev 130:273. https://doi.org/10.1007/s11214-007-9207-1

Klein K-L, Dalla S (2017) Acceleration and propagation of solar energetic particles. Space Sci Rev 212:1107–1136. https://doi.org/10.1007/s11214-017-0382-4

Kleinmann J, et al (2022) The structure of the large-scale heliosphere as seen by current models. Space Sci Rev 218:36. https://doi.org/10.1007/s11214-022-00902-6

Kolmogorov AN (1962) A refinement of previous hypotheses concerning the local structure of turbulence in a viscous incompressible fluid at high Reynolds number. J Fluid Mech 13:82. https://doi.org/10.1017/S0022112062000518

Kota J, Jokipii JR (1983) Effects of drift on the transport of cosmic rays. VI. A three-dimensional model including diffusion. Astrophys J 265:573–581

Koutroumpa D, Quémerais E, Ferron S, Schmidt W (2019) Global distribution of the solar wind and velocity from SOHO/SWAN during SC-23 and SC-24. Geophys Res Lett 46:4114–4121. https://doi.org/10.1029/2019GL082402

Krymsky GF (1977) A regular mechanism for the acceleration of charged particles on the front of a shock wave. Dokl Akad Nauk SSSR 234:1306

Kubiak MA, Bzowski M, Kowalska-Leszczynska I, Strumik M (2021a) WawHelioGlow: a model of the heliospheric backscatter glow. I. Model definition. Astrophys J Suppl Ser 254:16. https://doi.org/10.3847/1538-4365/abeb79

Kubiak MA, Bzowski M, Kowalska-Leszczynska I, Strumik M (2021b) WawHelioGlow: a model of the heliospheric backscatter glow. II. The helioglow buildup and the potential significance of the anisotropy in the solar EUV output. Astrophys J Suppl Ser 254:17. https://doi.org/10.3847/1538-4365/abeb78

Kucharek H, Möbius E, Li W, et al (2003) On the source and acceleration of energetic He+: a long-term observation with ACE/SEPICA. J Geophys Res Space Phys 108(A10). https://doi.org/10.1029/2003JA009938

Kurien LV, Kanekal SG, Di Matteo S, et al (2024) Outer zone relativistic electron response to mesoscale periodic density structures in the solar wind: Van Allen Probes measurements. J Geophys Res Space Phys 129:e2024JA032614. https://doi.org/10.1029/2024JA032614

Lallement R, Quémerais E, Bertaux JL, et al (2005) Deflection of the interstellar neutral hydrogen flow across the heliospheric interface. Science 307(5714):1447–1449. https://doi.org/10.1126/science.1107953

Lallement R, Quémerais E, Koutroumpa D, et al (2010) The interstellar flow: updated analysis of SOHO/SWAN data. In: Solar wind 12. AIP conf proc, vol 1216, pp 555–558. https://doi.org/10.48550/arXiv.1003.4243

Le Chat G, Issautier K, Meyer-Vernet N (2012) The solar wind energy flux. Sol Phys 279:197–205. https://doi.org/10.1007/s11207-012-9967-y

Le Roux JA, Zank GP, Matthaeus WH (2002) Pickup ion acceleration by turbulent field-aligned electric fields in the slow low-latitude solar wind. J Geophys Res Space Phys 107(A7):1–18. https://doi.org/10.1029/2001JA000285

Lee MA (1983) Coupled hydromagnetic wave excitation and ion acceleration at interplanetary traveling shocks. J Geophys Res 88(A8):6109–6119. https://doi.org/10.1029/JA088iA08p06109

Lee MA (2005) Coupled hydromagnetic wave excitation and ion acceleration at an evolving coronal/interplanetary shock. Astrophys J Suppl Ser 158(1):38–67. https://doi.org/10.1086/428753

Lee MA, Ip WH (1987) Hydromagnetic wave excitation by ionized interstellar hydrogen and helium in the solar wind. J Geophys Res 92(A10):11041–11052

Lee MA, Jokipii JR (1976) The irregularity spectrum in interstellar space. Astrophys J 202:439–453. https://doi.org/10.1086/154434

Lee MA, Shapiro VD, Sagdeev RZ (1996) Pickup ion energization by shock surfing. J Geophys Res 101:4777–4790

Lee MA, Kucharek H, Möbius E, et al (2012) An analytical model of interstellar gas in the heliosphere tailored to interstellar boundary explorer observations. Astrophys J Suppl Ser 198(2):10. https://doi.org/10.1088/0067-0049/198/2/10

Lee CO, Christian ER, Sandoval L, et al (2025) Space weather science to enhance forecasting with the NASA IMAP Active Link for Real-Time (I-ALiRT) system. Space Sci Rev 221:117. https://doi.org/10.1007/s11214-025-01244-9

Lembège B, Yang Z, Zank GP (2020) Energy power spectra measured at an interplanetary shock by the New Horizon's SWAP experiment: 1D full particle simulations versus observations. Astrophys J 890:48. https://doi.org/10.3847/1538-4357/ab65c5

Leske RA, Mewaldt RA, Cohen CMS, et al (1999) Event-to-event variations in the isotopic composition of neon in solar energetic particle events. Geophys Res Lett 26:2693–2696

Li G, Zank GP, Verkhoglyadova O, et al (2009) Shock geometry and spectral breaks in large SEP events. Astrophys J 702(2):998–1004. https://doi.org/10.1088/0004-637X/702/2/998

Lin RP (1985) Energetic solar electrons in the interplanetary medium. Sol Phys 100:537. https://doi.org/10.1007/BF00158444

Lin RP, Larson D, McFadden J, et al (1996) Observation of an impulsive solar electron event extending down to ∼0.5 keV energy. Geophys Res Lett 23:1211–1214. https://doi.org/10.1029/96GL00710

Lin RP, Larson DE, Ergun RE, et al (1997) Observations of the solar wind, the bow shock, and upstream particles with the wind 3DP plasma instrument. Adv Space Res 20:645–654. https://doi.org/10.1016/S0273-1177(97)00452-3

Liu K, Möbius E, Gary SP, Winske D (2012) Pickup proton instabilities and scattering in the distant solar wind and the outer heliosheath: hybrid simulations. J Geophys Res 117:A10102. https://doi.org/10.1029/2012JA017969

Liu TZ, Lu S, Angelopoulos V, Lin Y, Wang XY (2018) Ion acceleration inside foreshock transients. J Geophys Res Space Phys 123:163–178. https://doi.org/10.1002/2017JA024838

Liu TZ, Angelopoulos V, Lu S (2019) Relativistic electrons generated at Earth's quasi-parallel bow shock. Sci Adv 5. https://doi.org/10.1126/sciadv.aaw1368

Liu TZ, Lu S, Turner DL, et al (2020) Magnetospheric Multiscale (MMS) observations of magnetic reconnection in foreshock transients. J Geophys Res Space Phys 125:e27822. https://doi.org/10.1029/2020JA027822

Livadiotis G (2017) Kappa distribution: theory & applications in plasmas, Elsevier, Amsterdam

Livadiotis G (2018) Connection of turbulence with polytropic index in the solar wind proton plasma. Entropy 21:1041. https://doi.org/10.3390/e21111041

Livadiotis G, McComas DJ (2023a) Connection between polytropic index and heating. Astrophys J 956:88. https://doi.org/10.3847/1538-4357/acf45d

Livadiotis G, McComas DJ (2023b) Entropy defect in thermodynamics. Sci Rep 13:9033. https://doi.org/10.1038/s41598-023-36080-w

Livadiotis G, McComas DJ (2023c) Transport equation of kappa distributions in the heliosphere. Astrophys J 954:72. https://doi.org/10.3847/1538-4357/ace1e3

Livadiotis G, McComas DJ, Shrestha BL (2024) Thermodynamics of pickup ions in the heliosphere. Astrophys J 968:66. https://doi.org/10.3847/1538-4357/ad3e79

Livi S, Desai MI, Ogasawara K, et al (2026) The Compact Dual Ion Composition Experiment (CoDICE) for the IMAP Mission. Space Sci Rev 222:1. https://doi.org/10.1007/s11214-025-01251-w

Mason GM (2000) Composition and energy spectra of ions accelerated in corotating interaction regions. AIP Conf Proc 528:234–241

Mason GM, Gloeckler G (2012) Power law distributions of suprathermal ions in the quiet solar wind. Space Sci Rev 172:241–251. https://doi.org/10.1007/s11214-010-9741-0

Matthaeus WH, Smith CW, Oughton S (1998) Dynamical age of solar wind turbulence in the outer heliosphere. J Geophys Res 103:6495. https://doi.org/10.1029/97JA03729

Matthaeus WH, Dasso S, Weygand JM, et al (2005) Spatial correlation of solar-wind turbulence from two-point measurement. Phys Rev Lett 95:231101. https://doi.org/10.1103/PhysRevLett.95.231101

Matthaeus WH, Weygand JM, Dasso S (2016) Ensemble space-time correlation of plasma turbulence in the solar wind. Phys Rev Lett 116:245101. https://doi.org/10.1103/PhysRevLett.116.245101

Mazur JE, Mason GM, Dwyer JR, et al (2000) Interplanetary magnetic field line mixing deduced from impulsive solar flare particles. Astrophys J 532:L79

McComas DJ (2009a) ENA imaging of the inner heliosheath—preparing for the Interstellar Boundary Explorer (IBEX). Space Sci Rev 143(1–4):125–138. https://doi.org/10.1007/s11214-008-9410-8

McComas DJ, Schwadron NA (2006) An explanation of the Voyager paradox: particle acceleration at a blunt termination shock. Geophys Res Lett 33:L04102

McComas DJ, Barraclough BL, Funsten HO, et al (2000) Solar wind observations over Ulysses' first full polar orbit. J Geophys Res 105(A5):10419–10433. https://doi.org/10.1029/1999JA00038

McComas D, Allegrini F, Bagenal F, et al (2008b) The Solar Wind Around Pluto (SWAP) instrument aboard new horizons. Space Sci Rev 140:261–313. https://doi.org/10.1007/s11214-007-9205-3

McComas DJ, Ebert RW, Elliott HA, et al (2008a) Weaker solar wind from the polar holes and the whole Sun. Geophys Res Lett 35:L18103. https://doi.org/10.1029/2008GL034896

McComas DJ, Allegrini F, Bochsler P, et al (2009b) Global observations of the interstellar interaction from the Interstellar Boundary Explorer (IBEX). Science 326:959. https://doi.org/10.1126/science.1180906

McComas DJ, et al (2012) The first three years of IBEX observations and our evolving heliosphere. Astrophys J Suppl Ser 203:1

McComas DJ, Dayeh MA, Funsten HO, et al (2013) The heliotail revealed by the interstellar boundary explorer. Astrophys J 771:77. https://doi.org/10.1088/0004-637X/771/2/77

McComas DJ, Lewis WS, Schwadron NA (2014) IBEX's enigmatic ribbon in the sky and its many possible sources: the IBEX ribbon and its sources. Rev Geophys 52(1):118–155. https://doi.org/10.1002/2013RG000438

McComas DJ, Zirnstein EJ, Bzowski M, et al (2017) Interstellar pickup ion observations to 38 au. Astrophys J Suppl Ser 233(1). https://doi.org/10.3847/1538-4365/aa91d2

McComas DJ, Christian ER, Schwadron NA, et al (2018a) Interstellar Mapping and Acceleration Probe (IMAP): a new NASA mission. Space Sci Rev 221:100. https://doi.org/10.1007/s11214-025-01224-z

McComas DJ, Dayeh MA, Funsten HO, et al (2018b) Heliosphere responds to a large solar wind intensification: decisive observations from IBEX. Astrophys J Lett 856:L10. https://doi.org/10.3847/2041-8213/aab611

McComas DJ, Dayeh MA, Funsten HO, et al (2019a) Expanding global features in the outer heliosphere. Astrophys J 872:127. https://doi.org/10.3847/1538-4357/aafc2c

McComas DJ, Rankin JS, Schwadron NA, Swaczyna P (2019b) Termination shock measured by Voyagers and IBEX. Astrophys J 884:145. https://doi.org/10.3847/1538-4357/ab441a

McComas DJ, Swaczyna P, Szalay JR, et al (2021) Interstellar pickup ion observations halfway to the termination shock. Astrophys J Suppl Ser 254:19. https://doi.org/10.3847/1538-4365/abee76

McComas DJ, Shrestha BL, Swaczyna P, et al (2022) First high-resolution observations of interstellar pickup ion mediated shocks in the outer heliosphere. Astrophys J 934(2):147. https://doi.org/10.3847/1538-4357/AC7956

McComas DJ, et al (2024) Fourteen years of energetic neutral atom observations from IBEX. Astrophys J Suppl Ser 270:17. https://doi.org/10.3847/1538-4365/ad0a69

McComas DJ, Christian ER, Schwadron NA, et al (2025b) Interstellar Mapping and Acceleration Probe: the NASA IMAP mission. Space Sci Rev 221:100. https://doi.org/10.1007/s11214-025-01224-z

McComas DJ, Shrestha BL, Livadiotis G, et al (2025a) Interstellar pickup ion observations to 60 au. Astrophys J 980:154. https://doi.org/10.3847/1538-4357/ada6b1

McDonald FB, Teegarden BJ, Trainor JH, Webber WR (1974) The anomalous abundance of cosmic ray nitrogen and oxygen nuclei at low energies. Astrophys J 185:L105

Mewaldt RA, Selesnick RS, Cummings JR, Stone EC, von Rosenvinge TT (1996) Evidence for multiply charged anomalous cosmic rays. Astrophys J Lett 466:L43

Mewaldt RA, Cohen CMS, Mason GM, et al (2005) In: Solar energetic particle spectral breaks. AIP conf proc, vol 781, pp 227–232. https://doi.org/10.1063/1.2032701

Mewaldt RA, Cohen CMS, Mason GM, et al (2007) On the differences in composition between solar energetic particles and solar wind. Space Sci Rev 130:207. https://doi.org/10.1007/s11214-007-9187-1

Möbius E, Hovestadt D, Klecker B, et al (1985) Direct observation of He$^+$ pick-up ions of interstellar origin in the solar wind. Nature 318(6045):426–429. https://doi.org/10.1038/318426a0

Möbius E, Klecker B, Hovestadt D, Scholer M (1988) Interaction of interstellar pick-up ions with the solar wind. Astrophys Space Sci 144(1–2):487–505. https://doi.org/10.1007/BF00793200

Möbius E, Rucinski D, Isenberg PA, Lee MA (1996) Determination of interstellar pickup ion distributions in the solar wind with SOHO and cluster. Ann Geophys 14(5):492–496. https://doi.org/10.1007/s00585-996-0492-x

Möbius E, et al (1998) The Solar Energetic Particle Ionic Charge Analyzer (SEPICA) and the Data Processing Unit (S3DPU) for SWICS, SWIMS and SEPICA. Space Sci Rev 86:447–495

Möbius E, Kucharek H, Clark G, et al (2009) Diagnosing the neutral interstellar gas flow at 1 AU with IBEX-Lo. Space Sci Rev 146(1–4):149–172. https://doi.org/10.1007/s11214-009-9498-5

Möbius E, Liu K, Funsten H, et al (2013) Analytic model of the IBEX ribbon with neutral solar wind based ion pickup beyond the heliopause. Astrophys J 766:129

Möbius E, Lee MA, Drews C (2015) Interstellar flow longitude from the symmetry of the pickup ion cutoff at 1 au. Astrophys J 815(1):20. https://doi.org/10.1088/0004-637X/815/1/20

Möbius E, Bower J, Aly A, et al (2019) Observation of suprathermal tails of He$^+$ pickup ions across solar wind compression regions with STEREO PLASTIC. J Phys Conf Ser 1332(1):012011. https://doi.org/10.1088/1742-6596/1332/1/012011

Montroll EW, Shlesinger MF (1982) On 1/f noise and other distributions with long tails. Proc Natl Acad Sci USA 79:3380. https://doi.org/10.1073/pnas.79.10.3380

Neugebauer M, Giacalone J (2005) Multispacecraft observations of interplanetary shocks: nonplanarity and energetic particles. J Geophys Res 110(A12):A12106. https://doi.org/10.1029/2005JA011380

Neugebauer M, Giacalone J (2015) Energetic particles, tangential discontinuities, and solar flux tubes. J Geophys Res 120(10):8281–8287. https://doi.org/10.1002/2015JA021632

Neugebauer M, Giacalone J, Chollet E, Lario D (2006) Variability of low-energy ion flux profiles on interplanetary shock fronts. J Geophys Res 111(A12):A12107. https://doi.org/10.1029/2006JA011832

Obukhov AM (1962) Some specific features of atmospheric turbulence. J Geophys Res 67:3011. https://doi.org/10.1029/JZ067i008p03011

Odstrcil D (2023) Heliospheric 3-D MHD ENLIL simulations of multi-CME and multi-spacecraft events. Front Astron Space Sci 10. https://doi.org/10.3389/fspas.2023.1226992

Ogasawara K, Dayeh MA, Ebert RW, et al (2025) Helium pickup ion velocity distributions observed in interplanetary coronal mass ejection structures. Astrophys J 981(1):35. https://doi.org/10.3847/1538-4357/adb1b4

Oka M, Terasawa T, Noda H, Saito Y, Mukai T (2002) 'Torus' distribution of interstellar helium pickup ions: direct observation. Geophys Res Lett 29:1688

Opher M, Richardson JD, Toth G, Gombosi TI (2009) Confronting observations and modeling: the role of the interstellar magnetic field in Voyager 1 and 2 asymmetries. Space Sci Rev 143(1–4):43–55. https://doi.org/10.1007/s11214-008-9453-x

Oschlies K, Beaujean R, Enge W (1989) On the charge state of anomalous oxygen. Astrophys J 345:776. https://doi.org/10.1086/167949

Padhye NS, Smith CW, Matthaeus WH (2001) Distribution of magnetic field components in the solar wind plasma. J Geophys Res 106:18635. https://doi.org/10.1029/2000JA000293

Parker LN, Zank GP, Hu Q (2014) Particle acceleration at quasi-perpendicular shock waves: Theory and observations at 1 AU. Astrophys J 782(1). https://doi.org/10.1088/0004-637X/782/1/52

Pesses ME, Jokipii JR, Eichler D (1981) Cosmic ray drift, shock wave acceleration, and the anomalous component of cosmic rays. Astrophys J 24:L85

Pogorelov NV, Borovikov SN, Zank GP, Ogino T (2009) Three-dimensional features of the outer heliosphere due to coupling between the interstellar and interplanetary magnetic fields. III. The effects of solar rotation and activity cycle. Astrophys J 696(2):1478–1490. https://doi.org/10.1088/0004-637X/696/2/1478

Pogorelov NV, Suess ST, Borovikov SN, Ebert RW, McComas DJ, Zank GP (2013) Three dimensional features of the outer heliosphere due to coupling between the interstellar and interplanetary magnetic fields, IV, solar cycle model based on Ulysses observations. Astrophys J 772:2. https://doi.org/10.1088/0004-637X/772/1/2

Pomoell J, Poedts S (2018) EUHFORIA: European heliospheric forecasting information asset. J Space Weather Space Clim 8:A35. https://doi.org/10.1051/swsc/2018020

Porowski C, Bzowski M, Tokumaru M (2022) A new 3D solar wind speed and density model based on interplanetary scintillation. Astrophys J 259:2. https://doi.org/10.3847/1538-4365/ac35d7

Porowski C, Bzowski M, Tokumaru M (2023) On the general correlation between 3D solar wind speed and density model and solar proxies. Astrophys J Suppl Ser 264:11. https://doi.org/10.3847/1538-4365/ac9fd4

Posner A (2007) Up to 1-hour forecasting of radiation hazards from solar energetic ion events with relativistic electrons. Space Weather 5(5):05001. https://doi.org/10.1029/2006SW000268

Posner A, Schwadron NA, Zurbuchen TH (2001) In: Scherer K, Fichtner H, Fahr HJ, Marsch E (eds) The outer heliosphere: the next frontiers, vol 315. https://ui.adsabs.harvard.edu/abs/2001ohnf.conf..315P

Quinn PR, Schwadron NA, Möbius E (2016) Transport of helium pickup ions within the focusing cone: reconciling STEREO observations with IBEX. Astrophys J 824(2):142. https://doi.org/10.3847/0004-637X/824/2/142

Rankin JS, McComas DJ, Richardson JD, Schwadron NA (2019b) Heliosheath properties measured from a Voyager 1 to Voyager 2 transient. Astrophys J 883:101. https://doi.org/10.3847/1538-4357/ab3d9d

Rankin JS, Stone EC, Cummings AC, McComas DJ, Lal N, Heikkila BC (2019a) Galactic cosmic-ray anisotropies: Voyager 1 in the local interstellar medium. Astrophys J 873:46. https://doi.org/10.3847/1538-4357/ab041f

Rankin JS, Bindi V, Bykov AM, Cummings AC, Della Torre S, Florinski V, Heber B, Potgieter MS, Stone EC, Zhang M (2022) Galactic cosmic rays throughout the heliosphere and in the very local interstellar medium. Space Sci Rev 218:42. https://doi.org/10.1007/s11214-022-00912-4

Rankin JS, McComas DJ, Alimaganbetov M, et al (2025) The Solar Wind and Pickup Ion Instrument (SWAPI) on NASA's Interstellar Mapping and Acceleration Probe. Space Sci Rev 221:108. https://doi.org/10.1007/s11214-025-01229-8

Raptis S, Lalti A, Lindberg M, et al (2024) Revealing an unexpectedly low electron injection threshold via reinforced shock acceleration. Nat Commun 16:488. https://doi.org/10.1038/s41467-024-55641-9

Reames DV (2014) Element abundances in solar energetic particles and the solar corona. Sol Phys 289:977–993. https://doi.org/10.1007/s11207-013-0350-4

Reeves GD, Spence HE, Henderson MG, et al (2013) Electron acceleration in the heart of the Van Allen radiation belts. Science 341(6149):991–994. https://doi.org/10.1126/science.1237744

Reid HAS, Kontar EP (2010) Solar wind density turbulence and solar flare electron transport from the Sun to the Earth. Astrophys J 721:864. https://doi.org/10.1088/0004-637x/721/1/864

Reisenfeld DB, Bzowski M, Funsten HO, et al (2016) Tracking the solar cycle through IBEX observations of energetic neutral atom flux variations at the heliospheric poles. Astrophys J 833:277. https://doi.org/10.3847/1538-4357/833/2/227

Reisenfeld DB, Bzowski M, Funsten HO, et al (2019) The influence of polar coronal holes on the polar ENA flux observed by IBEX. Astrophys J 879:1. https://doi.org/10.3847/1538-4357/ab22c0

Reisenfeld DB, Bzowski M, Funsten HO, et al (2021) A three-dimensional map of the heliosphere from IBEX. Astrophys J Suppl Ser 254:40. https://doi.org/10.3847/1538-4365/abf658

Reisenfeld DB, Allegrini FA, Christian ER, et al (2026) Exploring the Outer Heliosphere through ENA Observations from IMAP. Space Sci Rev 222. https://doi.org/10.1007/s11214-025-01258-3

Richardson JD (2010) Reflected ions at interplanetary shocks. Geophys Res Lett 37:L12105. https://doi.org/10.1029/2010GL043660

Richardson JD, Smith CW (2003) The radial temperature profile of the solar wind. Geophys Res Lett 30:1206. https://doi.org/10.1029/2002GL016551

Richardson JD, Paularena KI, Lazarus AJ, Belcher JW (1995) Evidence for a solar wind slowdown in the outer heliosphere? Geophys Res Lett 22:1469. https://doi.org/10.1029/95GL01421

Richardson JD, Kasper JC, Wang C, et al (2008) Cool heliosheath plasma and deceleration of the upstream solar wind at the termination shock. Nature 454:63–66

Richardson JD, Burlaga LF, Elliott HA, et al (2022) Observations of the outer heliosphere, heliosheath, and interstellar medium. Space Sci Rev 218(4):1–42. https://doi.org/10.1007/s11214-022-00899-y

Riley P, Linker JA, Mikic Z (2001) An empirically-driven global MHD model of the solar corona and inner heliosphere. J Geophys Res 106(8):15,889–15,901

Riley P, Caplan RM, Downs C, Linker JA, Lionello R (2022) Comparing and contrasting the properties of the inner heliosphere for the three most recent solar minima. J Geophys Res 127:e2022JA030261. https://doi.org/10.1029/2022JA030261

Roberts OW, Narita Y, Escoubet CP (2018) Multi-scale analysis of compressible fluctuations in the solar wind. Ann Geophys 36(1):47–52. https://doi.org/10.5194/angeo-36-47-2018

Rosenbauer H, Schwenn R, Marsch E, et al (1977) A survey on initial results of the helios plasma experiment. J Geophys 42:561–580

Rosenvinge TT, Richardson IG, Reames DV, et al (2009) The solar energetic particle event of 14 December 2006. Sol Phys 256:443–462. https://doi.org/10.1007/s11207-009-9353-6

Ruiz ME, Dasso S, Matthaeus WH, Weygand JM (2014) Characterization of the turbulent magnetic integral length in the solar wind: from 0.3 to 5 astronomical units. Sol Phys 289:3917. https://doi.org/10.1007/s11207-014-0531-9

Schwadron NA, Gloeckler G (2007) Pickup Ions and Anomalous Cosmic Rays from Dust in the Heliosphere. Space Sci Rev 96. https://doi.org/10.1007/s11214-007-9166-6

Schwadron NA, McComas DJ (2005) The sub-Parker spiral structure of the heliospheric magnetic field. Geophys Res Lett 32:L03112. https://doi.org/10.1029/2004GL021579

Schwadron NA, McComas DJ (2010) Pickup ions from energetic neutral atoms. Astrophys J Lett 712(2):2001–2003. https://doi.org/10.1088/2041-8205/712/2/L157

Schwadron NA, McComas DJ (2013) Spatial retention of ions producing the IBEX ribbon. Astrophys J 764:92. https://doi.org/10.1088/0004-637X/764/1/92

Schwadron NA, McComas DJ (2021) Switchbacks explained: super-Parker fields—the other side of the sub-Parker spiral. Astrophys J 909:95. https://doi.org/10.3847/1538-4357/abd4e6

Schwadron NA, Zurbuchen TH, Fisk LA, et al (1999) Pronounced enhancements of pickup hydrogen and helium in high-latitude compressional regions. J Geophys Res 104:535. https://doi.org/10.1029/1998JA900054

Schwadron NA, Geiss J, Fisk LA, et al (2000) Inner source distributions: theoretical interpretation, implications, and evidence for inner source protons. J Geophys Res 105:7465

Schwadron NA, Combi M, Huebner W, McComas DJ (2002) The outer source of pickup ions and anomalous cosmic rays. Geophys Res Lett 29:20. https://doi.org/10.1029/2002GL015829

Schwadron NA, Lee MA, McComas DJ (2008) Diffusive acceleration at the blunt termination shock. Astrophys J 675:1584. https://doi.org/10.1086/527026

Schwadron NA, Allegrini F, Bzowski M, et al (2018) Time dependence of the IBEX ribbon and the globally distributed energetic neutral atom flux using the first 9 years of observations. Astrophys J Suppl Ser 239:1. https://doi.org/10.3847/1538-4365/aae48e

Schwartz SJ, Burgess D, Wilkinson WP, et al (1992) Observations of short large-amplitude magnetic structures at a quasi-parallel shock. J Geophys Res 97:4209–4227. https://doi.org/10.1029/91JA02581

Schwartz SJ, Avanov L, Turner D, et al (2018) Ion kinetics in a hot flow anomaly: MMS observations. Geophys Res Lett 45:11520–11529. https://doi.org/10.1029/2018GL080189

Shi X, Artemyev A, Angelopoulos V, et al (2023) Evidence of electron acceleration via nonlinear resonant interactions with whistler-mode waves at foreshock transients. Astrophys J 952. https://doi.org/10.3847/1538-4357/acd9ab

Shrestha BL, McComas DJ, Zirnstein EJ, et al (2025) High-resolution observations of pickup-ion-mediated shocks to 60 au. Astrophys J 984:11. https://doi.org/10.3847/1538-4357/adc0a1

Singh RK, Mitra B, Durgaprasad N, et al (1991) Ionization states of the anomalous cosmic rays. Astrophys J 374:753. https://doi.org/10.1086/170160

Skoug RM, Gosling JT, McComas DJ, Smith CW, Hu Q (2006) Suprathermal electron 90 pitch angle depletions at reverse shocks in the solar wind. J Geophys Res 111:A01101. https://doi.org/10.1029/2005JA011316

Skoug RM, Schultz TB, Venhaus DM, et al (2026) The Solar Wind Electron (SWE) Instrument for the Interstellar Mapping and Acceleration Probe Mission. Space Sci Rev 222

Sokół JM, Swaczyna P, Bzowski M, Tokumaru M (2015) Reconstruction of helio-latitudinal structure of the solar wind proton speed and density. Sol Phys 290:2589–2615. https://doi.org/10.1007/s11207-015-0800-2

Sokół JM, Bzowski M, Kubiak MA, Möbius E (2016) Solar cycle variation of interstellar neutral He, Ne, O density and pick-up ions along the Earth's orbit. Mon Not R Astron Soc 458(4):3691–3704. https://doi.org/10.1093/mnras/stw515

Sokół JM, Bzowski M, Tokumaru M (2019) Interstellar neutral gas species and their pickup ions inside the heliospheric termination shock. Ionization rates for H, O, Ne, and He. Astrophys J 872:57. https://doi.org/10.3847/1538-4357/aafdaf

Sokół JM, McComas DJ, Bzowski M, Tokumaru M (2020) Sun-heliosphere observation based ionization rates model. Astrophys J 897:179. https://doi.org/10.3847/1538-4357/ab99a4

Sokół J, Kucharek H, Baliukin I, et al (2022) Interstellar neutrals, pickup ions, and energetic neutral atoms throughout the heliosphere: present theory and modeling overview. Space Sci Rev 218:18. https://doi.org/10.1007/s11214-022-00883-6

Sonnerup B (1969) Acceleration of particles reflected at a shock front. J Geophys Res 74:1301

Starkey MJ, Fuselier SA, Desai MI, et al (2019) Acceleration of interstellar pickup He+ at Earth's perpendicular bow shock. Geophys Res Lett 46(19):10735–10743. https://doi.org/10.1029/2019GL084198

Starkey MJ, Fuselier SA, Desai MI, et al (2021) MMS observations of energized He+ pickup ions at quasiperpendicular shocks. Astrophys J 913(2). https://doi.org/10.3847/1538-4357/abf4d9

Steinberg JT, Gosling JT, Skoug RM, Wiens RC (2005) Suprathermal electrons in high-speed streams from coronal holes: counterstreaming on open field lines at 1 AU. J Geophys Res 110:A06103. https://doi.org/10.1029/2005JA011027

Stern SA, Weaver HA, Spencer JR, et al (2019) Initial results from the new horizons exploration of 2014 MU69, a small Kuiper Belt object. Science 364(6441):eaaw9771. https://doi.org/10.1126/science.aaw9771

Strauss RD, Leske RA, Rankin JS (2023) The modulation of anomalous and galactic cosmic ray oxygen over successive solar cycle minima. Astrophys J 944:114. https://doi.org/10.3847/1538-4357/acb53d

Szabo A (2005) Multi-spacecraft observations of interplanetary shocks. In: The physics of collisionless shocks: 4th annual IGPP international astrophysics conference, vol 781, pp 37–41. https://doi.org/10.1063/1.2032672

Szabo A, Lepping RP, Merka J, Smith CW, Skoug RM (2001) The evolution of interplanetary shocks driven by magnetic clouds. In: Battrick B, Sawaya-Lacoste H (eds) Solar encounter: Proceedings of the First Solar Orbiter Workshop. ESA Special Publications, vol SP-493. ESA Publications Division, Noordwijk, pp 383–387

Szalay JR, Pokorný P, Malaspina DM, Pusack A, Bale SD, et al (2021) Collisional evolution of the inner zodiacal cloud. Planet Sci J 2:185. https://doi.org/10.3847/PSJ/abf928

Szalay JR, Provornikova E, Ayari E, et al (2026) Direct Samples of Interstellar and Interplanetary Material with IMAP. Space Sci Rev 222

Tan LC, Mason GM, Klecker B, Hovestadt D (1989) Seed population for about 1 MeV per nucleon heavy ions accelerated by interplanetary shocks. Astrophys J 345:572–583. https://doi.org/10.1086/167931

Taut A, Berger L, Möbius E, et al (2018) Challenges in the determination of the interstellar flow longitude from the pickup ion cutoff. Astron Astrophys 611:A61. https://doi.org/10.1051/0004-6361/201731796

Thorne RM, Li W, Ni B, et al (2013) Evolution and slow decay of an unusual narrow ring of relativistic electrons near L $\sim$ 3.2 following the September 2012 magnetic storm. Geophys Res Lett 40(14):3507–3511. https://doi.org/10.1002/grl.50627

Tokumaru M, Fujiki K, Kojima M, Iwai K (2021) Global distribution of the solar wind speed reconstructed from improved tomographic analysis of interplanetary scintillation observations between 1985 and 2019. Astrophys J 922:73. https://doi.org/10.3847/1538-4357/ac1862

Trotta D, Valentini F, Burgess D, Servidio S (2021) Phase space transport in the interaction between shocks and plasma turbulence. Proc Natl Acad Sci USA 118(21):e2026764118. https://doi.org/10.1073/pnas.2026764118

Tsurutani B, Baker D (1979) Substorm warnings: an ISEE-3 real time data system. Eos Trans AGU 60(41):701–703. https://doi.org/10.1029/EO060i041p00701

Tsurutani BT, Lin RP (1985) Acceleration of greater than 47 keV ions and greater than 2 keV electrons by interplanetary shocks at 1 AU. J Geophys Res 90:1–11. https://doi.org/10.1029/JA090iA01p00001

Tu CY, Marsch E (1994) On the nature of compressive fluctuations in the solar wind. J Geophys Res 99(A11):21481–21509. https://doi.org/10.1029/94JA00843

Turner DL, Wilson III LB, Liu TZ, et al (2018) Autogenous and efficient acceleration of energetic ions upstream of Earth's bow shock. Nature 561:206. https://doi.org/10.1038/s41586-018-0472-9

Turner DL, Liu TZ, Wilson III LB, et al (2020) Microscopic, multipoint characterization of foreshock bubbles with Magnetospheric Multiscale (MMS). J Geophys Res Space Phys 125:e2019JA027707. https://doi.org/10.1029/2019JA027707

Vasyliunas VM, Siscoe GL (1976) On the flux and the energy spectrum of interstellar ions in the Solar System. J Geophys Res 81(7):1247–1252. https://doi.org/10.1029/JA081i007p01247

Viall NM, DeForest CE, Kepko L (2021) Mesoscale structure in the solar wind. Front Astron Space Sci 8:735034. https://doi.org/10.3389/fspas.2021.735034

Wang C, Richardson JD (2005) Dynamic processes in the outer heliosphere: Voyager observations and models. Adv Space Res 35(1):2102–2105. https://doi.org/10.1016/j.asr.2004.10.008

Wang C, Richardson JD, Gosling JT (2000) Slowdown of the solar wind in the outer heliosphere and the interstellar neutral hydrogen density. Geophys Res Lett 27:2429. https://doi.org/10.1029/2000GL000058

Wang L, Lin RP, Krucker S, Mason GM (2012) A statistical study of solar electron events over one solar cycle. Astrophys J 759:69. https://doi.org/10.1088/0004-637X/759/1/69

Wang J, Matthaeus WH, Chhiber R, et al (2024) 1/f noise in the heliosphere: a target for PUNCH science. Sol Phys 299:169. https://doi.org/10.1007/s11207-024-02401-z

Wiedenbeck ME, Leske RA, Cohen CMS, et al (2008) In: Li G, et al (eds) Particle acceleration and transport in the heliosphere and beyond. AIP conf proc, vol 1039. AIP, Melville, p 149

Wijsen N, Aran A, Sanahuja B, et al (2020) The effect of drifts on the decay phase of SEP events. Astron Astrophys 634:A82. https://doi.org/10.1051/0004-6361/201937026

Wilson III LB, Sibeck DG, Turner DL, et al (2016) Relativistic electrons produced by foreshock disturbances observed upstream of Earth's bow shock. Phys Rev Lett 117. https://doi.org/10.1103/PhysRevLett.117.215101

Witte M, Banaszkiewicz M, Rosenbauer H (1996) Recent results on the parameters of the interstellar helium from the Ulysses/GAS experiment. Space Sci Rev 78(1–2):289–296. https://doi.org/10.1007/BF00170815

Xu S, Li H (2022) On the injection scale of the turbulence in the partially ionized very local interstellar medium. Astrophys J Lett 941:L19. https://doi.org/10.3847/2041-8213/aca143

Zank GP (2015) Faltering steps into the galaxy: the boundary regions of the heliosphere. Annu Rev Astron Astrophys 53:449–500. https://doi.org/10.1146/annurev-astro-082214-122254

Zank GP, Pauls HL, Cairns IH, Webb GM (1996) Interstellar pick-up ions and perpendicular shocks: implications for the termination shock and interplanetary shocks. J Geophys Res Space Phys 101:457–477

Zank GP, Rice WKM, Le Roux JA, Cairns IH, Webb GM (2001) The "injection problem" for quasiparallel shocks. Phys Plasmas 8(10):4560–4576. https://doi.org/10.1063/1.1400125

Zank GP, Li G, Florinski V, et al (2006) Particle acceleration at perpendicular shock waves: model and observations. J Geophys Res Space Phys 111:A06108. https://doi.org/10.1029/2005JA011524

Zank GP, Heerikhuisen J, Pogorelov V, et al (2010) Microstructure of the heliospheric termination shock: implications for energetic neutral atom observations. Astrophys J 708(2):1092. https://doi.org/10.1088/0004-637X/708/2/1092

Zank GP, Adhikari L, Zhao LL, et al (2018) The pickup ion-mediated solar wind. Astrophys J 869:23. https://doi.org/10.3847/1538-4357/aaebfe

Zank GP, Nakanotani M, Webb GB (2019) Compressible and incompressible magnetic turbulence observed in the very local interstellar medium by Voyager 1. Astrophys J 887:116. https://doi.org/10.3847/1538-4357/ab528c

Zank GP, Nakanotani M, Zhao L-L, Adhikari L, Che H, Le Roux JA (2021) Flux ropes, turbulence, and collisionless shock waves: high plasma beta case. Astrophys J 913:127. https://doi.org/10.3847/1538-4357/abf7c8

Zhang M, et al (2023) Numerical modeling of solar wind and coronal mass ejection in the inner heliosphere: a review. Front Astron Space Sci 10. https://doi.org/10.3389/fspas.2023.1105797

Zirnstein EJ, Heerikhuisen J, Zank GP, Pogorelov NV, McComas DJ (2014) Charge-exchange coupling between pickup ions across the heliopause and its effect on energetic neutral hydrogen flux. Astrophys J 783:129. https://doi.org/10.1088/0004-637X/783/2/129

Zirnstein EJ, Dayeh MA, McComas DJ, Sokół JM (2017) Imprint of the Sun's evolving polar winds on IBEX energetic neutral atom all-sky observations of the heliosphere. Astrophys J 846:63. https://doi.org/10.3847/1538-4357/aa7fba

Zirnstein EJ, Heerikhuisen J, Dayeh MA (2018a) The role of pickup ion dynamics outside of the heliopause in the limit of weak pitch angle scattering: implications for the source of the IBEX ribbon. Astrophys J 855:30. https://doi.org/10.3847/1538-4357/aaaf6d

Zirnstein EJ, Heerikhuisen J, McComas DJ, et al (2018b) Simulation of the solar wind dynamic pressure increase in 2014 and its effect on energetic neutral atom fluxes from the heliosphere. Astrophys J 859:104. https://doi.org/10.3847/1538-4357/aac016

Zirnstein EJ, Kumar R, Heerikhuisen J, et al (2018c) Constraining the evolution of the proton distribution function in the heliotail. Astrophys J 865:150. https://doi.org/10.3847/1538-4357/aadb98

Zirnstein EJ, Kumar R, Heerikhuisen J, et al (2018d) Stochastic acceleration of ∼0.1-5 keV pickup ions in the heliotail. Astrophys J 860:170. https://doi.org/10.3847/1538-4357/aac3de

Zirnstein EJ, McComas DJ, Kumar R, et al (2018e) In situ observations of preferential pickup ion heating at an interplanetary shock. Phys Rev Lett 121:075102. https://doi.org/10.1103/PhysRevLett.121.075102

Zirnstein EJ, McComas DJ, Schwadron NA, et al (2019) Strong scattering of ∼ keV pickup ions in the local interstellar magnetic field draped around our heliosphere: implications for the IBEX ribbon's source and IMAP. Astrophys J 876:92. https://doi.org/10.3847/1538-4357/ab15d6

Zirnstein EJ, Dayeh MA, McComas DJ, Sokół JM (2020a) Asymmetric structure of the solar wind and heliosphere from IBEX observations. Astrophys J 894:13. https://doi.org/10.3847/1538-4357/ab7b67

Zirnstein EJ, Giacalone J, Kumar R, et al (2020b) Turbulence in the local interstellar medium and the IBEX ribbon. Astrophys J 888:29. https://doi.org/10.3847/1538-4357/ab594d

Zirnstein EJ, Kumar R, Bandyopadhyay R, et al (2021) Turbulent acceleration of interstellar pickup ions at the heliospheric termination shock forms the global ENA spectrum. Astrophys J Lett 916:L21. https://doi.org/10.3847/2041-8213/ac12cc

Zirnstein EJ, Möbius E, Zhang M, et al (2022a) In situ observations of interstellar pickup ions from 1 au to the outer heliosphere. Space Sci Rev 218:28. https://doi.org/10.1007/s11214-022-00895-2

Zirnstein EJ, Shrestha BL, McComas DJ, et al (2022b) Oblique and rippled heliosphere structures from the interstellar boundary explorer. Nat Astron 6:1398–1413. https://doi.org/10.1038/s41550-022-01798-6

Zirnstein EJ, Swaczyna P, Dayeh MA, Heerikhuisen J (2023) Constraints on the IBEX ribbon's origin from its evolution over a solar cycle. Astrophys J 949:45. https://doi.org/10.3847/1538-4357/acc577

Zirnstein EJ, Kim TK, Rankin JS (2024) Evolving outer heliosphere: tracking solar wind transients from 1 au to the VLISM with IBEX and Voyager 1. Astrophys J 974:213. https://doi.org/10.3847/1538-4357/ad725a

Authors and Affiliations

C.M.S. Cohen[1] ⓘ **· B.L. Alterman[2] · D.N. Baker[3] · A. Bruno[2,4] · M. Bzowski[5] ·
E.R. Christian[2] · I.J. Cohen[6] · S. Dalla[7] · M.A. Dayeh[8] · M.I. Desai[8] · H.A. Elliott[8] ·
J. Giacalone[9] · M. Gkioulidou[6] · F. Guo[10] · T. Horbury[11] · S.G. Kanekal[2] ·
I. Kowalska-Leszczyńska[5] · C.O. Lee[12] · G.I. Livadiotis[13] · J.G. Luhmann[12] ·
W.H. Matthaeus[14] · D.J. McComas[13] · J.G. Mitchell[2] · E. Moebius[15] · J. Rankin[13] ·
J.D. Richardson[16] · N.A. Schwadron[15] · R. Skoug[10] · D. Turner[6] · G. Zank[17] ·
E.J. Zirnstein[13]**

✉ C.M.S. Cohen
    cohen@srl.caltech.edu

[1]   California Institute of Technology, Pasadena, CA, 91125, USA

[2]   Heliophysics Division, NASA, Goddard Space Flight Center, Greenbelt, MD, 20771, USA

[3]   Laboratory for Atmospheric and Space Physics, University of Colorado, Boulder, CO, 80309, USA

[4]   Catholic University of America, Washington, DC, 20064, USA

[5]   Space Research Centre, Polish Academy of Sciences (CBK PAN), 00-716, Warsaw, Poland

[6]   Johns Hopkins University Applied Physics Laboratory, Laurel, MD, 20723, USA

[7]   University of Lancashire, Preston, PR1 2HE, UK

[8]   Southwest Research Institute, San Antonio, TX, 78238, USA

[9]   Lunar and Planetary Laboratory, University of Arizona, Tucson, AZ, 85721, USA

[10] Los Alamos National Laboratory, Los Alamos, NM, 87544, USA

[11] Imperial College London, London, SW7 2AZ, UK

[12] Space Sciences Laboratory, University of California - Berkeley, Berkeley, CA, 94720, USA

[13] Department of Astrophysical Sciences, Princeton University, Princeton, NJ, 08544, USA

[14] Department of Physics and Astronomy, University of Delaware, Newark, DE, 19716, USA

[15] Space Science Center, University of New Hampshire, Durham, NH, 03824, USA

[16] Kavli Center for Astrophysics and Space Science, Massachusetts Institute of Technology, Cambridge, MA, 02139, USA

[17] Department of Space Science, University of Alabama in Huntsville, Huntsville, AL, 35899, USA